Title
NUCLEON ISOBAR PRODUCTION PROTON-PROTON COLLISIONS FROM 3 TO 7 GeV/c

Author
Ankeribrandt, Charles Martin.

Publication Date
1967-02-01

UCRL-17257

University of California

Ernest O. Lawrence Radiation Laboratory

NUCLEON-ISOBAR PRODUCTION IN PROTON-PROTON COLLISIONS FROM 3 to 7 GeV/c

DISCLAIMER

UCRL-17257

UNIVERSITY OF CALIFORNIA

Lawrence Radiation Laboratory
Berkeley, California

AEC Contract No. W-7405-eng-48

NUCLEON ISOBAR PRODUCTION IN PROTON—PROTON COLLISIONS FROM 3 to 7 GeV/c

Charles Martin Ankenbrandt
(Ph.D. Thesis)

NUCLEON ISOBAR PRODUCTION IN PROTON—PROTON COLLISIONS FROM 3 TO 7 GeV/c

Contents

II. Experimental Method and Apparatus

III. Reduction and Correction of the Data

IV. Results

Appendices

NUCLEON ISOBAR PRODUCTION IN PROTON—PROTON COLLISIONS FROM 3 TO 7 GeV/c

Charles Martin Ankenbrandt

Lawrence Radiation Laboratory
University of California
Berkeley, California

ABSTRACT

A systematic study of the reactions pp → pp and pp → pN* in the angular range from $\theta_{lab} = 10^\circ$ to $\theta_{cm} = 90^\circ$ at 3, 4, 5, 6, and 7 GeV/c is reported. A "missing mass" spectrometer detected protons resulting from interactions of the Bevatron external proton beam in a liquid hydrogen target. The spectrometer consisted of a series of bending and focusing magnets and a scintillator hodoscope.

Peaks in the missing mass spectra occur at average N* masses of 1240 ± 6 MeV, 1508 ± 2 MeV, and 1683 ± 3 MeV with average full widths of 102 ± 4 MeV, 92 ± 3 MeV, and 110 ± 4 MeV respectively. In the missing mass region below 2400 MeV no other significant enhancements are found.

Comparison of the N* production cross sections $d\sigma/dt$ near $\theta_{cm} = 90^\circ$ with the predictions of the statistical model indicates partial success of the model. The differential cross sections at fixed energy manifest exponential dependence on $v = [-tu/(t + u)]$, a symmetric function of the Mandlestam variables t and u, which reduces to the squared transverse momentum transfer for elastic scattering. The slopes of these exponentials vary systematically with energy in a way that depends on the particular reaction under consideration; but all these slopes tend toward the same value ($v_o \approx 0.4\ \text{GeV}^2$) at the upper limit of our energy range.

I. INTRODUCTION

Pion-nucleon cross sections manifest considerable structure as functions of energy. Figure 1 (adapted from Chew *et al.*(1)) illustrates the dependence of the $\pi^{\pm}p$ total cross sections on center-of-mass energy. The peaks near 1238, 1512, and 1688 MeV constituted early evidence for the existence of pion-nucleon resonant states. Such resonances, since they are formed by strong interactions between pions (baryon number B = 0, strangeness S = 0, isospin I = 1) and nucleons (B = 1, S = 0, I = 1/2), must be nonstrange baryons of isospin 1/2 or 3/2. They are sometimes called nucleon isobars and denoted by the symbol N*.

The $\pi^{\pm}p$ total cross sections reveal some of the properties of these resonant states. A resonance of isospin I produces a peak in the corresponding cross section σ_I for that isospin state. These isospin cross sections can be calculated from the measured total cross sections via Clebsch-Gordan coefficients, resulting in the relations

$$\sigma_{3/2} = \sigma_{\pi^+p} \qquad (1)$$

and

$$\sigma_{1/2} = 3/2\sigma_{\pi^-p} - 1/2\sigma_{\pi^+p}. \qquad (2)$$

The location and full width of a peak in σ_I yield the mass and width of a well-resolved isobar. The nucleon isobar spectrum implied by this simple interpretation of the structure is presented in Table 1 a, which is adapted from the 1963 compilation of Barkas *et al.*(2).

The discovery of these peaks motivated an extensive experimental effort by many groups to acquire more detailed data on the pion-nucleon interaction. Differential elastic cross sections, charge exchange and polarization data as well as inelastic cross sections and photoproduction cross sections have been measured in the neighborhood of the peaks. Subsequent phase-shift analyses(3-7) of this wealth of data indicate that the peaks near 1512 and 1688 MeV are probably superpositions of several resonances. The current isobar spectrum incorporating these developments is presented in Table 1b, adapted from the most recent compilation of Rosenfeld *et al.*(8)

As this work on the pion-nucleon system proceeded, a related phenomenon was discovered in proton-proton interactions. Peaks were observed in the missing mass spectra of particles produced along with protons in inelastic proton-proton collision.(9-12) Interpretation of these peaks as evidence for the reaction

$$p + p \rightarrow p + N^* \qquad (3)$$

was confirmed by the agreement of the calculated N* masses with the masses at the pion-nucleon peaks. Application to reaction (3) of the discrete conservation laws yield N* quantum numbers which are identical to those of the πN system.

Two types of information are available from studies of reaction (3). First, one can examine the intrinsic properties of the isobar spectrum; in particular, one can measure mass and width parameters of known resonances and search for evidence of new ones. Second, one can study the production properties of the various isobars; in this manner various models of the reaction can be tested and further understanding of the fundamental proton-proton interaction can be acquired.

Investigations of this reaction by several groups using counter and spark chamber techniques have provided extensive data on nucleon isobar production at low momentum transfers. The main features of the data are the following:

(1) A new enhancement near 1410 MeV has been observed.(12-16)

(2) The higher-mass resonances above 1688 MeV are not copiously produced at presently available energies.(10, 11, 13, 15, 16)

(3) The total production cross sections at high energy are roughly constant for the $T = 1/2$ isobars but fall with increasing energy for the $T = 3/2$ N*(1238).(15) The N*(1238) and N*(1512) cross sections manifest peaks above their production thresholds.(16)

(4) The slopes of the differential production cross sections $\frac{d\sigma}{dt}$ vs. t at low momentum transfer are comparable to that of the elastic.(12, 15, 16)

In contrast to this fairly complete experimental picture of N* production in low-momentum-transfer proton-proton collisions, the information at medium and high momentum transfers is very scanty; only a few isolated data points exist.(11, 14, 15) The goal of the experiment reported herein was a systematic survey of N* production in this latter range of momentum transfers. Such information helps to discriminate among the various possible interpretations of the proton-proton elastic scattering data in this momentum-transfer region. In particular the relative N* production cross sections provide a direct test of the basic statistical model assumption that various final states are produced according to their intrinsic statistical weights; and the dependence of the data on transverse momentum transfer serves to define the region of validity of empirical formulae such as that of Orear.(17, 18)

II. EXPERIMENTAL METHOD AND APPARATUS

A. Introduction

Resonances, i.e., unstable particles which decay via strong interactions, have lifetimes so short that their trajectories cannot be measured directly. The evidence for their formation or production in a given type of reaction must then necessarily be indirect. One of the simplest ways to deduce their presence is by observing the peaks they produce in invariant mass spectra. The peaks in pion-nucleon total cross sections furnish a familiar example; here the total center-of-mass energy is the invariant mass of the pion-nucleon system, and its value at a peak gives the mass of the corresponding resonance. Alternatively, mass spectra can be obtained indirectly by application of the conservation laws of energy and momentum. For a reaction of the form

$$m_1 + m_2 \rightarrow m_3 + m_4 \tag{4}$$

involving particles or particle systems of invariant mass m_i, total energy E_i, and momentum $\vec{p}_i$, the conservation laws take the form

$$E_1 + E_2 = E_3 + E_4 \tag{5}$$

and

$$\vec{p}_1 + \vec{p}_2 = \vec{p}_3 + \vec{p}_4 . \tag{6}$$

Then m_4 is given by

$$m_4^2 = E_4^2 - \vec{p}_4^{\,2} = (E_1 + E_2 - E_3)^2 - (\vec{p}_1 + \vec{p}_2 - \vec{p}_3)^2. \tag{7}$$

In the lab system where particle 2, the target, is at rest, this reduces to

$$m_4^2 = m_1^2 - m_2^2 + m_3^2 + 2\,[p_1 p_3 \cos\theta_3 - (E_1 + m_2)(E_3 - m_2)], \tag{8}$$

where θ_3 is the lab angle between $\vec{p}_1$ and $\vec{p}_3$. Thus for a kinematically well-defined initial state, measurement of the momentum and angle of particle 3, together with a knowledge of its mass m_3, suffices to determine m_4, the "missing mass". The discrete conservation laws allow one to deduce additional properties of particle m_4, for example its baryon number, strangeness, charge, and sometimes its isospin. The present experiment was based on this idea; such experiments are sometimes called missing mass experiments.

The apparatus to be described in this section was used to study several quasi-two-body reactions of type (4). Besides the nucleon isobar production reaction $p + p \to p + N^*$, which is the subject of this thesis, the following reactions were observed:

$$p + p \to \pi^+ + d \tag{9}$$

$$p + p \to \pi^\pm + X \tag{10}$$

$$p + p \to K^+ + (\Lambda p) \tag{11}$$

$$p + p \to p + p \tag{12}$$

$$p + p \to d + X \tag{13}$$

$$p + d \to p + d \tag{14}$$

$$p + N\,(N) \to p + N\,(N). \tag{15}$$

Here X represents a system of particles and (N) is a spectator nucleon in the deuteron. A description of the apparatus has been published(19); the present account is included here for completeness.

Figure 2 is a schematic diagram of the complete experimental arrangement. The setup can be called a missing mass spectrometer since it provided for the determination of the kinematic quantities which are required in order to calculate m_4 via formula (8). A general understanding of the system can be gained by considering how these quantities were measured.

The incident beam was the external proton beam (EPB) of the Bevatron. Its energy was maintained at a preselected value by monitoring the Bevatron magnetic field. A target filled with liquid hydrogen or liquid deuterium was used.

The scattered beam was bent by bending magnets B_i and focused by quadrupoles Q_i to a detection system consisting of scintillators and gas Cerenkov counters. The vertical bending magnets B_{4-6} provided momentum analysis in a vertical plane, allowing p_3 to be determined. For a given momentum p_3, the scattering angle θ_3 was determined by the horizontal coordinate of the particle at the image plane. The Cerenkov counters were used when necessary to select the particle m_3 of interest.

The primary design goals of the spectrometer were threefold: good statistics, good missing mass resolution, and reduction of certain systematic errors to which the missing mass method is susceptible. The remainder of this section is devoted to a more detailed discussion of the spectrometer design and the experimental methods.

B. Incident Beam and Target

The target for this experiment was located at the second focus of the EPB. The optics and geometry of the EPB have been described elsewhere(20). Vertically the beam was focused to a point at the target and horizontally it was parallel. As will be seen later, errors in the horizontal direction of the incident beam directly affect the measurement of the scattering angle θ_3. The horizontal angular spread of the beam at the target was estimated to be ± 0.5 mr. The direction of the beam was continuously monitored downstream of the target by left-right scintillators whose output was displayed on an oscilloscope in the electronics area.

The vertical location and spot size of the beam affect the accuracy and precision of measurement of the scattered momentum p_3. The location of the beam was checked periodically between runs by remotely viewing a scintillator which could be positioned behind our target. The maximum vertical spot size at the target was about 0.2 in.; this was demagnified by about a factor of two in the spectrometer image plane.

The average beam intensity was of the order of 10^{11} protons per pulse, with a repetition rate of about 11 pulses per minute. The spill length averaged about 500 ms during Bevatron "flattop" with little radio frequency structure. The intensity was monitored by an ionization chamber located 6.5 ft. downstream of the target. In our early running at 7 GeV/c, the ion chamber was further downstream; the greater beam width at this point affected the reproducibility of the ion chamber readings. An estimated error of ± 10% is applied to these data. For most of the running, a chamber which had been directly calibrated during a previous experiment(21) was used. Another ion chamber which was used briefly during the experiment was calibrated against a group of ionization chambers and secondary emission monitors located along the external beam. The charge collected by the ion chamber is proportional to the integrated beam flux. The capacitor voltage induced by this charge was converted by an analog-to-digital converter (ADC) and automatically recorded after each pulse.

It was important to know the beam momentum and keep it constant for a set of runs. This was accomplished by gating our scalers on when the Bevatron magnetic field fell within two preselected values. The field was measured by integrating the current induced in a current loop around the Bevatron by the changing magnetic field. This gate is thus called the "$\int \dot{B}dt$ gate"; the range of values accepted was usually ± 0.2%, which matched our resolution in scattered momentum.

A portion of the data was taken with another experimenter's target at the first focus of the EPB; for the N^* running, the main effect of this target was a slight deterioration of our missing mass resolution.

Our target was a liquid hydrogen/deuterium target of conventional cryogenic design. The flask was a cylinder 4 inches in diameter and 12 inches in length along the beam direction. The sides of the flask were of mylar with stainless steel end domes of 3.5 inch radius. The beam spot was about 2 inches wide horizontally at the target and about 0.2 inches high.

The material in the incident and scattered beam at the target was the minimum consistent with cryogenic and safety requirements. Thin mylar and aluminum windows in the vacuum jacket surrounding the flask allowed for the entry and exit of particles. The "target empty" background (with H_2 gas near atmospheric pressure in the flask) was about 5% of the target full rate. The scattered particles traversed a total of 0.2 $\mathrm{gm/cm^2}$ of aluminum and mylar in leaving the target.

C. Spectrometer

Figure 2 shows the layout of the scattered beam. See also Table 2 for detailed characteristics of the spectrometer magnets.

B_1 and B_2 are uniform-field "C" magnets which were movable to change the production angle θ_3 between the limits of 10° and 70°. The magnet positions for these extreme angles are indicated in the figure. The movement of B_1 and B_2 was accomplished in a novel manner. Each magnet rested on four air pads. The magnets could be raised slightly above a steel plate by air pressure applied to the pads (30 psi at a total flow of 100 $\mathrm{ft^3/min}$ NTP). A small remotely-controlled motor then moved the magnets horizontally. Guide rails assured the proper relative alignment of the magnets; the position along the rails was remotely digitized. Bellows-type plastic bags moving with the magnets were filled with helium to reduce the scattering along the beam path. When necessary, a concrete block was moved into position behind B_2 to shield the fixed channel from particles coming directly from the target.

The remainder of the magnets defined a fixed channel at an angle of 14° to the incident beam. The function of B_3, a uniform-field "H" magnet, was to direct the scattered particles down the fixed channel. A vacuum pipe occupied the fixed portion of the beam path, from B_3 to B_6.

Q_1 and Q_2 constitute a quadrupole doublet with a circular aperture Of 7.75 inch diameter; Q_1 focused the beam horizontally and Q_2 focused vertically. The quadrupole field gradients were chosen so that in the horizontal plane particles produced at a given angle θ_3, from any point on the target, were focused to a point in the image plane ("parallel-to-point" focusing); in the vertical plane an image of the beam spot at the target was formed in the image plane ("point-to-point" focusing).

Magnets B_4, B_5, B_6 are identical "H" magnets which produced a total vertical deflection of 15° for a central-momentum particle. Particles of different momenta were deflected through different angles and thus separated vertically in the image plane. All the bending magnets were shimmed to provide magnetic field path integrals uniform to 0.1% over the apertures.

The heart of the particle detection system was a 28-element scintillator hodoscope mounted perpendicular to the scattered beam at the image plane. Each element had a sensitive area 6.75 in. by 0.25 in. and a thickness of 0.5 in. in the beam direction. Figure 3 shows details of the hodoscope construction.

D. Kinematic Relations at the Hodoscope

The optical properties of the spectrometer are illustrated by the ray diagrams of Figure 4. In discussing these properties, we will momentarily neglect chromatic aberrations for simplicity. In this approximation, the optical properties are such that the momentum and angle of a scattered particle are uniquely determined by the coordinates of its intersection with the hodoscope.

Let us define a Cartesian coordinate system in the plane of the hodoscope as shown in Figure 5. (The reason for the rotation of the hodoscope in the figure will be explained shortly.) The horizontal x-axis points in the direction of increasing θ_3; the y-axis is normal to the scattered beam direction and is thus directed upward at a 15° angle with the vertical.

In a vertical plane, an image of the target is produced at the hodoscope. The vertical coordinate thus depends only on the momentum of the particle, through the relation $p = eB\rho$. For small deviations of the momentum p_3 from its value p_c at the center of the hodoscope, we may write

$$y = D \frac{\Delta p}{p_c} \tag{16}$$

where D (= 59.2 in.) is defined as the dispersion at the hodoscope and $\Delta p = p_3 - p_c$.

In the horizontal direction, let θ_h represent the angle between the incident beam direction and the trajectory of a particle as it enters the quadrupole. Since the hodoscope lies at the focus of the optical system and the incident beam is parallel, the horizontal displacement at the hodoscope is given by

$$x = f_h \, \Delta\theta_h, \tag{17}$$

where f_h is the horizontal focal length and $\Delta\theta_h$ is the deviation of the trajectory from the central ray of angle θ_{hc},

$$\Delta\theta_h = \theta_h - \theta_{hc}. \tag{18}$$

The focal length f_h is 612 in. when $\theta_3 = \theta_{hc} = 14^\circ$ and depends slightly on θ_3.

The uniform-field magnets B_1, B_2, B_3 provide no horizontal focusing but merely bend the beam through angles of Φ_1, Φ_1, and Φ_2 respectively. Thus the angle θ_h is related to the production angle θ_3 by the equation

$$\theta_h = \theta_3 + 2\Phi_1(p_3) + \Phi_2(p_3). \tag{19}$$

Combining equations (17), (18), and (19) leads to the result that

$$x = f_h \, [\theta_3 + 2\Phi_1(p_3) + \Phi_2(p_3) - \theta_{hc}]. \tag{20}$$

Alternatively, equations (17) and (19) lead to the relation

$$x = f_h \, [\Delta\theta_3 + 2\Delta\Phi_1(p_3) + \Delta\Phi_2(p_3)], \tag{21}$$

where $\Delta\theta_3$ measures the variation of θ_3 from its central value θ_{3c}. Equations (16) and (20) are the desired results relating θ_3 and p_3 to the x - y coordinates on the hodoscope.

The variation of missing mass over the hodoscope is then calculable. For fixed incident momentum one has

$$M_4^{\,2} \, (p_1, p_3, \theta_3) = M_4^{\,2} \, (p_3, \theta_3) = M_4^{\,2} \, (x, y). \tag{22}$$

The variations in p_3 and θ_3 over the hodoscope are small so that to good approximation

$$M_4^2\,(p_3, \theta_3) = M_4^2\,(p_{3c}, \theta_{3c}) + \left(\frac{\partial M_4^2}{\partial p_3}\right)\Delta p_3 + \left(\frac{\partial M_4^2}{\partial \theta_3}\right)\Delta \theta_3 \qquad (23)$$

$$= M_4^2\,(p_{3c}, \theta_{3c}) + x\left(\frac{\partial M_4^2}{\partial x}\right) + y\left(\frac{\partial M_4^2}{\partial y}\right). \qquad (24)$$

The missing mass is therefore constant along a line $y = mx + b$, where b is arbitrary and

$$m = -\left(\frac{\partial M_4^2}{\partial x}\right) \Big/ \left(\frac{\partial M_4^2}{\partial y}\right) = \left(\frac{\partial y}{\partial x}\right)_{M_4}. \qquad (25)$$

In this experiment the hodoscope was rotated by remote control through an angle δ to align the elements with these lines of constant missing mass (see Figure 5). In our (lefthanded) coordinate system, the angle δ is determined by

$$\cot \delta = -\frac{1}{m} = -\left(\frac{\partial x}{\partial y}\right)_{M_4}. \qquad (26)$$

To evaluate δ in terms of production kinematics and spectrometer parameters, consider the displacements at the hodoscope produced by small variations, at fixed M_4, of θ_3 and p_3 from their central values. Equations (16) and (21) yield

$$\left(\frac{\partial x}{\partial y}\right)_{M_4} = \frac{f_h\,(\Delta\theta_3 + 2\Delta\Phi_1 + \Delta\Phi_2)}{D\,(\Delta p/p)}. \qquad (27)$$

Using the small-angle relation

$$\frac{\Delta\Phi}{\Phi} = -\frac{\Delta p}{p} \qquad (28)$$

for the bending angles and the kinematic relation between θ_3 and p_3 at fixed M_4

$$\Delta\theta_3 = \left(\frac{\partial \theta_3}{\partial p_3}\right)_{M_4} \Delta p_3, \qquad (29)$$

we find that

$$\cot\delta = \frac{f_h}{D}\left[2\Phi_1 + \Phi_2 - p_3\left(\frac{\partial\theta_3}{\partial p_3}\right)_{M_4}\right]. \tag{30}$$

When the hodoscope is oriented at the proper angle δ, each element subtends an interval in θ_3 of the order of 10 mr (dependent on the spectrometer settings) without a corresponding deterioration of missing mass resolution.

The range of masses $\Delta(M_4^2)$ which a single hodoscope element accepts is determined by the rate of change of missing mass in the normal direction $\vec{n}$. Explicitly we have

$$\Delta(M_4^2) = w\,\frac{dM_4^2}{dn} = 2p_1p_3(w/f_h)\,\sin\theta_3\,\csc\delta \tag{31}$$

for a detector of width w(.25 in.). Some typical values of $\Delta M_4 = \Delta(M_4^2)/2M_4$ are shown in Figure 6.

E. Measurement Accuracy and Precision

Equation (8) indicates that systematic errors in p_1, p_3, and θ_3 can be serious in an experiment of this type because M_4 depends sensitively on these quantities. For example, $(\partial M_4/\partial\theta_3)$ is -8.14 MeV/mr for the elastic peak at 7 GeV/c and 10°. Systematic errors in p_1, p_3, and θ_3 can be located and corrected by using the elastic and $pp \rightarrow \pi^+ d$ peaks as calibration points for the mass scale. In calculating this correction it is desirable to separate the random errors from the systematic ones. Details of the method are described in Appendix A.

The main sources of resolution loss in this apparatus are the following: (a) spread in momentum, horizontal direction, and vertical position of the incident beam, (b) multiple Coulomb scattering of the scattered beam, and (c) chromatic aberrations in the spectrometer optics. The chromatic aberrations are large at the top and bottom of the hodoscope because of the large momentum acceptance ($\frac{\Delta p}{p} \approx \pm 6\%$) of the spectrometer. The image moves downstream about 43 in. for a $\frac{\Delta p}{p}$ of + 6%, which implies a spot size of about 0.87 in. diameter at the edges of the hodoscope. The resolution at the center of the hodoscope, where chromatic effects are absent, can be calculated from an incoherent sum of the estimated effects of (a) and (b) above. That the resolution is approximately as expected can be verified by comparison of the observed and calculated widths of the proton-proton elastic scattering peak. Usually the peak is largely confined to a single hodoscope element as expected. The comparison is carried out in Section III B.

A principal advantage of the hodoscope lies in its ability to accumulate data simultaneously over an entire peak. This greatly facilitates the identification of small peaks on a large background. Previous experience(14) showed that the alternative method of using a single counter to take consecutive points in the neighborhood of a peak is plagued by difficulties involving temporal fluctuations in incident beam position and direction, spectrometer magnet currents, background levels, etc. In this experiment such errors lead principally to occasional mismatches between the data from adjacent runs.

F. Detectors and Fast Electronics

The detection system for this experiment consisted in general of a scintillator and Cerenkov counter telescope which identified particles of the desired type in the scattered beam. Coincidences between the telescope output and the hodoscope elements were recorded on 10 Mc/sec scalers. The good temporal resolution of the scintillation and Cerenkov counters and their remoteness from the target enabled us to use the high intensity of the EPB to advantage in obtaining good statistics in reasonable running times. For detecting protons the Cerenkov counters were not used because rejection of π^+ and K^+ was deemed unnecessary; justification for this approximation is given in Section III A. When not in use, Cerenkov counters C_1 and C_2 were lowered out of the scattered beam.

To detect protons, we used two scintillators S_2 and S_3 in coincidence with the hodoscope. In addition, an anticoincidence counter $\overline{A}$ was used to reduce background in the hodoscope light pipes. The orientation of these scintillators is shown in Figure 7. S_3 defined a 6.75 in. effective length for each hodoscope element; S_2 was slightly larger. The counter dimensions are given in Table 3.

S_2, S_3, and $\overline{A}$ were viewed by RCA 6810A photomultipliers (two for $\overline{A}$). For the hodoscope detectors, we used the smaller 1P21 photomultiplier tubes because of space limitations.

The fast electronics was assembled from Chronetics modular discriminators, coincidence circuits and fanouts in conjunction with standard LRL 10 Mc/sec scalers. A block diagram of the fast electronics is shown in Figure 8. Not shown is an adder circuit by which the hodoscope outputs were summed electronically and recorded on a scaler called the E' scaler. The E and E' scalers thus recorded the channel trigger rate and the electronically added hodoscope counting rate respectively. The E' circuit had the desirable property of recording only one count when two or more hodoscope elements fired within the resolving time (~20 ns) of the E' circuitry. It thereby generates a correction to the hodoscope output data; see Section III A for a description of this correction.

The E and E' scalers were 6-decade scalers, whereas the hodoscope scalers were 3-decade scalers. The limit of 10^3 per pulse on the hodoscope counters occasionally led to overflow problems, particularly at the elastic peak where the incident beam intensity often had to be decreased. In case of an overflow, the most significant digit was lost but the first three digits were correct. Since the data for each pulse were recorded separately, occasional overflows could be identified and either corrected or eliminated by comparing the sum of the hodoscope counts with the E and E' counts or by checking the smoothness of the data.

G. Data Acquisition and Storage

A block diagram of the information-handling system is shown in Figure 9. The heart of the system was an on-line PDP-5 computer. This small computer, manufactured by the Digital Equipment Corporation, is characterized by a 12-bit, 4096-word core memory with a 6-μsec cycle time. The rapid rate of data accumulation necessitated the use of a computer both to store the data and to monitor the progress of the experiment and the performance of the equipment.

The experiment was divided into runs with constant settings of all the variable parameters of the apparatus. The N* runs were typically of a few minutes' duration. At the start of each run, the movable magnet position and $B_4B_5B_6$ magnet current were read into the computer via an analogue-to-digital converter. These determined the angle θ_3 and momentum p_3 which were also recorded in the log book. After each Bevatron pulse, 30 scalers (H_{1-28}, E, and E') were read and reset by the computer, as was the ion chamber output integrator (incident beam intensity). The information from each pulse was written on magnetic tape, then added to the previous data in the computer.

Operator intervention and control was accomplished by Teletype communication and by a set of 24 switches ("switch register") through which various options (e.g. start run, end run) could be exercised.

A display oscilloscope provided the main on-line feedback of data to the experimenters. Histograms of the hodoscope data, either cumulative or pulse-by-pulse, could be displayed. In this way an almost continuous record of the progress of a run was available. At the end of a run, a Polaroid photograph of a parallel oscilloscope was taken for the log book, and the accumulated data were typed out on the Teletype and written on the magnetic tape.

III. REDUCTION AND CORRECTION OF THE DATA

A. Anaylsis of Individual Runs

1. Differential Cross Section Formula

The basic results of this experiment are missing mass spectra for various fixed incident momenta and lab angles. These spectra take the form of doubly-differential cross sections $(d^2\sigma/dM_4{}^2dt)$ as functions of p_1, θ_3, and M_4. The cross sections are given in terms of experimentally determined quantities by the formula

$$\frac{d^2\sigma}{dM_4{}^2dt}\,(p_1,\,\theta_3,\,M_4) = \frac{N_s}{N_\ell n_t} \cdot \frac{1}{\Delta\Omega_L \Delta M_4{}^2}\;J\left(\frac{M_4{}^2,\;\Omega_L}{M_4{}^2,\;t}\right), \qquad (32)$$

where N_s = No. of protons scattered into lab solid angle $\Delta\Omega_L$ with squared missing mass in the range $\Delta M_4{}^2$,

N_ℓ = No. of incident protons,

n_t = Target thickness in protons per unit area,

$J\left(\frac{M_4{}^2,\;\Omega_L}{M_4{}^2,\;t}\right)$ = Jacobian transformation from lab solid angle Ω_L to invariant 4-momentum transfer squared, t. This Jacobian is evaluated in Appendix B.

This section describes the analysis and corrections necessary to deduce these cross sections from the raw data via equation (32).

2. Combination of Data into Runs

The first step is to combine the counting data from a set of Bevatron pulses into composite results for a run. These data consist of 30 scaler readings (H_{1-28}, E, E'), and the voltage V of the ion chamber output intergrator ($0 \leq V \leq 10$ volts). In combining the data, scaler overflows are discovered and, if possible, corrected; also self-consistency of the pulse data is checked. A pulse is eliminated if it contains an unrecoverable scaler overflow, if it is obviously inconsistent with the other pulses, or if V is outside the range $0.5 \text{ v.} \leq V \leq 9.5 \text{ v.}$ Each of these requirements eliminates about 5% of the pulses. The combined data yield N_s and N_ℓ in equation (32) for a set of 28 adjacent mass intervals. N_ℓ is determined by the relation

$$N_\ell = SCV, \tag{33}$$

in which S is the sensitivity of the ion chamber in protons per microcoulomb and C is the charge-collecting capacitance.

3. Kinematics

The next step is to calculate, for each hodoscope element, the kinematic quantities which enter equation (32) as independent variables and as factors in the cross section. As was indicated in Section II D, the kinematic quantities are determined everywhere on the hodoscope by their values at the center of the hodoscope and by the optical properties of the spectrometer. The actual reconstruction and correction of the kinematics on the hodoscope proceeds as follows.

In preparation for the experiment, an IBM 7094 computer program calculated kinematic quantities and the corresponding spectometer settings (magnet currents, angle δ, and movable magnet position) for sets of runs at constant p_1 and θ_3; the runs comprising a set cover overlapping intervals in M_4 so as to define a complete missing mass spectrum. Included in each set are runs centered at 938, 1238, 1512, and 1688 MeV, the locations of elastic and isobar peaks. The nominal values of p_1, θ_3, and M_4 associated with each run were entered in the log book.

During the course of the experiment, systematic errors in the positions of elastic peaks were observed. Subsequent measurements of the spectrometer geometry and the total magnetic field path integral through $B_4B_5B_6$ indicated slight ($< 1\%$) deviations from nominal values. In addition there were systematic effects of the following types: errors of the order of 1% in calculating p_1 from the integrated Bevatron field, errors of the same order in determining p_3 at the center of the hodoscope, and uncertainties of the order of a few mr in determining θ_3 from the channel angle θ_h and the horizontal bending angles. Corrections for these effects are made in two steps as follows. First the known corrections to the spectrometer geometry and magnet excitation curves are used in conjunction with the actual magnet currents (as determined from the nominal kinematics) to calculate corrected kinematics. Then further corrections to p_1, p_3, and θ_3 are determined empirically via a least squares fitting procedure which uses as input the observed positions of the elastic peak and the pion peak from $pp \to \pi^+ d$. Details of the fitting procedure are described in Appendix A. Histograms of observed peak masses before and after the latter correction are shown in Figure 10. The spread in mass remaining after the fitting correction is attributed to random errors.

The kinematic variables at any point on the hodoscope are then determined from the corrected central p_3, θ_3, and M_4 by the methods of Section II D.

4. Laboratory Solid Angle

A numerical calculation of the laboratory solid angle subtended by each hodoscope element for each run was performed on the CDC 6600 computer. The method is based on ray-tracing of extreme rays, with matrix representation of the spectrometer elements. Details of this calculation are given in Appendix C.

The solid angle is typically about 10^{-4} steradians. The "illumination" on the hodoscope is almost uniform vertically but decreases by about a factor of two from center to edge horizontally. Thus the solid angle is about the same for each hodoscope element unless the angle δ is large. The dependence of $\Delta\Omega$ on laboratory angle θ_3 is illustrated in Figure 11, in which the quantity $\Delta\Omega\Delta p/p$ is plotted for a central hodoscope element. The minimum near 14° is caused by the lack of vertical focusing in magnets B_1 and B_2 at that angle.

5. Counting Corrections

The following three effects must be examined as possible sources of background in our proton spectra:

(a) counts in two or more hodoscope elements caused by a single scattered particle ("double counts"),

(b) interactions on material other than hydrogen at the target,

and (c) detection of particles other than protons.

In this section these effects are considered in turn.

The presence of a significant number of double counts in our apparatus is indicated empirically by the fact that the sum of the hodoscope counts consistently exceeds the number in E' by about 8%. As pointed out previously (Section II F), this excess is a measure of the number of times when two or more hodoscope counts occurred within the resolving time of the E' circuitry. E' is used for this test rather than E (the total channel flux) because the channel counters are vertically slightly larger than the hodoscope. Indeed, E usually exceeds E' by 1% to 4% for this reason.

Accidental coincidences between two beam particles do not account for a significant part of this excess; this is indicated by direct estimates of the accidental rate and verified by the fact that the excess is approximately independent of the scattered beam flux.

In fact, estimates indicate that the following effects account for most of the excess: passage of a single particle through two hodoscope elements (~ 0.5%), interactions of scattered-beam particles in S_2 and in the hodoscope (~ 2%), and production of delta rays in S_2 and in the hodoscope (~ 4%). Since these effects usually produce spurious counts close to the original particle path, thereby preserving the shape of the spectrum, the correction is made by dividing the data by the observed ratio of ΣH_i to E' for each run.

Regarding the background from the target walls, the counting rate with target empty was found to be about 5% of the target full rate for a representative small sample of runs. Since this background is caused by scattering from composite nuclei, it does not show the structure inherent in the proton-proton spectra. Care must thus be taken that the method of subtraction of this background does not affect the size of the peaks. The correction is accomplished by fitting the spectra with a polynomial plus peaks and subtracting 5% of the polynomial from the data.

With respect to the background from particles other than protons, it has already been mentioned that no attempt was made to reject such particles electronically. This background has been neglected in the analysis of the data because the effect is small compared to the other corrections and contributes a smooth background (except for the small $pp \rightarrow \pi^+ d$ peak); besides, it is difficult to estimate the magnitude of the background accurately. Ordinarily one expects that pions would constitute a significant background, with kaons and deuterons produced much less copiously. In our case, however, the proton spectra of interest lie near the kinematic limit of pion production, so that pion background is either kinematically impossible or strongly suppressed by the small phase space available. A similar argument applies to the kaon background. Figure 12 shows where the pion kinematic limit occurs in terms of N* missing mass for the kinematic conditions of this experiment. Since the N* missing mass is below 2000 MeV for almost all of our data, the above argument is justified. This conclusion is verified by a few direct measurements of the pion background which were made in the course of the experiment.

B. Analysis of Elastic Data

Our data on elastic proton-proton scattering provide valuable checks of our absolute normalization, missing mass resolution, and kinematic measurement accuracy. The use of the peak positions to generate a correction to the kinematics has already been outlined. This section describes how elastic cross sections and resolution estimates are obtained from the elastic peaks.

Figure 13 shows a typical set of runs taken at the elastic peak. In order to determine the number of counts in each peak, a small smooth background must be subtracted; to check the resolution at the center of the hodoscope, the true intensity distribution normal to the hodoscope elements (before "binning" into hodoscope elements) should be estimated. Both of these purposes are achieved, in a manner similar to our subsequent analysis of the inelastic spectra, by the following procedure.

It is assumed that the true peak intensity distribution is a Gaussian in M_4, centered at M_o and of width Γ. The background is represented by a polynomial $P(M_4)$. With these assumptions the number of counts in hodoscope element ℓ centered at $M_{4\ell}$ and of mass width Δ_ℓ is given by

$$y_\ell = P(M_{4\ell}) + A \int_{M_{4\ell} - \Delta_\ell/2}^{M_{4\ell} + \Delta_\ell/2} \exp\left[- (M_4 - M_o)^2 / 2\Gamma^2 \right] dM_4 . \quad (34)$$

This function is fitted to the measured data by a least-squares fitting program with A, M_o, Γ, and the polynomial coefficients as variable parameters. The order of the polynomial is adjusted to obtain the best fit. Then Γ is the observed resolution at the elastic peak, and the number of elastically scattered protons is obtained by subtracting the polynomial from the data in the neighborhood of the peak.

The proton-proton elastic differential cross sections resulting from this experiment are presented in Fig. 14 and Table 4. The uncertainties given are compounded from statistical errors, uncertainties resulting from random errors in the kinematic variables (including t), and, when applicable at 7 GeV/c, the aforementioned random errors of

10% in the incident beam intensity (cf. Section II B). The errors given do not include the estimated error of 7% in the absolute normalization.

In Figure 15 our elastic cross sections at 3, 5, and 7 GeV/c are compared with the results of Clyde(21) at corresponding momenta. The agreement is sufficiently good to give confidence in our normalization. Quantitative interpretation of our elastic cross sections is postponed to Section V for comparison with the inelastic results.

The observed elastic peak widths are compared with our estimated resolution in Fig. 16. The full widths at half-maximum are shown. There is some disagreement, but the discrepancies are not serious; the main contributions to loss of resolution in the inelastic spectra usually come from chromatic aberrations and/or from the finite mass width of a single hodoscope element.

C. Combination of Inelastic Runs into Composite Mass Spectra

After the analysis of individual runs described in Section III A, the next step in the reduction of inelastic data is to combine the data into composite missing mass spectra at constant p_1 and θ_3. There is usually considerable overlapping of adjacent runs, which provides another self-consistency check.

In combining the data, it is found that the data from the ends of the hodoscope are consistently in error, presumably because of small errors in aperture location, nonuniform distribution of background on the hodoscope, and similar effects; for this reason data from hodoscope elements 1 - 4 (at the top of the hodoscope) and from element 28 have been rejected.

An additional correction is necessary in order to obtain the mass spectra at constant angle. This correction to the cross section compensates for slight variations in the lab angle over the spectrum. These variations are caused primarily by variations in θ_3 on the hodoscope for a single run (see Section II D) and secondarily by slight changes in the corrected central θ_3 from run to run. Although the variations are small, they contribute a significant effect because of the strong dependence of the cross section on θ_3. In particular, the systematic variation of θ_3 over the hodoscope leads to systematic discrepancies in the uncorrected data for the mass regions where runs overlap.

The compensation for this effect is accomplished as follows. Let $f(\theta)$ be the differential cross section at constant p_1 and M_4, and let θ_o be the nominal angle at which the spectrum is desired. Expanding in a Taylor series to second order about θ_o, we obtain

$$f(\theta) = f(\theta_o) + f'(\theta_o)\,(\theta - \theta_o) + 1/2f''(\theta_o)\,(\theta - \theta_o)^2. \quad (35)$$

The observed cross section g is given by the integral of $f(\theta)$ over the detector, whose angular response is represented by a normalized weight function $w(\theta)$:

$$\begin{aligned} g &= \int f(\theta)\, w(\theta)\, d\theta \qquad (36)\\ &= f(\theta_o) + f'(\theta_o) \int(\theta - \theta_o)\, w(\theta)\, d\theta + 1/2f''(\theta_o) \int(\theta - \theta_o)^2\, w(\theta)\, d\theta. \end{aligned}$$

The last two terms constitute the desired correction to the observed cross section g. The derivatives $f'(\theta)$ and $f''(\theta)$ are obtained numerically from the angular dependence of our data at fixed p_1 and

M_4; the integrals are evaluated as a "by-product" of our computer program for calculating solid angles. This correction is of course greatest at our smallest angles; its magnitude is always less than 18%, and the second term is usually small compared to the first, except when the first derivative vanishes. The uncertainty in the correction is estimated to be ± 20% of its magnitude. The importance of the correction is illustrated in Fig. 17, in which a spectrum at small angle is shown before and after the correction is applied.

IV. RESULTS

A. Mass Spectra

In the early stages of this experiment, we measured a few spectra of protons from the N* production reaction (3) up to high missing masses. The results of this exploratory survey are shown in Fig. 18. The absence of pronounced structure in these spectra beyond the peak near 1688 MeV led us to confine the remainder of the experiment to the missing mass region below about 2000 MeV.

The missing mass spectra measured in this latter mass region at 3, 4, 5, 6, and 7 GeV/c are presented in Figures 19-23, respectively, The data of Fig. 18 in this mass interval are repeated for comparison with the other spectra. Note that data taken at 7.0 BeV/c and at 7.1 GeV/c are combined in Fig. 23. The errors shown include statistical errors, which are usually about 1%,and the estimated uncertainty in the variable θ_3 correction, which was discussed in Section III C.

The solid curve associated with each spectrum is the nonresonant background as estimated by the fitting procedure to be described in Section IV C.

Some qualitative observations on the form of the spectra can be made. The enhancements near 1512 and 1688 MeV are strongly excited at all our angles for all incident momenta except 3 GeV/c. The 1238 MeV peak, on the other hand, decreases rapidly as either the incident energy or the momentum transfer increases. At our momentum transfers, we find no independent evidence for the enhancement near 1410

MeV which has been observed at lower momentum transfers$^{(12-16)}$. Finally, at 3 GeV/c we see the enhancement near the kinematic limit that has been attributed$^{(11, 16)}$ to detection of the decay protons from N*(1238) isobars produced with nucleons.

B. Breit-Wigner Fits

To obtain a quantitative measure of the nucleon isobar effects in our data, we make least-squares fits to the spectra, using a sum of Breit-Wigner resonant forms plus a polynomial representing the nonresonant background:

$$\frac{d^2\sigma}{dM_4^{\ 2}dt}(M_4) = P(M_4) + \sum \frac{H_\ell}{(M_\ell - M_4^{\ 2}) + (\Gamma_\ell/2)^2}. \qquad (37)$$

In this equation, H_ℓ, M_ℓ, Γ_ℓ, and the coefficients of the polynomial $P(M_4)$ are variable parameters; the sum extends over the number of peaks in the spectrum. Peaks near 1238, 1512, and 1688 MeV are used provided that such peaks are apparent in the data. The order of the polynomial is increased until a satisfactory fit is obtained; in particular, that fit is chosen for which no further significant improvement in chi-square is obtained by increasing the order of the polynomial.

We use a polynomial, rather than the more conventional phase space formula, to represent the background because the composition of the background is sufficiently complex that no simple phase space form can be expected to represent its shape adequately. For example, the aforementioned enhancement near threshold at low incident momentum (caused by the decay protons from the N*(1238)) is a well-known background effect which does not conform to phase space. A polynomial is easy to use and provides a rather general smooth functional behavior.

The simplest type of Breit-Wigner resonant form is used to fit the peaks in the spectra. The use of more complicated Breit-Wigner forms is not justified because our varying resolution somewhat distorts the peak shapes and because in any case the peaks near 1512 MeV and 1688 MeV are probably superpositions of several resonances.

The main results of these fits are sets of parameters - mass M, full width Γ, and height H - which characterize the peaks. A quantitative study of the effects of N* production on the spectra is possible in terms of these parameters.

The first step is to search for dependence of the mass and/or the width of a peak on the incident energy or the momentum transfer. Such shifts could arise from the dynamics of the production and decay of a resonance or from the superposition of more than one resonance at a peak. After unfolding our resolution, no significant dependence of mass or true width on the kinematics of the production process is found.

Since we find no such systematic dependence on the kinematics, we can determine best values of mass and width for the three peaks by averaging our results over all the spectra in which a given peak occurs. In the case of the N*(1238), a correction is necessary for the well-known fact that the peak does not occur at the true mass of the resonance. A correction of 23 MeV for this effect, as estimated by Jackson(22), is applied. The average masses and widths are given in Table 5.

Some discussion of the errors in our mass and width determinations is necessary. In the case of the mass, the position of a peak relative to our missing mass scale is very well determined (~ ± 3 MeV) by the fitting procedure; the dominant uncertainty arises from random errors in the mass scale itself. The magnitude of these errors is estimated from the spread in our proton and deuteron mass determinations (cf. Figures 10(b) and 10(d)) and checked by the self-consistency of the peak masses in our various spectra. The error in the mean quoted in Table 5 is then found in the usual way. For the 1238 MeV peak, an additional uncertainty of ± 5 MeV in the "Jackson correction" is assumed.

Unlike the mass at a peak, the width is not determined precisely by the fitting procedure. The reason is that the polynomial background is too "accommodating": a decrease in the background in conjunction with an increase in the height (and simultaneously the width) of a peak does not greatly affect the goodness of fit. The errors in the widths as estimated by the fitting procedure are typically about 15 MeV. These errors are compounded with the estimated uncertainty in unfolding our resolution before forming the weighted averages of Table 5.

The large and correlated errors in the height and width of a peak would of course be disastrous for our determinations of production cross sections (proportional to height times width) from the Breit-Wigner parameters. This problem is circumvented in the manner described in the next part of this section.

C. Differential Cross Sections for N* Production

To obtain reliable production cross sections from the data, we make additional fits in which the true widths of the peaks are fixed at the average values of Table 5. This procedure considerably reduces the aforementioned uncertainty in the background polynomial. Equation (37) is used as before, with M_l and H_l as variable parameters but with Γ_l held equal to the expected width as calculated from the average width $\overline{\Gamma}$ and from our resolution.

The N* production cross sections are given by the area under the corresponding peaks (when the data are plotted vs. mass squared). These integrals are evaluated from the Breit-Wigner parameters of the fixed-width fits; the errors are propagated from the error matrix of the parameters. The uncertainties in background subtraction are taken into account in this procedure because such uncertainties are reflected in the error matrix. The quoted results at 7.0 and 7.1 GeV/c include an additional uncertainty arising from the random errors in incident beam intensity described in Section II B. Uncertainties in the absolute normalization are not reflected in the quoted data. It is estimated that systematic errors in the incident beam intensity and in our solid angle calculation contribute a ± 7% uncertainty and that errors in the average widths used in our fitting procedure (cf. Table 5) cause an additional ± 10% uncertainty in absolute normalization.

The cross sections are presented in Table 6 and in Fig. 24 (a, b, c). To represent the general trends of the data of Blair _et al._(16) at lower momentum transfers and comparable energies, we have reproduced their fits of the form A exp (-bt) in Fig. 24. In Fig. 25 (a, b, c, d, e) our data are replotted to facilitate comparison of the various N*'s and the elastic cross section at fixed incident momenta.

Some noteworthy features of our cross sections at medium and high momentum transfers are the following. The isospin 1/2 peaks near 1512 and 1688 MeV show quite similar behavior: both are slowly varying as functions of momentum transfer but decrease fairly rapidly with energy; their production cross sections are significantly larger than the elastic cross section at 90° C.M. The 1238 MeV resonance production cross section is, like the elastic cross section, a somewhat steeper function of momentum transfer. These observations are made more quantitative in the next section.

V. DISCUSSION OF RESULTS

A. Comparison with Statistical Model

The interpretation of proton-proton elastic cross sections at high energy is divided naturally into two domains. At low momentum-transfer the differential cross section is dominated by the forward diffraction peak, which is roughly independent of energy; at higher momentum-transfer, the cross section varies less rapidly as a function of momentum-transfer but decreases rapidly with increasing energy. Figures 14 and 15 illustrate this behavior.

The angular restrictions on our data allow us to confine our attention to the high momentum-transfer region. The dependence of the elastic data on energy and momentum transfer in this region suggests a statistical interpretation. The statistical model succeeds at least qualitatively in accounting for the characteristic features of the elastic data(23-25), but recent developments - the absence of Ericson fluctuations(26) and the detailed behavior of the cross sections at $\theta_{cm} = 90^{o}$(21,27) - appear to contradict statistical predictions. Several authors(24,28,29) have called for a direct test of the basic assumption that the various final states of an interaction are produced in proportion to their respective statistical weights. The results of this experiment provide such a "branching ratio" test for the nucleon isobar channels in the final state of proton-proton interactions.

Hagedorn(24) has extended the statistical treatment of proton-proton elastic scattering to arbitrary two-body processes $p + p \rightarrow A + B$ near

$\theta_{cm} = 90$ at high energy. The application of his results to the process $pp \rightarrow pN^*$ leads to the "branching ratio" prediction

$$\left(\frac{d\sigma}{dt}\right)_{pp \rightarrow pN^*} = \left\{ \alpha^2 \left(\frac{2J_{N^*} + 1}{2}\right) \frac{K_{pN^*}}{K_{pp}} \frac{\rho_{pN^*}}{\rho_{pp}} \right\} \left(\frac{d\sigma}{dt}\right)_{pp \text{ elastic}}, \qquad (38)$$

where α is the Clebsch—Gordan coefficient for projecting the final pN^* isospin state on the pure $I = 1$ initial state,

J_{N^*} = spin of the isobar,

$K_{pN^*} = \frac{1}{p^2 E_p E_{N^*}}$, a kinematical factor involving center—of—mass quantities in the final state, and

ρ_{pN^*} = two—body phase space for the pN^* final state. Note that there are no adjustable parameters. There are, however, some ambiguities in comparing the predictions with our results, which we resolve as follows: for the elastic cross section we use measured data rather than the statistical model prediction of Hagedorn(24); and we assume that only the isobars listed in Table 1(a) contribute to our observed peaks at 1512 and 1688 MeV.

In Fig. 26 the predictions are compared with our observed results near $\theta_{cm} = 90^\circ$. The comparison indicates that the model is at least partially successful. Although the absolute normalization is wrong, the energy dependence of the cross sections and the relative amounts of $N^*(1238)$, $N^*(1512)$, and $N^*(1688)$ production are approximately reproduced by the model.

The absence of other peaks from our spectra might be regarded as weak evidence against the statistical model. The N*(1400) and N*(1920) are in mass regions where they could be observed in this experiment; but the cross sections predicted by the statistical model are small. The N*(1400) is suppressed relative to the N*(1512) and N*(1688) by the spin factor and the N*(1920) is suppressed by the isospin Clebsch-Gordan factor. In addition their large widths make them difficult to locate above background. Thus it would be difficult to rule out the possibility of production of N*(1400) and N*(1920) is accordance with the model.

B. Dependence of Cross Sections on Momentum Transfer

In 1964, Orear(17, 18) noticed an interesting regularity in the data then available on proton-proton scattering at high energy. Both the energy dependence and the angular distribution (away from the diffraction peak) could be represented by the simple formula

$$\frac{d\sigma}{d\Omega} = \frac{A}{s} \exp\,(-\,ap_{\perp}), \qquad (39)$$

with $A = 595 \pm 135\ \text{GeV}^2$ mb/sr and $1/a = 158 \pm 3$ MeV/c. In the formula we have

$$s = (\underline{p}_1 + \underline{p}_2)^2 = E_{cm}{}^2 = 4(p^2 + M_p{}^2)$$

and

$p_{\perp} = p \sin \theta_{cm}$, the transverse momentum transfer.

The fact that equation (39) approximately reproduces the exponential dependence on energy of the statistical model at $\theta_{cm} = 90^{\circ}$ suggests that it might be regarded as an empirical extension of the model. Alternatively, Wu and Yang(30) have speculated on the theoretical interpretation of the Orear formula in terms of an extended internal structure of the proton.

Recently, more precise data on proton-proton elastic scattering have cast doubt on the validity of the Orear formula. The angular distributions of Clyde(21), Allaby *et al.*(26) and the present experiment indicate that the slope parameter, a, of equation (39) is not constant but depends on energy in the manner indicated in Fig. 27; and the energy dependence of the data of Akerlof *et al.*(27) at 90° is in marked disagreement with the formula. The latter authors find that $\frac{d\sigma}{dt}$ is well represented by the sum of two exponentials in $p_{\perp}^2$; they point out, however, that the persistence of this behavior at high energy would violate the analyticity bound of Cerulus and Martin(31) and Kinoshita(32).

In view of these developments, it seems best to use our data to search for empirical regularities. First we must choose a suitable independent variable. A difficulty in using $p_{\perp}$ (or $p_{\perp}^2$) for inelastic two-body processes is that if we define $p_{\perp}$ as the final-state transverse momentum, $p_{\perp}$ is not the same for the inverse process.

A suitable generalization of $p_{\perp}^2$ is suggested by expressing $p_{\perp}^2$ for elastic scattering in terms of the Mandelstam variables t and u:

$$t = (\underline{p}_1 - \underline{p}_3)^2 = -2p^2\,(1 - \cos\theta) \qquad (40)$$

and

$$u = (\underline{p}_1 - \underline{p}_4)^2 = -2p^2\,(1 + \cos\theta). \qquad (41)$$

Thus we have

$$p_{\perp}^{2} = p^{2} \sin^{2}\theta = \frac{-tu}{t + u} \qquad (42)$$

for elastic proton–proton scattering.

For inelastic processes, the function $v = [-tu/(t + u)]$ retains the following desirable properties that $p_{\perp}^{2}$ manifests for elastic scattering:

(1) it is symmetric under interchange of the initial–state protons,

(2) it takes the same value for the inverse process,

and (3) it reduces to $(-t)$ for small t.

Furthermore, we find that a function of the form

$$\frac{d\sigma}{dt} = B \exp\,(- v/v_{o}) \qquad (43)$$

usually provides a good fit to our cross sections at fixed energy, as is shown in Fig. 28–31.

The slopes of these fits vary systematically with energy and depend on the particular reaction under consideration in the manner shown in Fig. 32. An understanding of these variations must await a detailed theory applicable at intermediate energies. But a striking feature of Fig. 32 is the tendency of all the slopes toward the same value ($v_{o} \approx 0.4$ GeV^{2}) at the upper end of our energy range. This may be a manifestation of a welcome trend toward simplicity at high energy.

ACKNOWLEDGMENTS

I am grateful to Prof. L. T. Kerth for continued guidance and encouragement as director of my thesis research. Prof. Kerth and Drs. Alan R. Clark, Bruce Cork, Tom Elioff, and William A. Wenzel collaborated in the design and execution of the experiment; many technicians of the Lofgren Physics Group contributed to its success. I wish to thank Dr. Edward J. Lofgren for the hospitality of his research group.

The project was expedited by excellent support groups at the laboratory: the various shops, the Bevatron crew, and computer center personnel. Rolland Johnson and Norman Johnson aided considerably in the data analysis.

I am deeply indebted to my wife, Marge, for her cheerfulness, patience, and moral support throughout my graduate shool years.

I am grateful to the National Science Foundation for fellowship support.

APPENDIX A.

EMPIRICAL KINEMATIC CORRECTIONS

Systematic errors in the missing mass at the elastic and $p + p \rightarrow \pi^+ + d$ peaks persist after all known corrections are applied. Hence we infer the presence of small unknown systematic errors in determining p_1, p_3 and θ_3. Superimposed on these systematic effects are smaller random errors due to temporal fluctuations in operating conditions. We use the observed missing masses at the pp elastic and $p + p \rightarrow \pi^+ + d$ peaks to determine the required kinematic corrections independent of the random fluctuations. These peaks are good calibration points because their positions are well-determined and because the pp elastic and πd peaks occur near the limits of the inelastic mass range of interest.

Let unprimed kinematic variables represent measured quantities and primes denote corrected variables. We assume small unknown corrections x_j of the following simple forms:

$$\begin{aligned} p_1' &= p_1 \,(1 + x_j),\ (1 \leq j \leq 5) \\ p_3' &= p_3 \,(1 + x_6), \\ \theta_h' &= \theta_h + x_7, \\ \text{and} \qquad \phi_1 &= \phi_1 \,(1 + x_8). \end{aligned} \tag{A1}$$

The $x_j (1 \leq j \leq 5)$ are separate corrections to p_1 at each nominal incident momentum. We further assume that all the x_j are determined by minimizing the quantity

$$\chi^2 = \sum_\ell \left(\frac{M_\ell(x_j) - M_{o\ell}}{\sigma_\ell} \right)^2 + \sum_j \left(\frac{x_j}{\sigma_j} \right)^2 \tag{A2}$$

In this expression $M_i(x_j)$ is the peak mass calculated from the corrected kinematics and M_{oi} is the known proton or deuteron mass; the σ_i are estimated random mass errors and the σ_j are the expected magnitudes of the x_j. This least squares procedure is intended to allow some random fluctuations in the peak masses and to require that the x_j be small. In fact the resulting x_j are reasonable and the mass errors remaining after the corrections appear to be random. Therefore we apply the calculated corrections to our inelastic mass scale.

APPENDIX B

JACOBIAN TRANSFORMATION

In this appendix we derive an expression for the Jacobian transformation J which relates

$$\frac{d^2\sigma}{dM_4^{\,2}d\Omega_L} \text{ to } \frac{d^2\sigma}{dM_4^{\,2}\,dt},$$

$$\frac{d^2\sigma}{dM_4^{\,2}\,dt} = J\left(\frac{M_4^{\,2},\ \Omega_L}{M_4^{\,2},\ t}\right)\frac{d^2\sigma}{dM_4^{\,2}d\Omega_L}. \qquad (B\ 1)$$

To express J in terms of laboratory kinematics, first note that

$$J\left(\frac{M_4^{\,2},\ \Omega_L}{M_4^{\,2},\ t}\right) = 2\pi\ J\left(\frac{M_4^{\,2},\ \cos\theta_3}{M_4^{\,2},\ t}\right) \qquad (B\ 2)$$

To evaluate J, it is easiest to express $M_4^{\,2}$ and t in terms of the independent variables p_3 and θ_3 in the lab system:

$$\begin{aligned} M_4^{\,2} &= (\underset{\sim}{p}_1 + \underset{\sim}{p}_2 - \underset{\sim}{p}_3)^2 \\ &= m_1^{\,2} + m_2^{\,2} + m_3^{\,2} + 2(E_1m_2 - E_3m_2 - E_1E_3 + p_1p_3\cos\theta_3) \qquad (B\ 3) \\ \text{and } t &= (\underset{\sim}{p}_1 - \underset{\sim}{p}_3)^2 \\ &= m_1^{\,2} + m_3^{\,2} - 2(E_1E_3 + p_1p_3\cos\theta_3), \qquad (B\ 4) \end{aligned}$$

where the $\underset{\sim}{p}_i$ are four-vectors.

Using well-known properties of Jacobians, we can write

$$J\left(\frac{M_4^{\,2},\ \cos\theta_3}{M_4^{\,2},\ t}\right) = J\left(\frac{M_4^{\,2},\ \cos\theta_3}{p_3,\ \cos\theta_3}\right) \Big/ J\left(\frac{M_4^{\,2},\ t}{p_3,\ \cos\theta_3}\right). \qquad (B\ 5)$$

The numerator is just

$$J\left(\frac{M_4^2,\ \cos\theta_3}{p_3,\ \cos\theta_3}\right) = \left(\frac{\partial M_4^2}{\partial p_3}\right)_{\theta_3} = 2\left[\ p_1 \cos\theta_3 - (E_1 + m_2)\beta_3\ \right] \qquad \text{(B 6)}$$

The denominator simplifies via straightforward algebra to

$$J\left(\frac{M_4^2,\ t}{p_3,\ \cos\theta_3}\right) = -\ 4\ m_2 p_1 p_3 \beta_3 . \qquad \text{(B 7)}$$

Using equations (B 2), (B 5), (B 6), and (B 7), we obtain finally

$$J\left(\frac{M_4^2,\ \Omega_L}{M_4^2,\ t}\right) = \frac{\pi\ [(E_1 + m_2)\beta_3 - p_1\ \cos\theta]}{m_2 p_1 p_3 \beta_3} . \qquad \text{(B 8)}$$

APPENDIX C. SOLID ANGLE CALCULATION

The calculation of the laboratory solid angle subtended by each hodoscope element uses the well-known ray-tracing method wherein the rays are represented by 5-component vectors and the beam optical elements are represented by matrices.(33) The matrix representations of the optical elements (magnets and drift spaces) are adapted from those of Devlin(34). In this method the components of a ray vector $\vec{x} = (x, x', y, y', \Delta p/p)$ are the deviations of the ray in position, direction, and momentum from the central ray. The vector $\vec{x}_C$ upon exit from any element is given by

$$\vec{x}_C = A\vec{x}_B , \tag{C 1}$$

where $\vec{x}_B$ is the vector at the entrance and A is the matrix representing the beam element. The effect of a set of elements on a ray is then given by the product of the matrices of the set.

In our case, let $\vec{x}_T$ and $\vec{x}_H$ be vectors representing a ray at the target and at the hodoscope, respectively, and let A be the matrix connecting them. Neglecting chromatic aberrations and vertical source size ($y_T \equiv 0$), the intersection (x_H, y_H) of a ray with the hodoscope plane is determined by the momentum and the horizontal direction x_T' at the target:

$$y_H = A_{35}(\Delta p/p), \tag{C 2}$$

and

$$x_H = A_{12}\, x_T' + A_{15}(\Delta p/p). \tag{C 3}$$

The computer program determines $\Delta y_T'$, the acceptance interval of vertical directions y_T' at the target, for a set of rays equally spaced in x_T, x_T', and Δp. An average $\overline{\Delta y_T'}$ over the target coordinate x_T then gives the average range of y'_T at a given point (x_H, y_H) on the hodoscope. Integrating over a hodoscope element, we obtain the solid angle subtended by the element, averaged over the target:

$$\Delta\,\Omega = \int \overline{\Delta y'_T}\, dx'_T\,. \tag{C 4}$$

This integration is done numerically, using interpolation to find the integrand at points spaced uniformly along the hodoscope element.

The acceptance interval $\Delta y'_T$ for a simple aperture in a field-free region is easy to determine analytically. For example, a circular aperture centered on the beam imposes the requirement

$$x^2 + y^2 \leqq R^2. \tag{C 5}$$

But x and y are linearly related to y'_T by the matrix from the target to the aperture. The limits on y'_T for this aperture are found by substituting these linear relations into the equation of the circle.

The determination of $\Delta y'_T$ for the quadrupole is more difficult. The quadrupole aperture is a right-circular cylindrical pipe centered on the beam line. The difficulty arises because the extreme rays may be those which graze the pipe inside the quadrupole. The grazing condition is specified by the simultaneous requirements

$$x^2 + y^2 \equiv r^2 = R^2 \tag{C 6}$$

and

$$\frac{dr^2}{dz} = 0, \tag{C 7}$$

where z is the coordinate in the beam direction. Let us consider the horizontally convergent quadrupole Q_1, in which the particle orbit can be represented by

$$x = a \cos\,(kz + \delta) \tag{C 8}$$

and

$$y = b \cosh\,(kz + \epsilon). \tag{C 9}$$

Our knowledge of x_T, x'_T, $y_T = 0$, and $\Delta p/p$ at the target enables us to determine a, k, δ, and ϵ in these equations. Substituting Eq.(C 8) and (C 9) into (C 6) and (C 7), we obtain two equations in the two unknowns b and z:

$$a^2 \cos^2 (kz + \delta) + b^2 \cosh^2 (kz + \epsilon) = R^2 \qquad \text{(C 10)}$$

and

$$-a^2 \sin 2[(kz + \delta)] + b^2 \sinh[2 (kz + \epsilon)] = 0. \qquad \text{(C 11)}$$

Solution of (C 11) for b^2 in terms of z and substitution in (C 10) yields an equation in z which is solved numerically. Knowledge of z determines $(y'_T)_{\text{max, min}}$ for the grazing rays. The other quadrupole Q2 is treated similarly. Of course the entrance and exit of the two quadrupoles are treated as ordinary apertures.

After the extreme rays $(y'_T)_{\text{max, min}}$ are found for each aperture, the acceptance interval $\Delta y'_T$ is determined easily for the complete spectrometer.

The solid angle calculation for a run, which includes determination of $\Delta y'_T$ for about 1000 combinations of x_T, x'_T, and $\Delta p/p$ and integration over 28 hodoscope elements, requires about six seconds of CDC 6600 computer time.

REFERENCES

1. Geoffrey F. Chew, Murray Gell-Mann and Arthur H. Rosenfeld, Scientific American 210, 74 (Feb., 1964).
2. Walter H. Barkas and Arthur H. Rosenfeld, Data for Elementary-Particle Physics, UCRL-8030 Rev., April 1963.
3. L. D. Roper, Phys. Rev. Letters 12, 340 (1964)
4. L. D. Roper, R. M. Wright, and B. T. Feld, Phys. Rev. 138, B190(1965).
5. P. Auvil, C. Lovelace, A. Donnachie, and A. T. Lea, Phys. Letters 12, 76 (1964).
6. E. H. Bransden, P. J. O'Donnell, and R. G. Moorhouse, Phys. Letters 11, 339 (1964).
7. P. Bareyre, C. Bricman, and G. Villet, Phys. Rev. Letters 14, 881 (1965).
8. Arthur H. Rosenfeld, Angela Barbaro-Galtieri, Janos Kirz, William J. Podolsky, Matts Roos, William J. Willis, and Charles Wohl, Data for Elementary Particle Physics, Rev. Mod. Phys. (To be published).
9. G. B. Chadwick, G. B. Collins, C. E. Swartz, A. Roberts, S. De Benedetti, N. C. Hien, and P. J. Duke, Phys. Rev. Letters 4, 611 (1960).
10. G. Cocconi, A. N. Diddens, E. Lillethun, G. Manning, A. E. Taylor, T. G. Walker, and A. M. Wetherell, Phys. Rev. Letters 7, 450 (1961).
11. G. B. Chadwick, G. B. Collins, P. J. Duke, T. Fujii, N. C. Hien, M. A. R. Kemp, and F. Turkot, Phys. Rev. 128, 1823 (1962).
12. G. Cocconi, E. Lillethun, J. P. Scanlon, C. A. Stahlbrant, C. C. Ting, J. Walters, and A. M. Wetherell, Phys. Letters 8, 134 (1964).

13. G. Bellettini, G. Cocconi, A. N. Diddens, E. Lillethun, J. P. Scanlon, A. M. Shapiro, and A. M. Wetherell, Phys. Letters 18, 167 (1965).

14. C. M. Ankenbrandt, A. R. Clyde, Bruce Cork, D. Keefe, L. T. Kerth, W. M. Layson, and W. A. Wenzel, Nuovo Cimento 35, 1052 (1965).

15. E. W. Anderson, E. J. Bleser, G. B. Collins, T. Fujii, J. Menes, F. Turkot, R. A. Carrigan, Jr., R. M. Edelstein, N. C. Hien, T. J. McMahon, and I. Nadelhaft, Phys. Ref. Letters 16, 855 (1966).

16. I. M. Blair, A. E. Taylor, W. S. Chapman, P. I. P. Kalmus, J. Litt, M. C. Miller, D. B. Scott, H. J. Sherman, A. Astbury, T. G. Walker, Phys. Rev. Letters 17, 789 (1966).

17. Jay Orear, Phys. Rev. Letters 12, 112 (1964).

18. J. Orear, Phys. Letters 13, 190 (1964).

19. C. M. Ankenbrandt, A. R. Clark, Bruce Cork. T. Elioff, L. T. Kerth, and W. A. Wenzel, IEEE Transactions on Nuclear Science NS-12 No. 4-6, (1965) P. 113, (Proceedings of the Purdue Instrumentation Conference May 12-14, 1965).

20. W. W. Chupp, T. Elioff, and W. A. Wenzel, The Improved Bevatron and Its Performance at High Intensity, UCRL-16228, August 1965, (Presented at Vth International Conference on High Energy Accelerators, Frascati (Italy), September 9-16, 1965).

21. Allan Roy Clyde, Proton-Proton Elastic Scattering at Incidence Momenta 3, 5, and 7 BeV/c, UCRL-16275, 1966.

22. J. D. Jackson, Nuovo Cimento 34, 1644 (1964).

23. G. Fast, R. Hagedorn, and L. W. Jones, Nuovo Cimento 27, 856 (1963).

24. R. Hagedorn, Nuovo Cimento 35, 216 (1965).

25. A. Bialas and V. F. Weisskopf, Nuovo Cimento 35, 1211 (1965).

26. J. V. Allaby, G. Bellettini, G. Cocconi, A. N. Diddens, M. L. Good, G. Matthiae, E. J. Sacharidis, A. Silverman, and A. M. Wetherell, Search for Fluctuations in the Angular Distribution of Proton-Proton Scattering at 16.9 GeV/c. Phys. Letters (To be published).

27. C. W. Akerlof, R. H. Hieber, A. C. Krisch, K. W. Edwards, L. G. Ratner, and K. Ruddick, Phys. Rev. Letters 17, 1105 (1966).

28. H. A. Bethe, Nuovo Cimento 33, 1167 (1964).

29. S. D. Drell, D. R. Speiser, and J. Weyers, Test of Role of Statistical Model at High Energies, in Preludes in Theoretical Physics, edited by A. De-Shalit, H. Feshbach, and L. Van Hove (John Wiley and Sons, Inc., New York, 1966).

30. Tai Tsun Wu and C. N. Yang, Phys. Rev. 137B, 708 (1965).

31. F. Cerulus and A. Martin, Phys. Letters 8, 80 (1964).

32. T. Kinoshita, Phys. Rev. Letters 12, 257 (1964).

33. D. Luckey, In Techniques of High Energy Physics, Part IX, edited by David M. Ritson (Interscience Publishers, Inc., New York, 1961), p. 403.

34. Thomas J. Devlin, Optik-An IBM 709 Computer Program for the Optics of High-Energy Particle Beams, UCRL-9727, 1961.

Table I a. April 1963 values for isobar parameters.

Symbol and Mass (MeV)	Width Γ (MeV)	Spin-parity J^P	Isospin I
N*(1238)	100	$3/2^+$	3/2
N*(1512)	100	$3/2^-$	1/2
N*(1688)	100	$5/2^+$	1/2
N*(1920)	~200	$7/2^+$	3/2

Table I.b. August 1966 values for isobar parameters.

Symbol and Mass (MeV)	Widths (MeV)	Spin-Parity J^P	Isospin I
N*(1236)	120 ± 2	$3/2^+$	3/2
N*(1400)	≈200	$1/2^+$	1/2
N*(1518)	≈ 80	$3/2^-$	1/2
N*(1570)	≈130	$1/2^-$	1/2
N*(1670)	≈180	$1/2^-$	3/2
N*(1688)	≈100	$5/2^-$	1/2
N*(1688)	≈145	$5/2^+$	1/2
N*(1700)	≈240	$1/2^-$	1/2
N*(1920)	≈200	$7/2^+$	3/2

Table II. Characteristics of the spectrometer bending magnets.

Magnet	Type	Plane of bend	Length (in.)	Width of Gap (in.)	Height of Gap (in.)
B_1	"C"	horiz.	36	16	8
B_2	"C"	horiz.	36	16	8
B_3	"H"	horiz.	36	18	8
B_4	"H"	vert.	36	10	18
B_5	"H"	vert.	36	10	18
B_6	"H"	vert.	36	10	18

Table III. Dimensions of the scintillation counters.

Counter	Height (in.)	Width (in.)	Thickness (in.)
S_2	7.5	7.0	.25
H_t	.25	7.0	.50
S_3	7.375	6.75	.25
$\overline{A}$ (dimensions of hole)	7.5	7.5	1.0
$\overline{A}$ (max. outside dimensions)	20.	20.	1.0

Table IV. Differential Cross Sections for $p + p \rightarrow p + p$

Nominal p_1 (GeV/c)	Corrected p_1 (GeV/c)	$-t$ (GeV^2)	$\frac{d\sigma}{dt}$ (mb/GeV^2)
3.0	2.98	0.27	(1.6 ± 0.4)x 10 + 1
	2.98	0.39	(8.9 ± 0.7)x 10 + 0
	2.98	0.58	(3.2 ± 0.2)x 10 + 0
	2.98	0.68	(2.1 ± 0.2)x 10 + 0
	2.98	0.79	(1.48 ± 0.09)x 10 + 0
	2.98	0.94	(1.06 ± 0.05)x 10 + 0
	2.98	0.94	(1.05 ± 0.05)x 10 + 0
	2.98	1.34	(6.3 ± 0.3)x 10 - 1
	2.98	1.75	(4.7 ± 0.3)x 10 - 1
	2.98	1.98	(4.3 ± 0.2)x 10 - 1
4.0	3.98	0.48	(4.9 ± 0.3)x 10 + 0
	4.01	0.49	(4.5 ± 0.3)x 10 + 0
	3.98	0.54	(3.2 ± 0.2)x 10 + 0
	4.01	0.69	(1.6 ± 0.1)x 10 + 0
	4.01	1.18	(3.2 ± 1.0)x 10 - 1
	4.01	1.61	(1.88 ± 0.07)x 10 - 1
	4.01	2.23	(8.7 ± 0.4)x 10 - 2
	4.01	2.85	(5.9 ± 0.2)x 10 - 2
5.0	4.98	0.73	(9.5 ± 0.6)x 10 - 1
	5.01	0.75	(1.05 ± 0.08)x 10 + 0
	5.01	0.75	(1.07 ± 0.08)x 10 + 0
	4.98	0.83	(6.3 ± 0.4)x 10 - 1
	5.01	0.84	(7.1 ± 0.5)x 10 - 1
	4.98	1.03	(3.2 ± 0.3)x 10 - 1
	5.01	1.04	(3.3 ± 0.2)x 10 - 1
	4.98	1.52	(1.0 ± 0.1)x 10 - 1
	4.98	1.76	(6.4 ± 0.5)x 10 - 2
	5.05	1.80	(6.0 ± 0.3)x 10 - 2
	4.98	2.80	(2.1 ± 0.1)x 10 - 2
	4.98	3.08	(1.98 ± 0.07)x 10 - 2
	4.98	3.23	(1.68 ± 0.04)x 10 - 2
	4.98	3.59	(1.5 ± 0.1)x 10 - 2
	4.98	3.64	(1.64 ± 0.04)x 10 - 2
	4.98	3.64	(1.47 ± 0.07)x 10 - 2
	4.98	3.80	(1.9 ± 0.2)x 10 - 2

Table IV. (continued)

Nominal p_1 (GeV/c)	Corrected p_1 (GeV/c)	$-t$ (GeV^2)	$\frac{d\sigma}{dt}$ (mb/GeV^2)
6.0	6.07	1.09	$(2.0 \pm 0.2) \times 10^{-1}$
	6.08	1.23	$(1.23 \pm 0.09) \times 10^{-1}$
	6.08	1.51	$(5.7 \pm 0.3) \times 10^{-2}$
	6.08	1.83	$(2.9 \pm 0.2) \times 10^{-2}$
	6.08	2.18	$(1.7 \pm 0.1) \times 10^{-2}$
	6.08	2.18	$(1.7 \pm 0.2) \times 10^{-2}$
	6.08	2.18	$(1.7 \pm 0.2) \times 10^{-2}$
	6.08	2.51	$(1.21 \pm 0.06) \times 10^{-2}$
	6.08	2.85	$(9.3 \pm 0.6) \times 10^{-3}$
	6.08	3.32	$(6.2 \pm 0.3) \times 10^{-3}$
	6.08	3.90	$(4.5 \pm 0.2) \times 10^{-3}$
	6.08	4.44	$(3.1 \pm 0.2) \times 10^{-3}$
	6.08	4.66	$(3.1 \pm 0.1) \times 10^{-3}$
	6.07	4.66	$(3.0 \pm 0.2) \times 10^{-3}$
	6.07	4.67	$(3.2 \pm 0.1) \times 10^{-3}$
7.0 , 7.1	7.07	1.42	$(5.3 \pm 0.6) \times 10^{-2}$
	7.16	1.58	$(3.4 \pm 0.4) \times 10^{-2}$
	7.16	1.81	$(2.1 \pm 0.2) \times 10^{-2}$
	7.16	2.37	$(7.5 \pm 1.0) \times 10^{-3}$
	7.16	2.71	$(6.2 \pm 0.7) \times 10^{-3}$
	7.08	3.16	$(3.9 \pm 0.5) \times 10^{-3}$
	7.07	4.36	$(1.5 \pm 0.2) \times 10^{-3}$
	7.08	4.46	$(1.1 \pm 0.3) \times 10^{-3}$
	7.08	4.63	$(1.1 \pm 0.3) \times 10^{-3}$
	7.08	5.67	$(6.3 \pm 0.7) \times 10^{-4}$

Table V. Average masses and full widths of spectral peaks.

Symbol	Mass (MeV)	Γ (MeV)
N*(1238)	1240±6	102±4
N*(1512)	1508±2	92±3
N*(1688)	1683±3	110±4

Table VI a. Differential Cross Sections for $p + p \rightarrow p + N^*(1238)$

Nominal p_1 (GeV/c)	Corrected p_1 (GeV/c)	$-t$ (GeV^2)	$\frac{d\sigma}{dt}$ (mb/GeV^2)
3	2.98	0.26	(1.5 ± 0.2)x 10 + 0
	2.98	0.29	(9. ± 1.)x 10 - 1
	2.98	0.37	(9. ± 1.)x 10 - 1
	2.98	0.64	(3.9 ± 0.4)x 10 - 1
	2.98	0.74	(3.9 ± 0.4)x 10 - 1
	2.98	0.88	(3.1 ± 0.3)x 10 - 1
	2.98	1.26	(1. ± 0.2)x 10 - 1
	2.98	1.63	(1.5 ± 0.2)x 10 - 1
4	3.98	0.45	(4.1 ± 0.4)x 10 - 1
	3.98	0.51	(2.5 ± 0.2)x 10 - 1
	4.01	0.64	(1.8 ± 0.2)x 10 - 1
	4.01	1.12	(4.4 ± 0.9)x 10 - 2
	4.01	1.52	(2.4 ± 0.3)x 10 - 2
	4.01	2.12	(2.1 ± 0.2)x 10 - 2
	4.01	2.65	(2.1 ± 0.2)x 10 - 2
5	5.01	0.70	(7.6 ± 0.8)x 10 - 2
	5.01	0.80	(4.3 ± 0.6)x 10 - 2
	5.01	0.99	(2.4 ± 0.3)x 10 - 2
	5.02	1.46	(1.2 ± 0.3)x 10 - 2
	5.05	1.72	(5. ± 1.)x 10 - 3
	4.98	1.91	(9. ± 1.)x 10 - 3
	4.98	2.67	(3.5 ± 0.5)x 10 - 3
	4.98	3.08	(2. ± 1.)x 10 - 3
6	6.08	1.03	(1.1 ± 0.3)x 10 - 2
	6.08	1.16	(1.1 ± 0.3)x 10 - 2
	6.08	1.44	(9. ± 3.)x 10 - 3
	6.08	1.75	(6.6 ± 0.9)x 10 - 3
	6.08	2.08	(5. ± 1.)x 10 - 3
	6.08	2.40	(3.0 ± 0.6)x 10 - 3
	6.08	2.73	(2.1 ± 0.4)x 10 - 3
	6.08	3.18	(9. ± 1.)x 10 - 4
	6.08	3.75	(5. ± 1.)x 10 - 4
	6.08	4.25	(4. ± 2.)x 10 - 4
7, 7.1	7.07	1.33	(8. ± 3.)x 10 - 3
	7.16	1.50	(5. ± 1.)x 10 - 3
	7.16	1.72	(4.2 ± 0.8)x 10 - 3
	7.16	2.27	(2.6 ± 0.9)x 10 - 3
	7.16	2.60	(1.1 ± 0.5)x 10 - 3
	7.08	3.05	(1. ± 0.6)x 10 - 3
	7.07	4.22	(2.5 ± 0.9)x 10 - 4

Table VI b. Differential Cross Sections for $p + p \rightarrow p + N^*(1512)$

Nominal p_1 (GeV/c)	Corrected p_1 (GeV/c)	$-t$ (GeV^2)	$\frac{d\sigma}{dt}$ (mb/GeV^2)
4	3.98	0.44	$(2.5 \pm 0.4) \times 10^{-1}$
	3.98	0.50	$(2. \pm 0.2) \times 10^{-1}$
	4.01	0.62	$(1.5 \pm 0.2) \times 10^{-1}$
	4.01	1.06	$(1.5 \pm 0.2) \times 10^{-1}$
	4.01	1.43	$(1.20 \pm 0.09) \times 10^{-1}$
	4.01	1.99	$(9.2 \pm 0.6) \times 10^{-2}$
	4.01	2.05	$(1.22 \pm 0.09) \times 10^{-1}$
5	5.01	0.67	$(1. \pm 1.) \times 10^{-1}$
	5.01	0.76	$(1.05 \pm 0.09) \times 10^{-1}$
	5.01	0.94	$(8.8 \pm 0.6) \times 10^{-2}$
	5.02	1.38	$(7. \pm 1.) \times 10^{-2}$
	5.05	1.61	$(5.2 \pm 0.6) \times 10^{-2}$
	4.98	1.79	$(5.7 \pm 0.5) \times 10^{-2}$
	4.98	2.49	$(3.7 \pm 0.3) \times 10^{-2}$
	4.98	2.83	$(3. \pm 1.) \times 10^{-2}$
	4.98	2.86	$(3.1 \pm 0.5) \times 10^{-2}$
	4.98	3.14	$(2.5 \pm 0.5) \times 10^{-2}$
6	6.08	0.98	$(6.6 \pm 0.6) \times 10^{-2}$
	6.08	1.10	$(6.3 \pm 0.6) \times 10^{-2}$
	6.08	1.36	$(5.9 \pm 0.8) \times 10^{-2}$
	6.08	1.65	$(3.2 \pm 0.3) \times 10^{-2}$
	6.08	1.97	$(2.8 \pm 0.4) \times 10^{-2}$
	6.08	2.27	$(1.9 \pm 0.2) \times 10^{-2}$
	6.08	2.58	$(1.4 \pm 0.1) \times 10^{-2}$
	6.08	3.00	$(1.07 \pm 0.07) \times 10^{-2}$
	6.08	3.52	$(8.2 \pm 0.6) \times 10^{-3}$
	6.07	3.89	$(7. \pm 1.) \times 10^{-3}$
	6.08	4.02	$(6.4 \pm 0.8) \times 10^{-3}$
7, 7.1	7.07	1.27	$(3.5 \pm 0.5) \times 10^{-2}$
	7.16	1.43	$(2.9 \pm 0.4) \times 10^{-2}$
	7.16	1.64	$(2.0 \pm 0.3) \times 10^{-2}$
	7.16	2.16	$(7. \pm 1.) \times 10^{-3}$
	7.16	2.47	$(7. \pm 1.) \times 10^{-3}$
	7.08	2.89	$(3.2 \pm 0.8) \times 10^{-3}$
	7.07	4.01	$(2.3 \pm 0.4) \times 10^{-3}$
	7.08	5.01	$(1.3 \pm 0.3) \times 10^{-3}$

Table VI c. Differential Cross Sections for $p + p \rightarrow p + N^*(1688)$

Nominal p_1 (GeV/c)	Corrected p_1 (GeV/c)	$-t$ (GeV^2)	$\frac{d\sigma}{dt}$ (mb/GeV^2)
4	3.98	0.47	$(6.6 \pm 0.9) \times 10^{-1}$
	3.98	0.52	$(3.4 \pm 0.3) \times 10^{-1}$
	4.01	0.64	$(4.5 \pm 0.4) \times 10^{-1}$
	4.01	1.05	$(2.3 \pm 0.3) \times 10^{-1}$
	4.01	1.40	$(1.6 \pm 0.1) \times 10^{-1}$
	4.01	1.93	$(1.29 \pm 0.09) \times 10^{-1}$
5	5.01	0.67	$(2.3 \pm 0.2) \times 10^{-1}$
	5.01	0.75	$(1.8 \pm 0.2) \times 10^{-1}$
	5.01	0.92	$(1.2 \pm 0.1) \times 10^{-1}$
	5.02	1.33	$(9. \pm 1.) \times 10^{-2}$
	5.05	1.55	$(7.8 \pm 0.8) \times 10^{-2}$
	4.98	1.73	$(7.4 \pm 0.7) \times 10^{-2}$
	4.98	2.39	$(5.1 \pm 0.4) \times 10^{-2}$
	4.98	2.74	$(4.3 \pm 0.8) \times 10^{-2}$
6	6.08	0.95	$(9.3 \pm 0.8) \times 10^{-2}$
	6.08	1.07	$(8.9 \pm 0.9) \times 10^{-2}$
	6.08	1.32	$(5.8 \pm 0.8) \times 10^{-2}$
	6.08	1.59	$(4.3 \pm 0.4) \times 10^{-2}$
	6.08	1.90	$(2.9 \pm 0.4) \times 10^{-2}$
	6.08	2.18	$(2.0 \pm 0.2) \times 10^{-2}$
	6.08	2.47	$(1.3 \pm 0.1) \times 10^{-2}$
	6.08	2.88	$(1.08 \pm 0.08) \times 10^{-2}$
	6.08	3.38	$(7.7 \pm 0.8) \times 10^{-3}$
	6.08	3.85	$(8. \pm 1.) \times 10^{-3}$
7, 7.1	7.07	1.23	$(5.0 \pm 0.7) \times 10^{-2}$
	7.16	1.38	$(4.5 \pm 0.6) \times 10^{-2}$
	7.16	1.59	$(2.8 \pm 0.4) \times 10^{-2}$
	7.16	2.08	$(1.0 \pm 0.2) \times 10^{-2}$
	7.16	2.38	$(7. \pm 1.) \times 10^{-3}$
	7.08	2.79	$(4. \pm 1.) \times 10^{-3}$
	7.07	3.86	$(2.4 \pm 0.4) \times 10^{-3}$

FIGURE CAPTIONS

Fig. 1. Total cross sections for $\pi^{\pm}p$ scattering as functions of the center-of-mass energy, adapted from Chew et al(1).

Fig. 2. Schematic diagram of the experimental apparatus. In the drawing B_i represent bending magnets, Q_i are quadrupole magnets, S_i are scintillation counters, and C_i are Cerenkov counters. C_1 and C_2 are lowered out of the beam when not in use.

Fig. 3. Details of the hodoscope construction. The structure is periodic with a "cell length" of six elements.

Fig. 4. Trajectories of charged particles through the beam optical system. In the plan view parallel rays are traced; in the elevation view rays emanating from a point on the target are shown. These rays illustrate the focusing conditions for central-momentum particles.

Fig. 5. Coordinate system in the hodoscope plane, looking downstream along the scattered beam direction.

Fig. 6. The mass width ΔM_4 of the central hodoscope element for runs centered at the elastic peak.

Fig. 7. The geometry of the scintillators. S_2 and S_3 are in coincidence with H_i and $\overline{A}$ is in anticoincidence.

Fig. 8. Block diagram of the fast electronics.

Fig. 9. Block diagram of the data acquisition and storage system.

Fig. 10. Illustration of the effect of the empirical kinematic corrections described in Appendix A. Histograms of the missing masses at the pp elastic peaks, before and after the correction,

are shown in (a) and (b) respectively; (c) and (d) are the corresponding histograms for the pp → π^+d peaks.

Fig. 11. The acceptance $\Delta\Omega\ \Delta p/p$ for a central hodoscope element as a function of laboratory angle θ_3. The factor Δp refers to the momentum interval at constant θ_3 on the hodoscope.

Fig. 12. The kinematic limit of pion production in terms of N* missing mass. This is the mass at which a pion peak from the reaction pp → π^+d would occur in our missing mass spectra.

Fig. 13. A typical set of elastic peak runs. These results were obtained at 5 GeV/c at laboratory angles of (a) 10.3°, (b) 12.4°, (c) 16.8°, (d) 22.8°, and (e) 27.4°. Note the changes in the vertical scale.

Fig. 14. Differential cross sections for elastic proton-proton scattering resulting from this experiment.

Fig. 15. Comparison of our elastic data with that of Clyde(21) at (a) 3 GeV/c, (b) 5 GeV/c, (c) 7 GeV/c.

Fig. 16. Resolution (full width at half-max.) at the pp elastic peaks at (a) 3 GeV/c, (b) 4 GeV/c, (c) 5 GeV/c, (d) 6 GeV/c, and (e) 7 GeV/c. The points represent the observed widths of elastic peaks and the curves are estimates of our expected resolution.

Fig. 17. Missing mass spectrum at $p_1 = 7$ GeV/c and $\theta_3 = 10.07°$, (a) before and (b) after the correction described in Section III C.

Fig. 18. Missing mass spectra at (a) $p_1 = 6$ GeV/c, $\theta_3 = 10.26°$, (b) 7 GeV/c. 10.07°, and (c) 7 GeV/c, 13.49°, illustrating the lack of structure above the peak near 1688 MeV.

Fig. 19. Missing mass spectra at 3 GeV/c and laboratory angles of (a) 10.19°, (b) 10.91°, (c) 12.30°, (d) 16.90°, (e) 18.36°, (f) 20.36°, (g) 25.42°, and (h) 30.48°. All the spectra are plotted to the same scale, with successive spectra displaced vertically by equal increments. The solid curves are background estimates calculated with the fitting procedure of Section IV C. The small narrow peak between 1500 and 1600 MeV, especially noticeable in (d) - (f), is attributable to pions from the reaction $pp \rightarrow \pi^+ d$.

Fig. 20. Missing mass spectra at 4 GeV/c and laboratory angles of (a) 10.19°, (b) 10.90°, (c) 12.31°, (d) 16.89°, (e) 20.40°, (f) 25.45°, and (g) 30.55°. All the spectra are plotted to the same scale, with successive spectra displaced vertically by equal increments. The solid curves are background estimates calculated with the fitting procedure of Section IV C.

Fig. 21. Missing mass spectra at 5 GeV/c and laboratory angles of (a) 10.24°, (b) 10.96°, (c) 12.34°, (d) 15.42°, (e) 16.84°, (f) 18.32°, (g) 22.83°, (h) 25.26°, (i) 27.65°, and (j) 29.99°. All the spectra are plotted to the same scale, with successive spectra displaced vertically by equal increments. The solid curves are background estimates calculated with the fitting procedure of Section IV C.

Fig. 22. Missing mass spectra at 6 GeV/c and laboratory angles of (a) 10.26°, (b) 10.95°, (c) 12.34°, (d) 13.86°, (e) 15.42°, (f) 16.84°, (g) 18.32°, (h) 20.31°, (i) 22.81°, (j) 25.27°, and (k) 27.76°. All the spectra are plotted to the same scale, with successive spectra displaced vertically by equal increments.

The solid curves are background estimates calculated with the fitting procedure of Section IV C.

Fig. 23. Missing mass spectra at 7 GeV/c and laboratory angles of (a) 10.07°, (b) 10.59°, (c) 11.48°, (d) 13.49°, (e) 14.65°, (f) 16.44°, (g) 20.58°, and (h) 25.47°. All the spectra are plotted to the same scale, with successive spectra displaced vertically by equal increments. The solid curves are background estimates calculated with the fitting procedure of Section IV C.

Fig. 24. Differential cross sections $d\sigma/dt$ for production of (a) N*(1238), (b) N*(1512), and (c) N*(1688) vs. (-t), the squared four-momentum transfer, at 3, 4, 5, 6, and 7 GeV/c. The straight lines are fits to the data of Blair _et al._(16) at the indicated momenta.

Fig. 25. The differential cross sections for elastic scattering and N* production are repeated here to facilitate their comparison at fixed incident momenta of (a) 3 GeV/c, (b) 4 GeV/c, (c) 5 GeV/c, (d) 6 GeV/c, and (e) 7 GeV/c.

Fig. 26. Comparison of our production cross sections near $\theta_{cm} = 90^\circ$ with the predictions of the statistical model of Hagedorn (24).

Fig. 27. Dependence of the Orear slope parameter of Equation (39) on momentum, according to Clyde(21), Allaby _et al._(26), and the present experiment.

Fig. 28. Differential cross sections for pp elastic scattering vs. $[-tu/(t + u)]$ at (a) 3 GeV/c, (b) 4 GeV/c, (c) 5 GeV/c, (d) 6 GeV/c, and (e) 7 GeV/c. The straight lines are least-squares fits to the data away from the diffraction peak. The reason for this choice of independent variable is explained in the text.

Fig. 29. Differential cross sections for the process $pp \rightarrow pN^*(1238)$ vs. $[-tu/(t + u)]$ at (a) 3 GeV/c, (b) 4 GeV/c, (c) 5 GeV/c, (d) 6 GeV/c, and (e) 7 GeV/c. The straight lines are least-squares fits to all the data.

Fig. 30. Differential cross sections for the process $pp \rightarrow pN^*(1512)$ vs. $[-tu/(t + u)]$ at (a) 4 GeV/c, (b) 5 GeV/c, (c) 6 GeV/c, and (d) 7 GeV/c. The straight lines are least-squares fits to all the data.

Fig. 31. Differential cross sections for the process $pp \rightarrow pN^*(1688)$ vs. $[-tu/(t + u)]$ at (a) 4 GeV/c, (b) 5 GeV/c, (c) 6 GeV/c, and (d) 7 GeV/c. The straight lines are least-squares fits to all the data.

Fig. 32. The slope parameters of the fits shown in Fig. 28 - 31, as functions of the incident momentum.

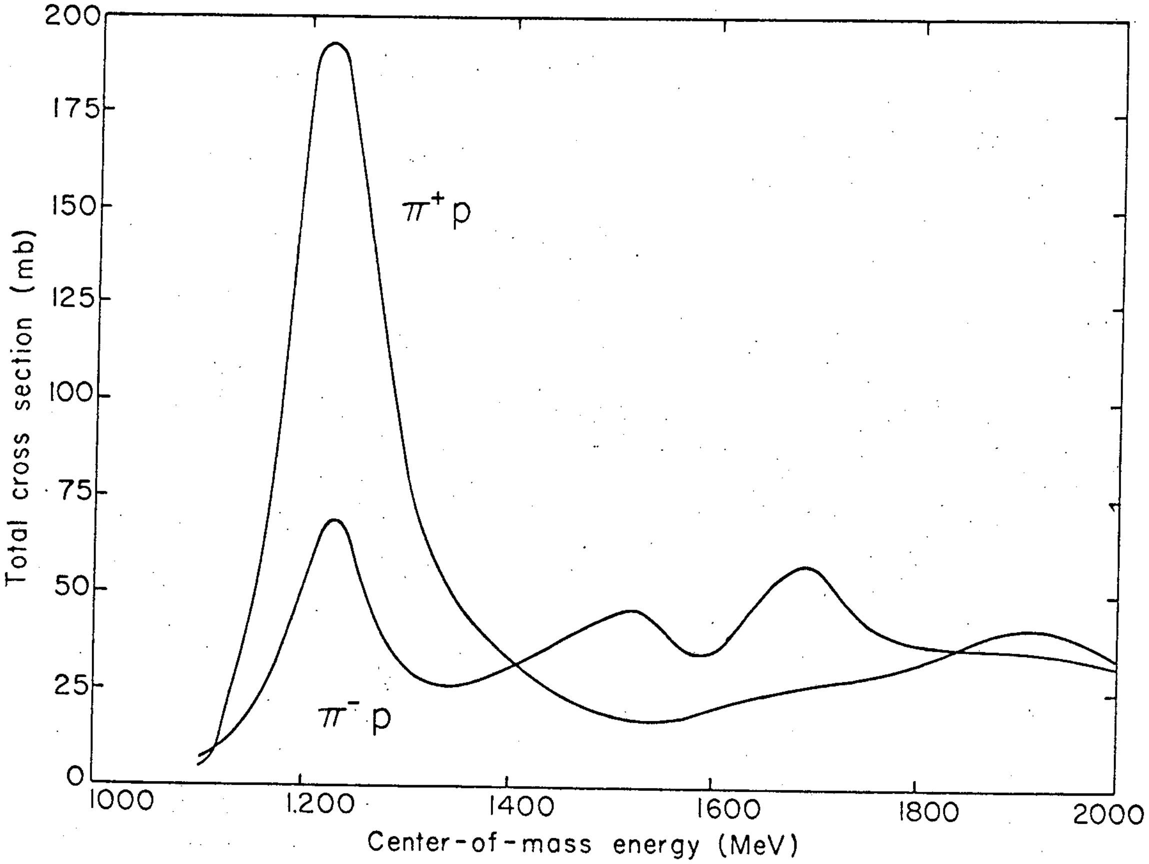

XBL 671-456

Fig. 1

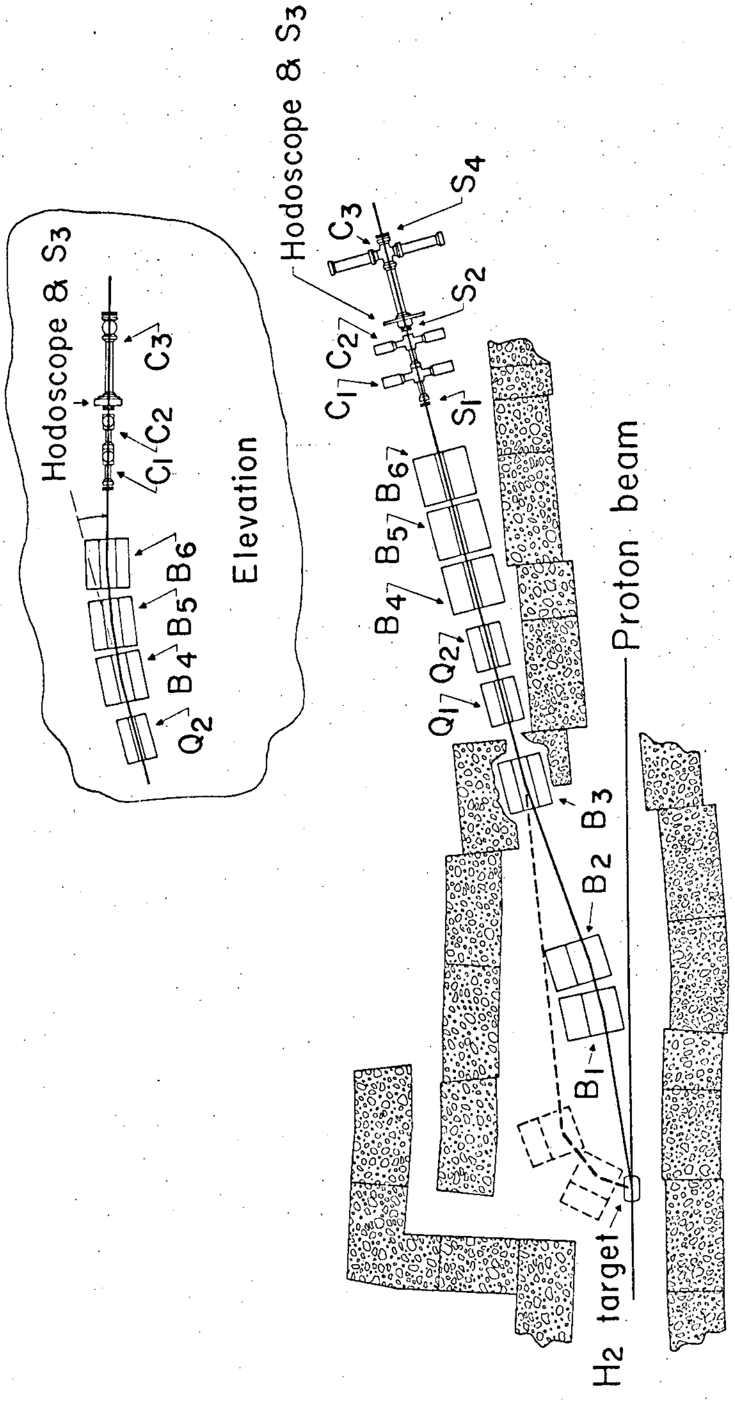

MUB-5979

Fig. 2

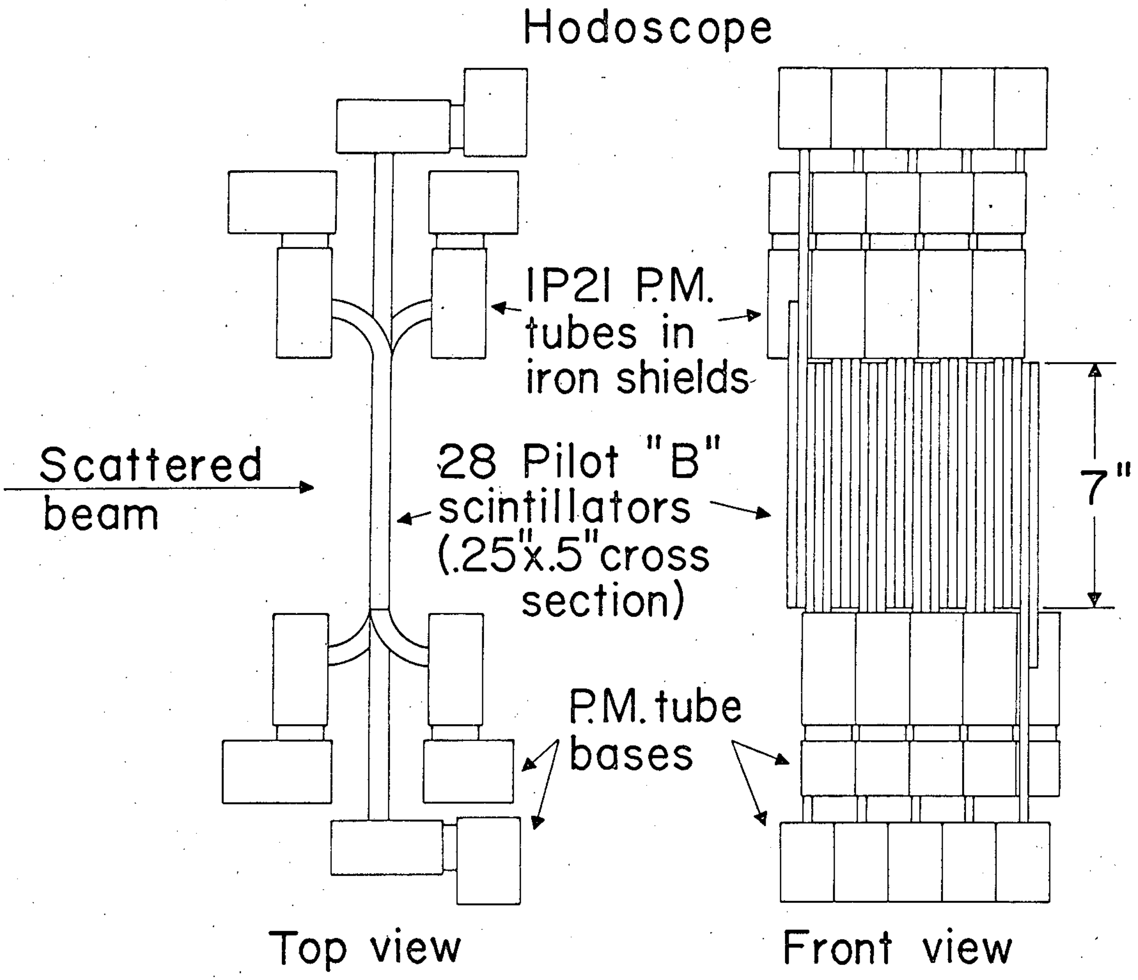
Hodoscope
IP21 P.M. tubes in iron shields
Scattered beam
28 Pilot "B" scintillators (.25"x.5" cross section)
7"
P.M. tube bases
Top view
Front view
XBL 671-469

Fig. 3

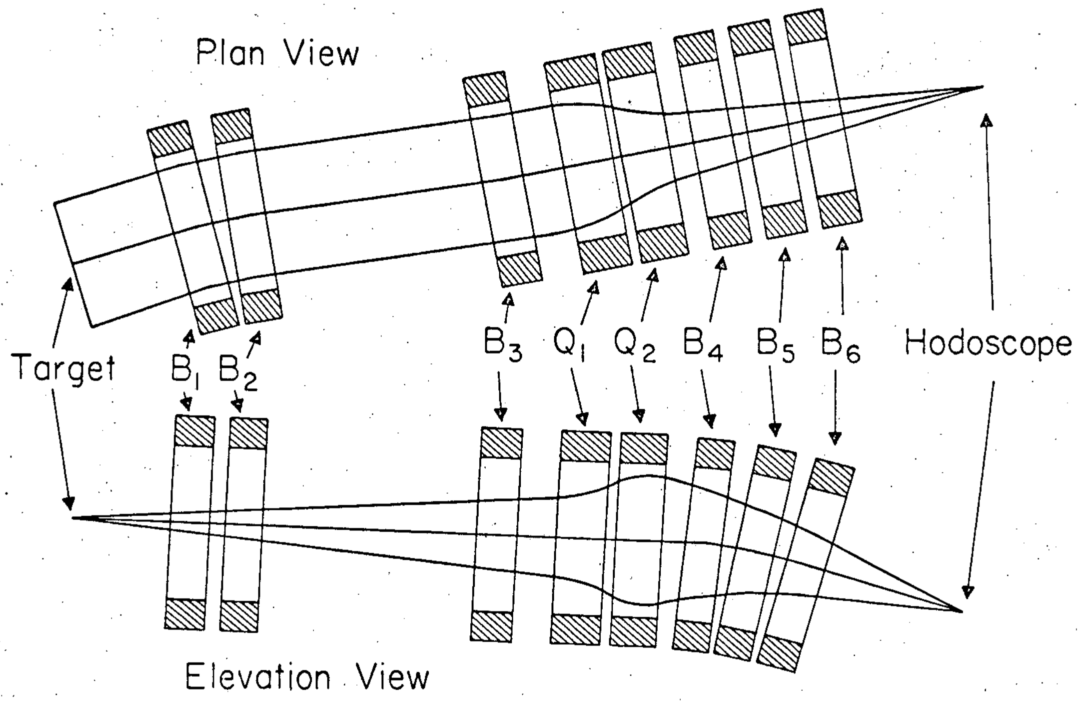

XBL 671-467

Fig. 4

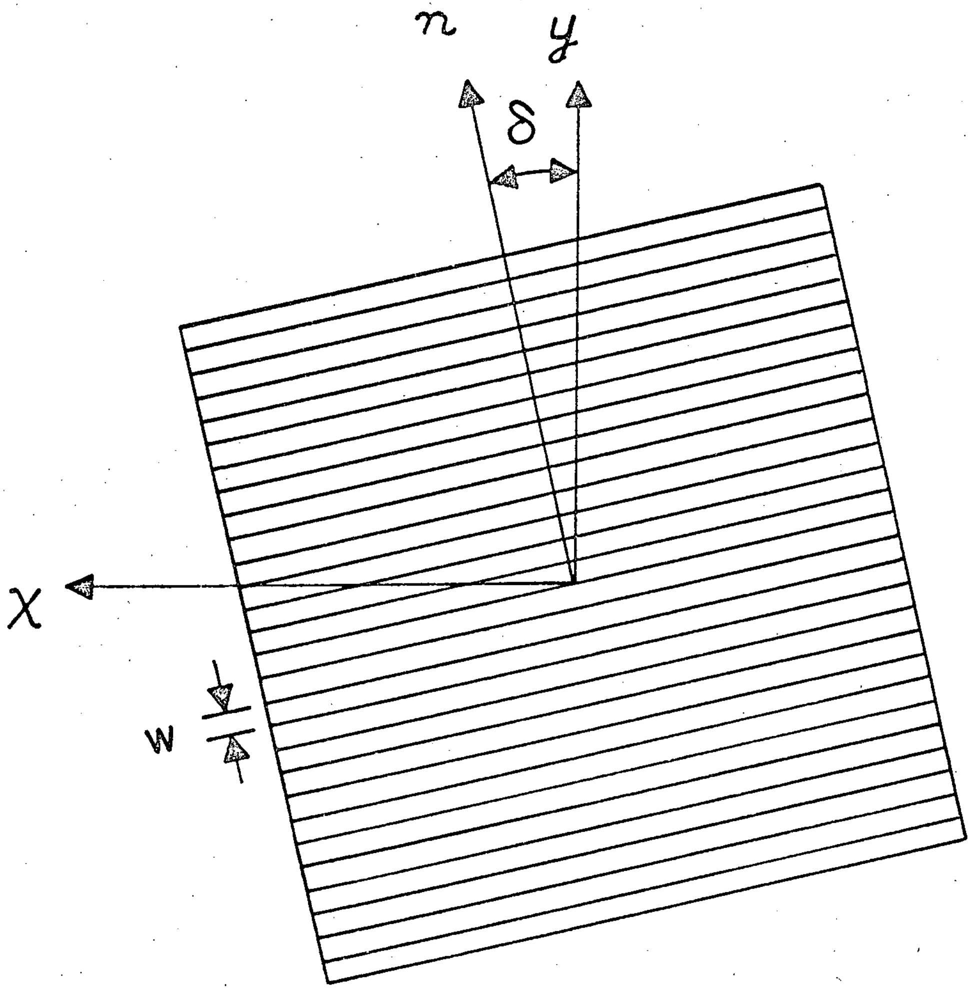

XBL 671-465

Fig. 5

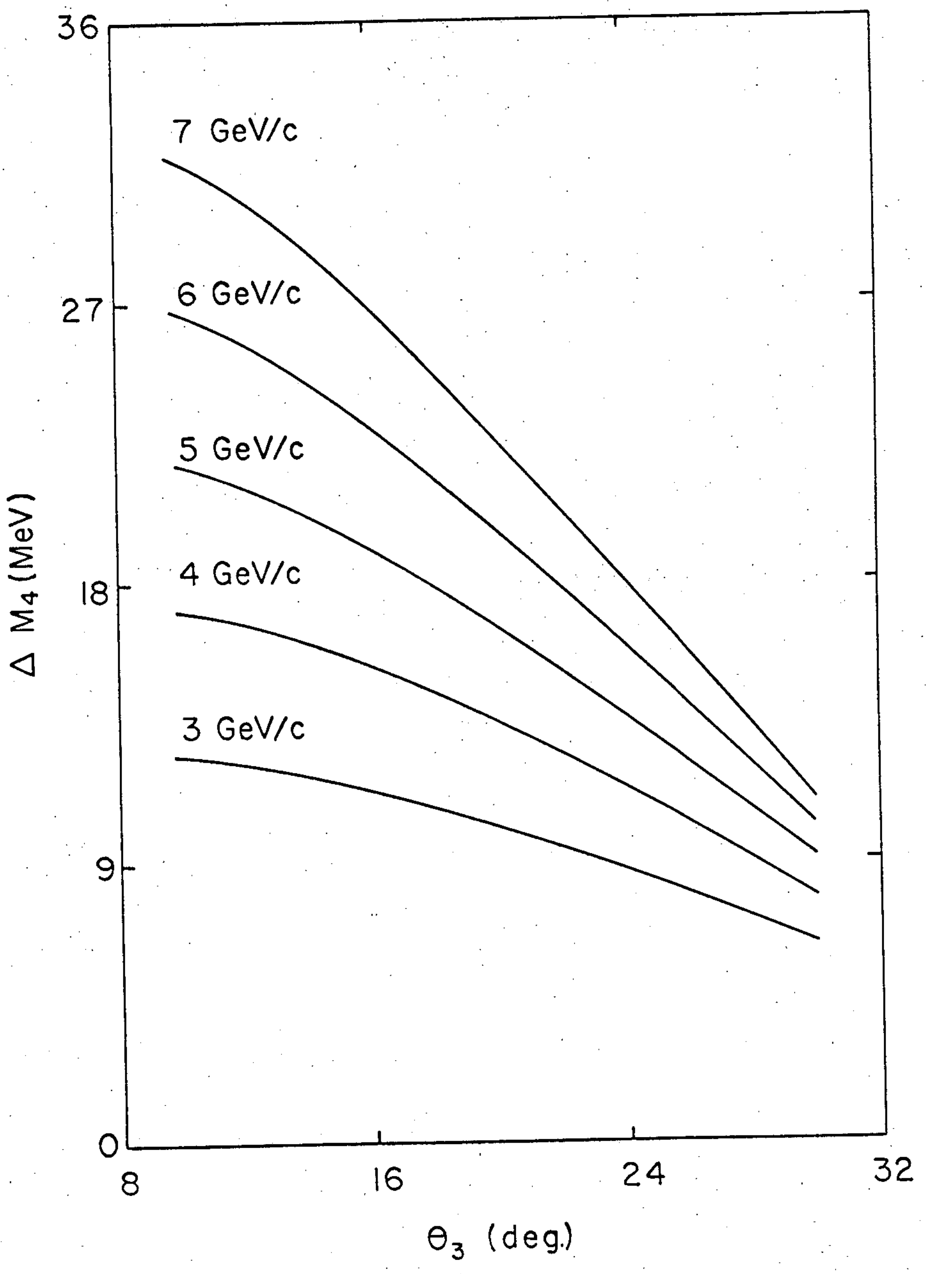

XBL 671-457

Fig. 6

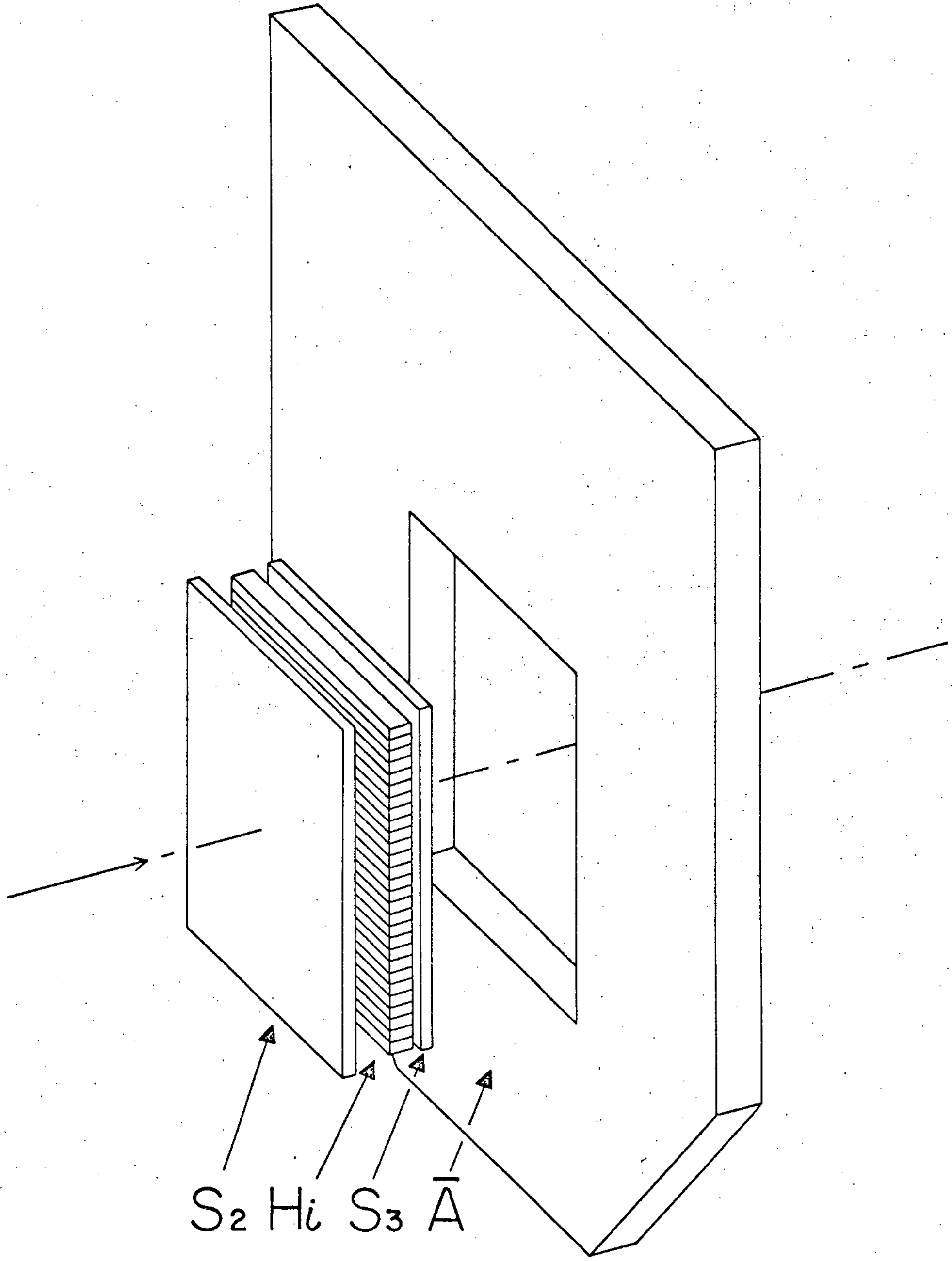

XBL 671-468

Fig. 7

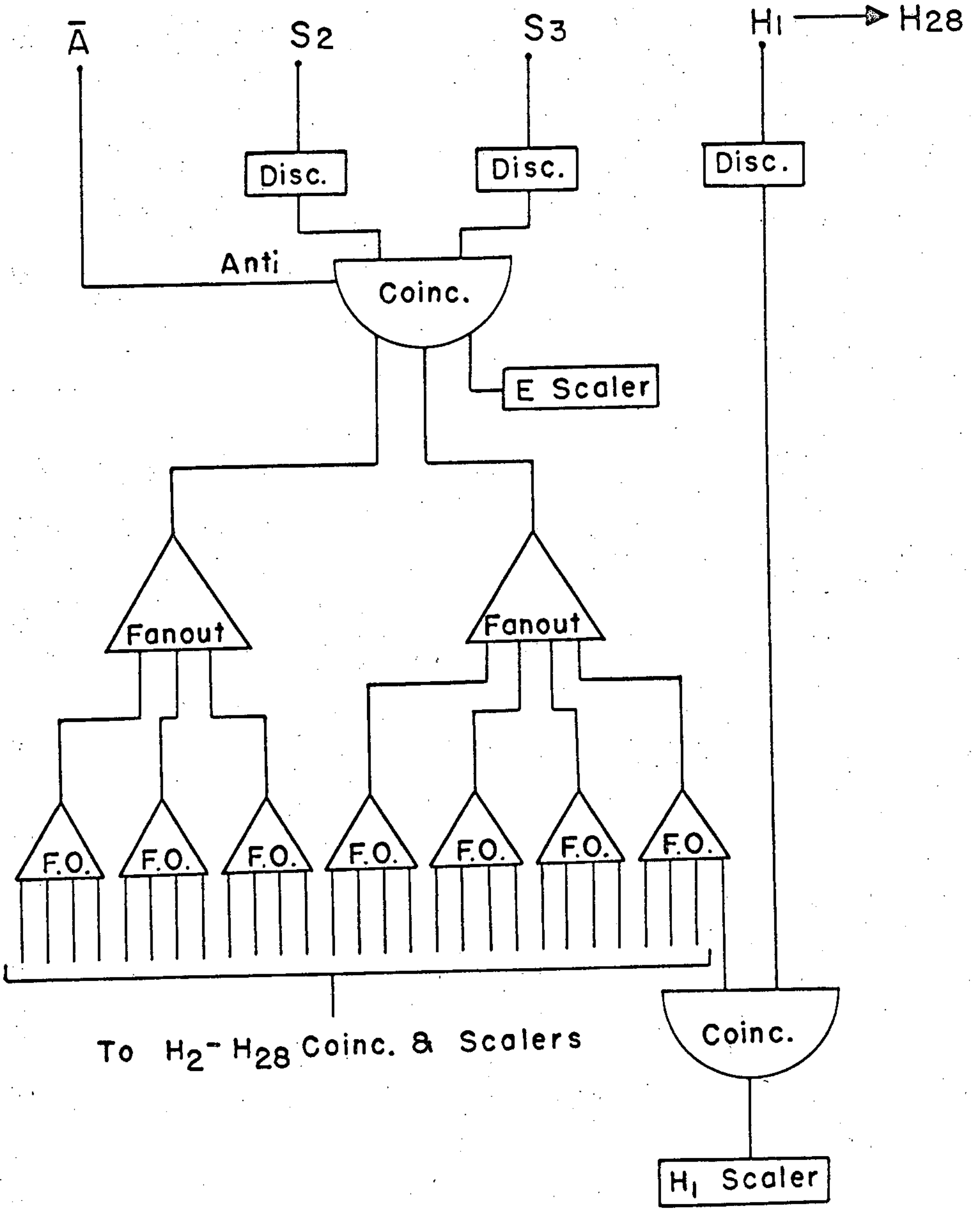

XBL 671-464

Fig. 8

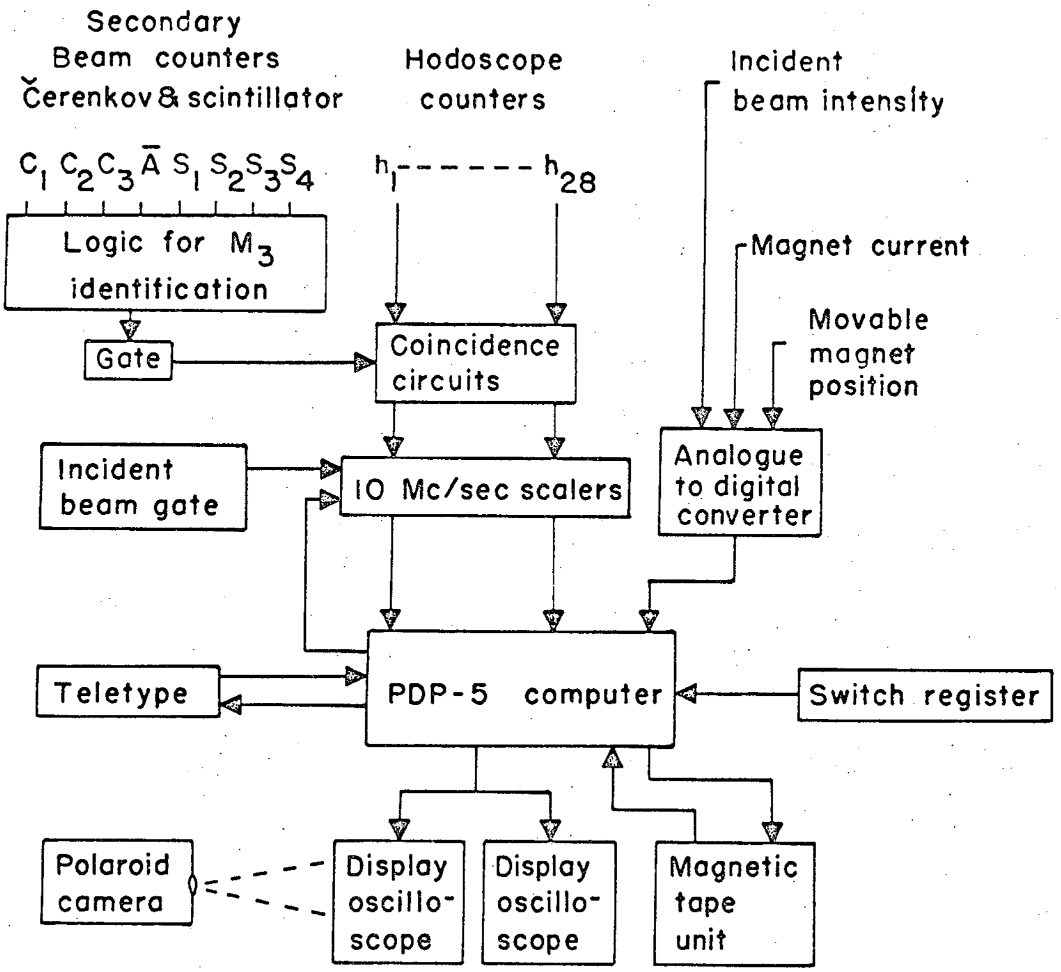

XBL 671-466

Fig. 9

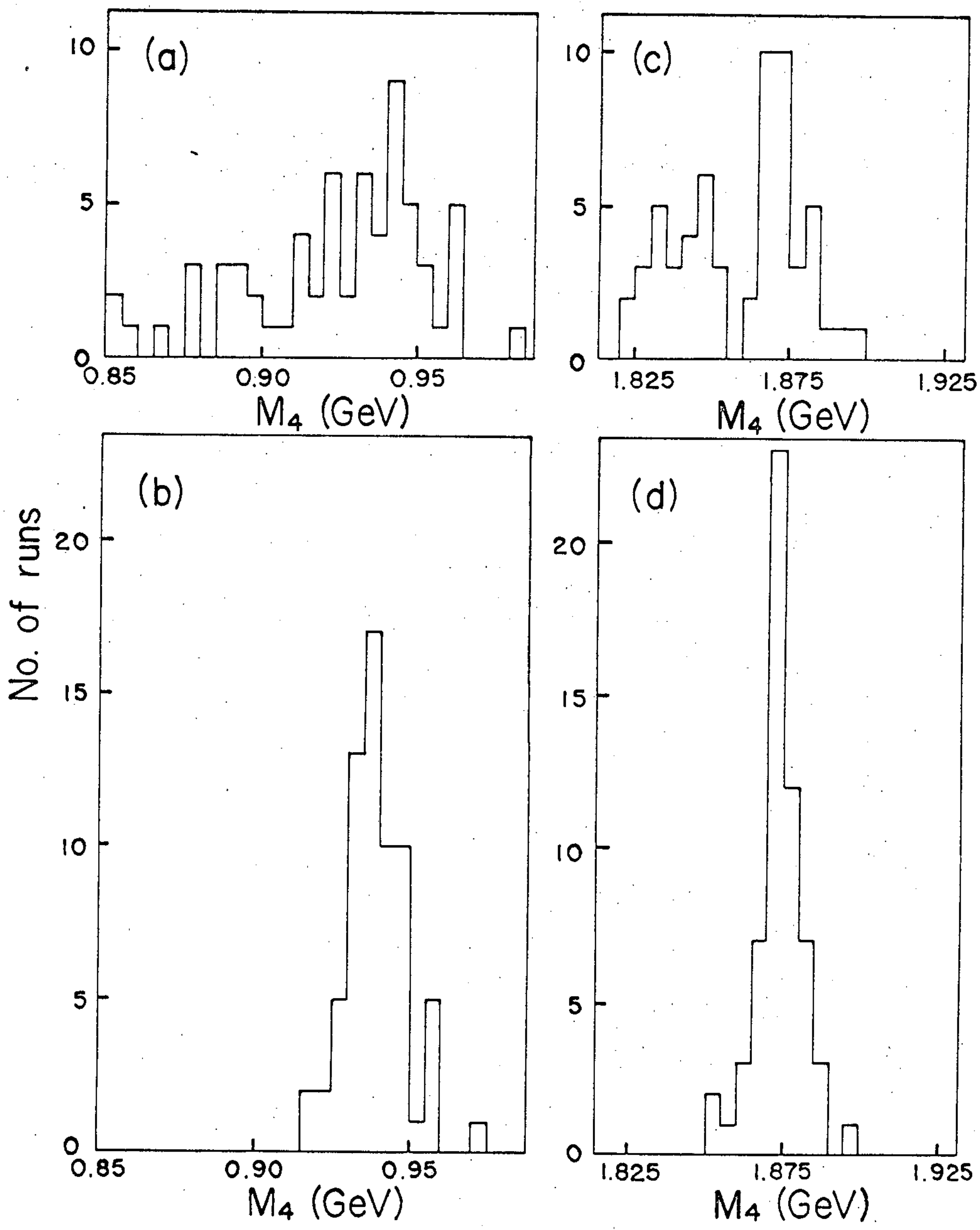

XBL 671-463

Fig. 10

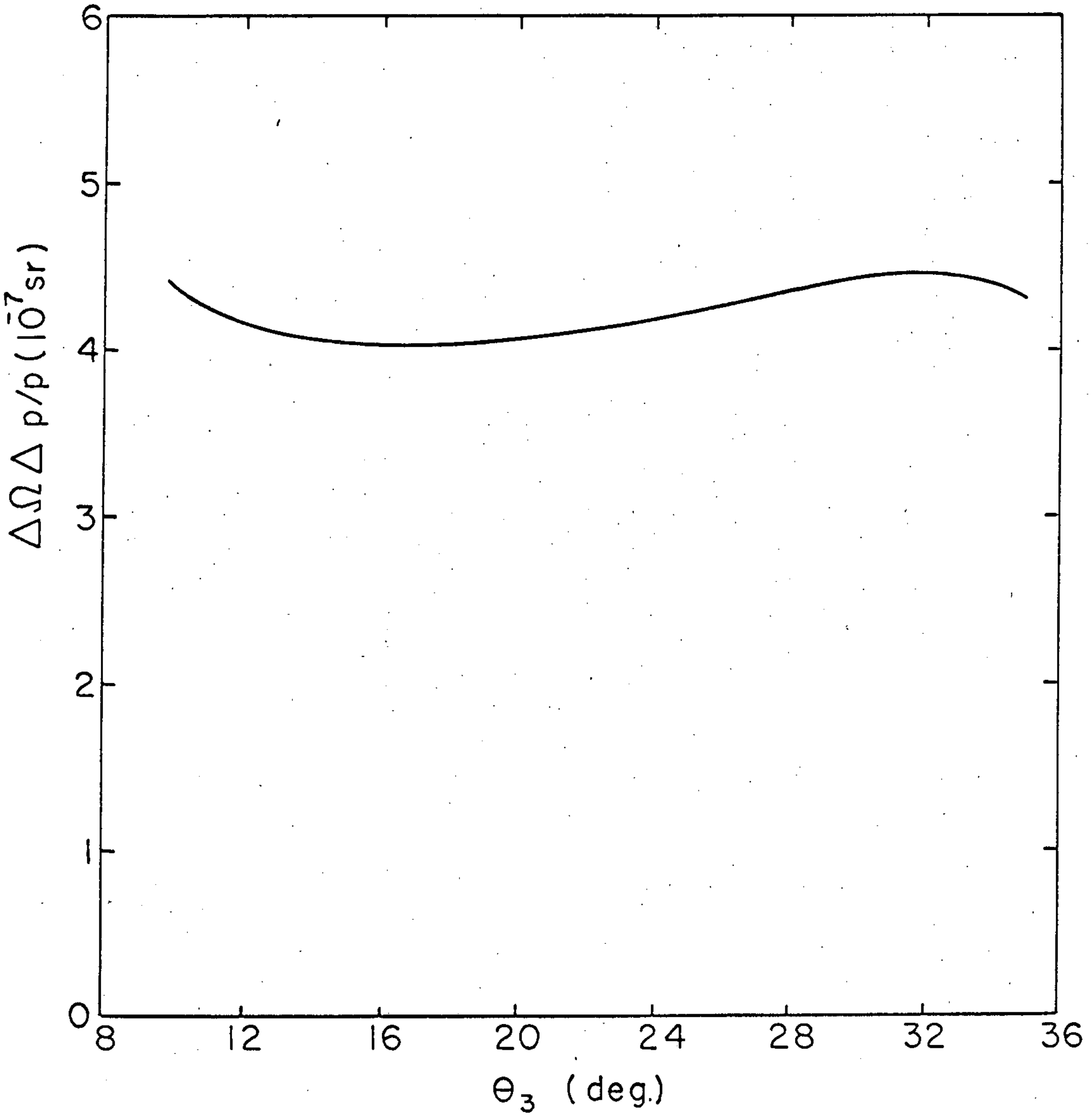

XBL 671-483

Fig. 11

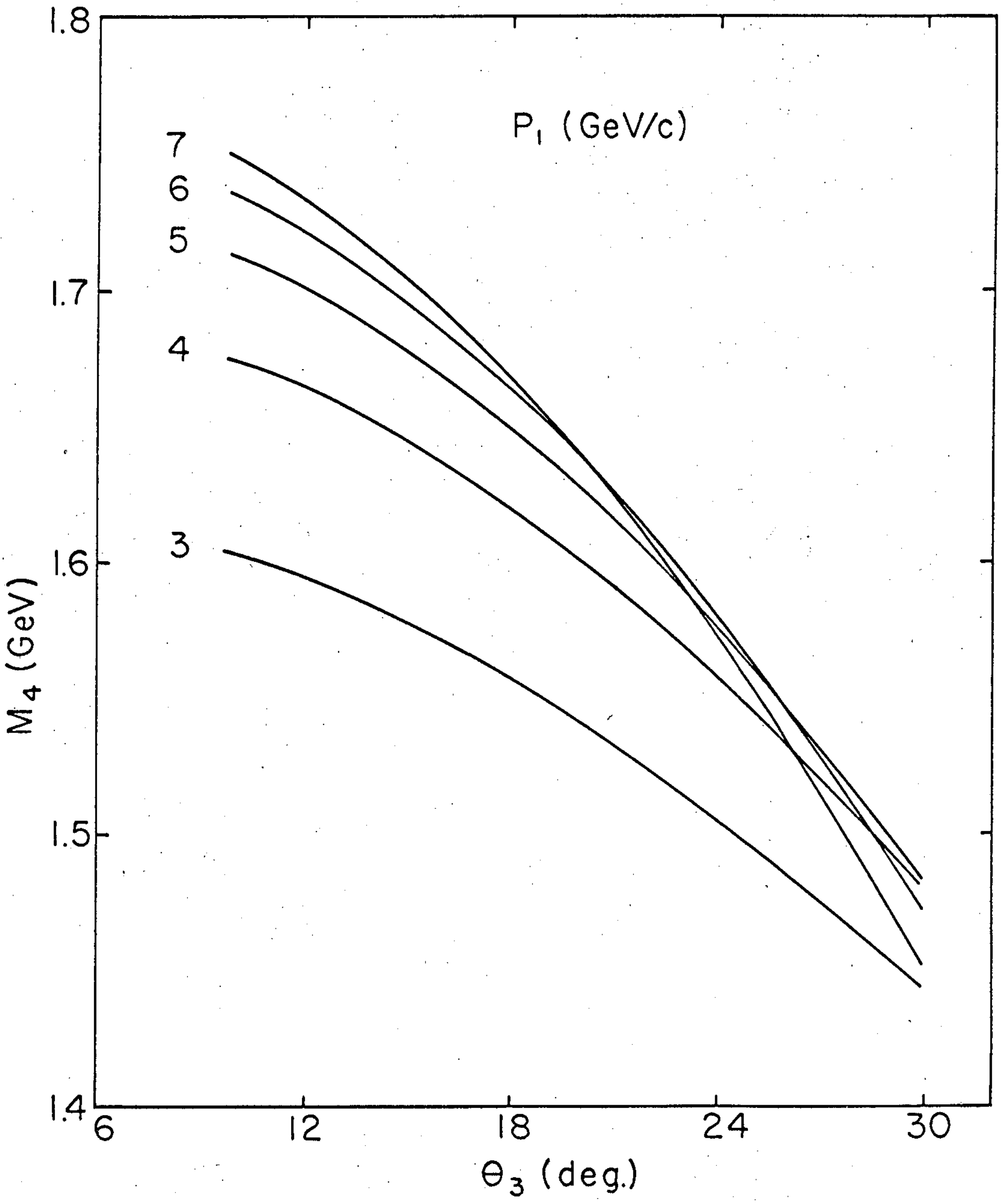

XBL 671-484

Fig. 12

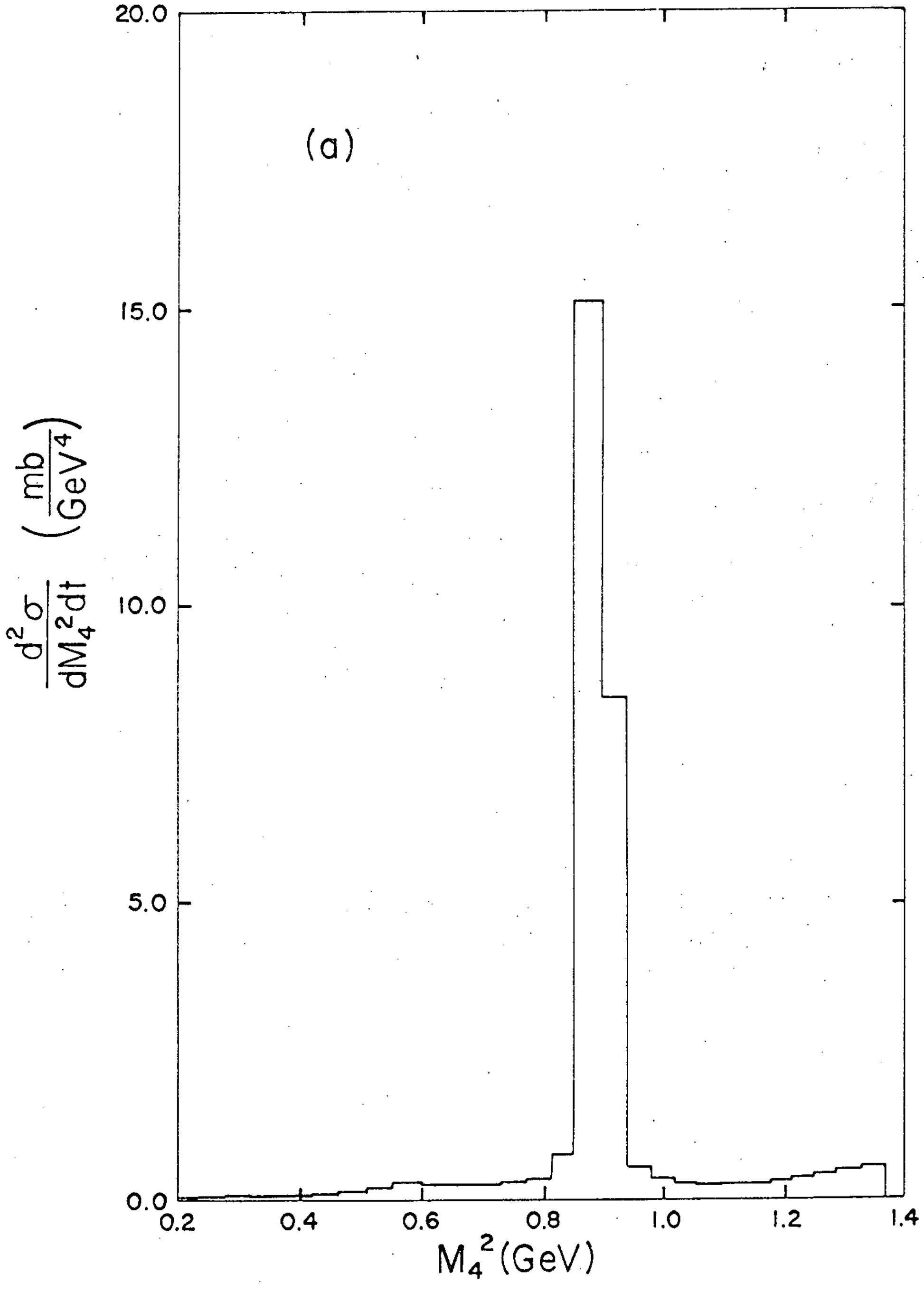

XBL 671=462

Fig. 13(a)

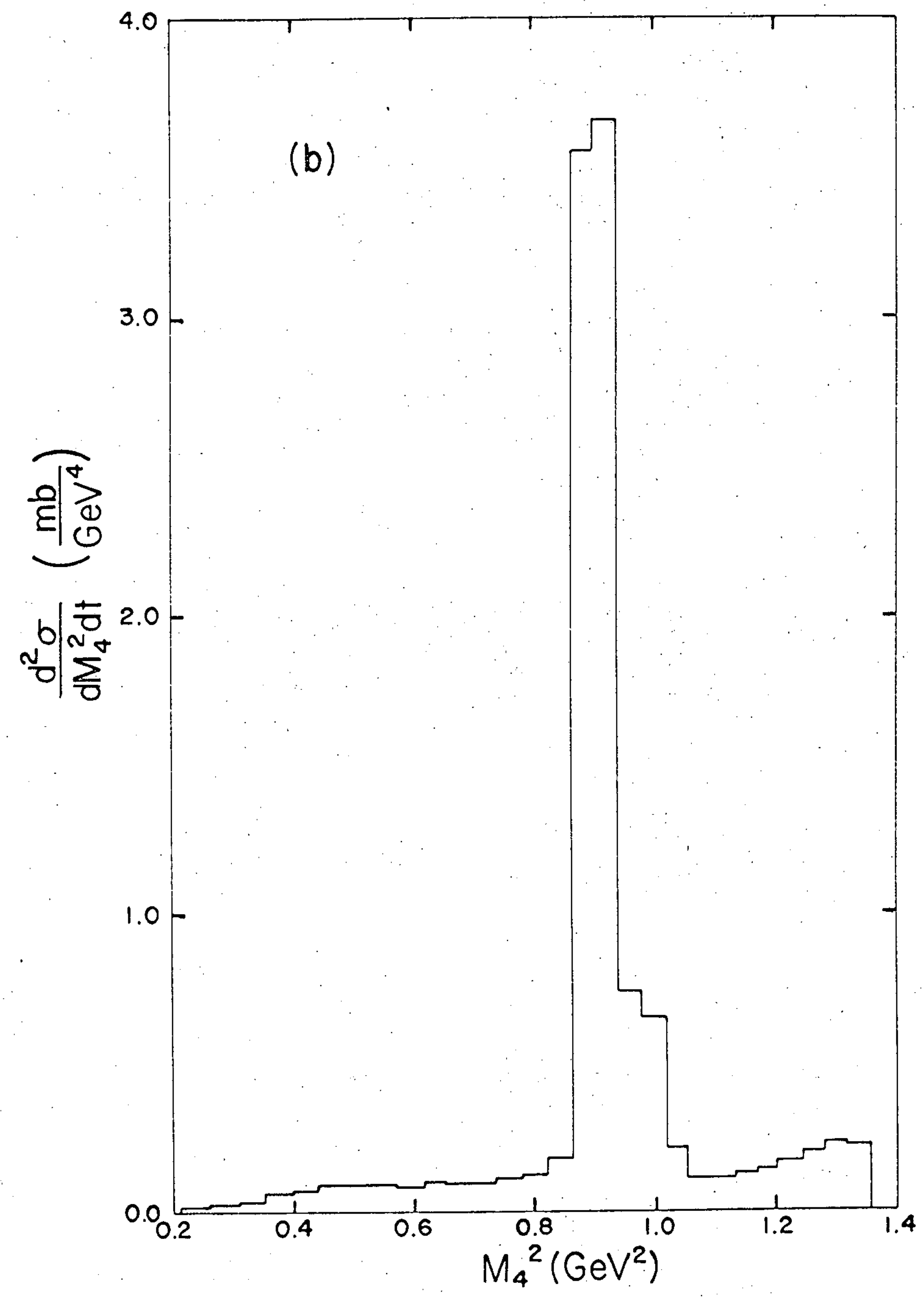

XBL 671 - 461

Fig. 13(b)

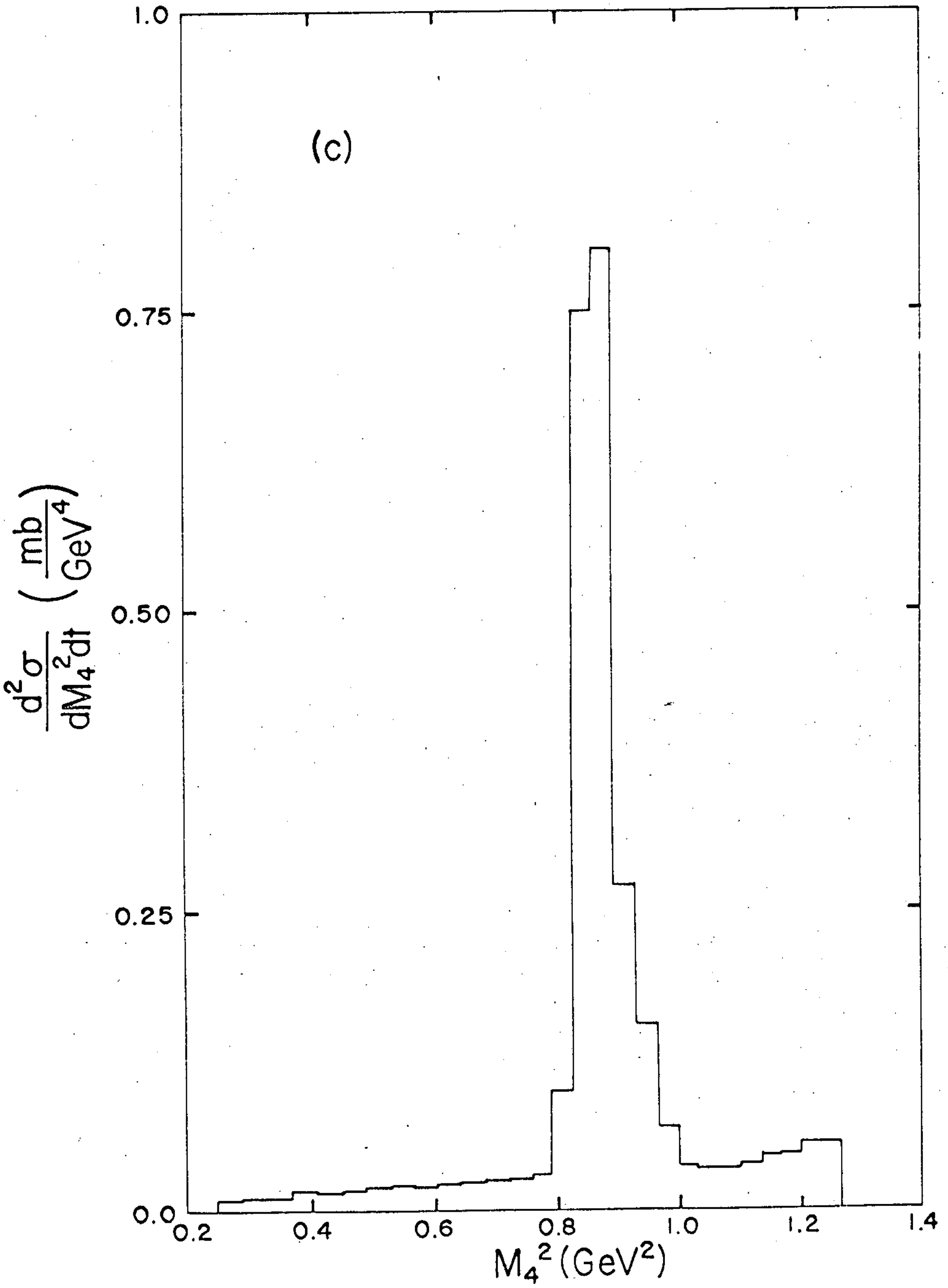

XBL 671-460

Fig. 13(c)

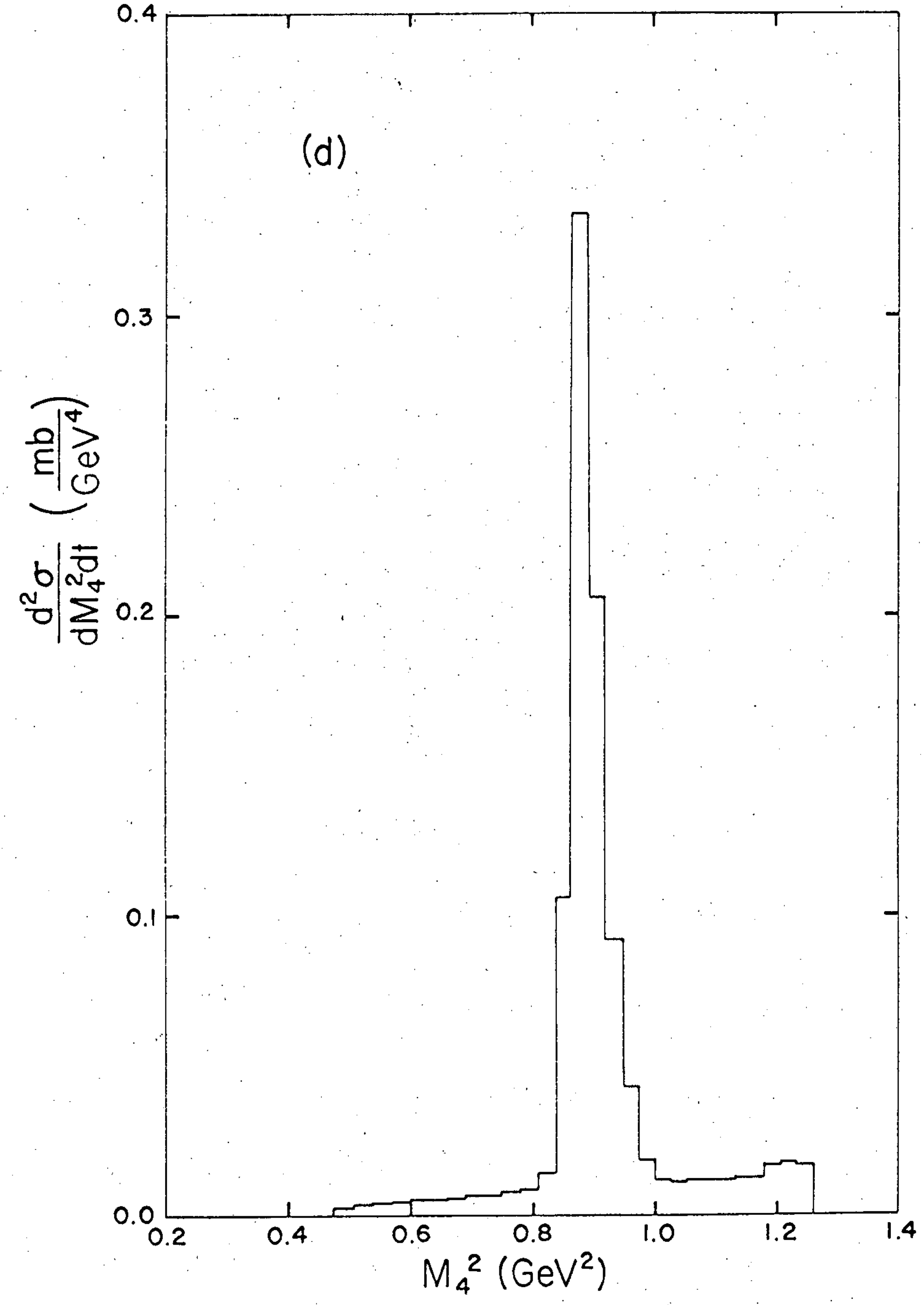

XBL 671-459

Fig. 13(d)

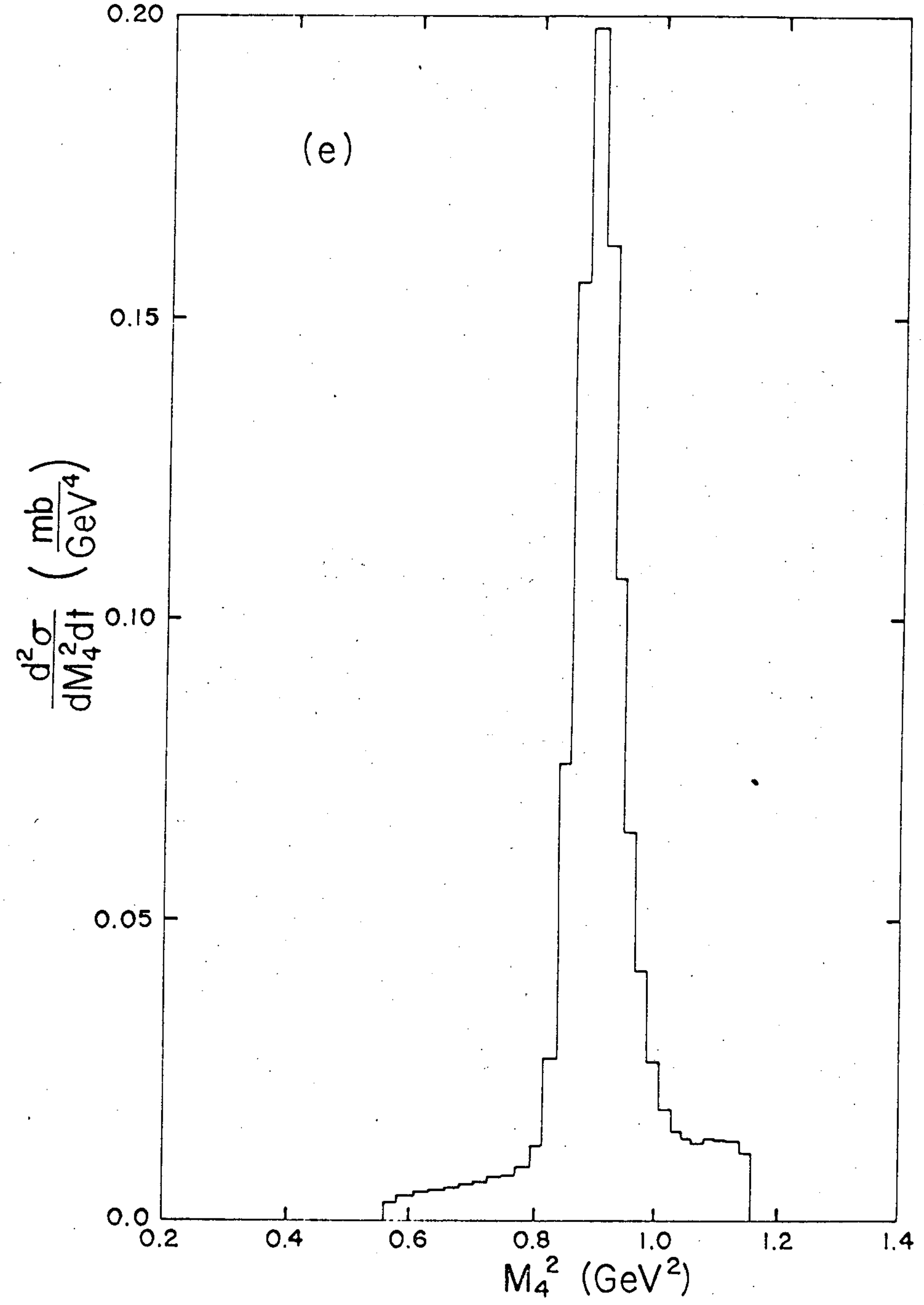

XBL 671-458

Fig. 13(e)

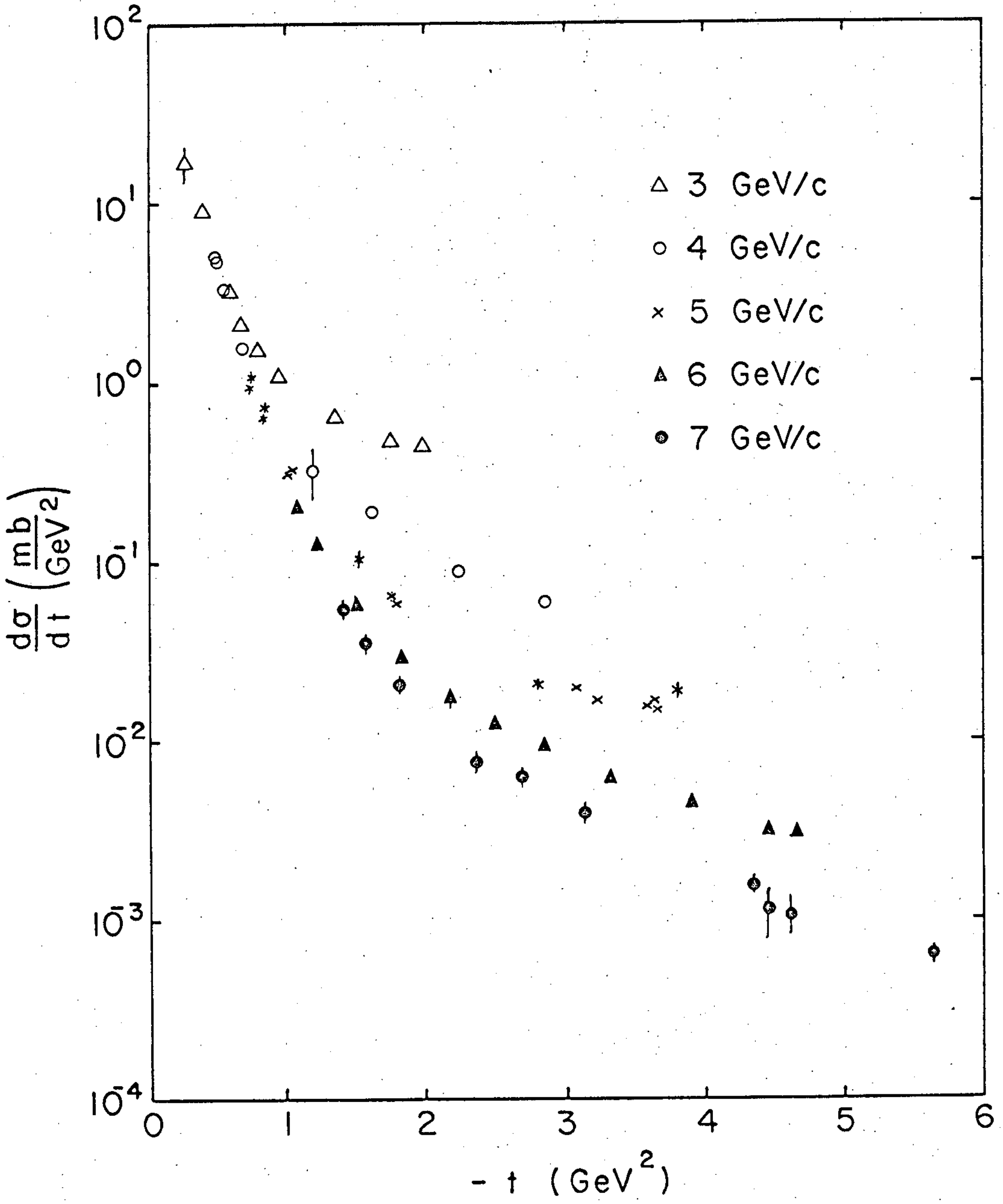

XBL 671-473

Fig. 14

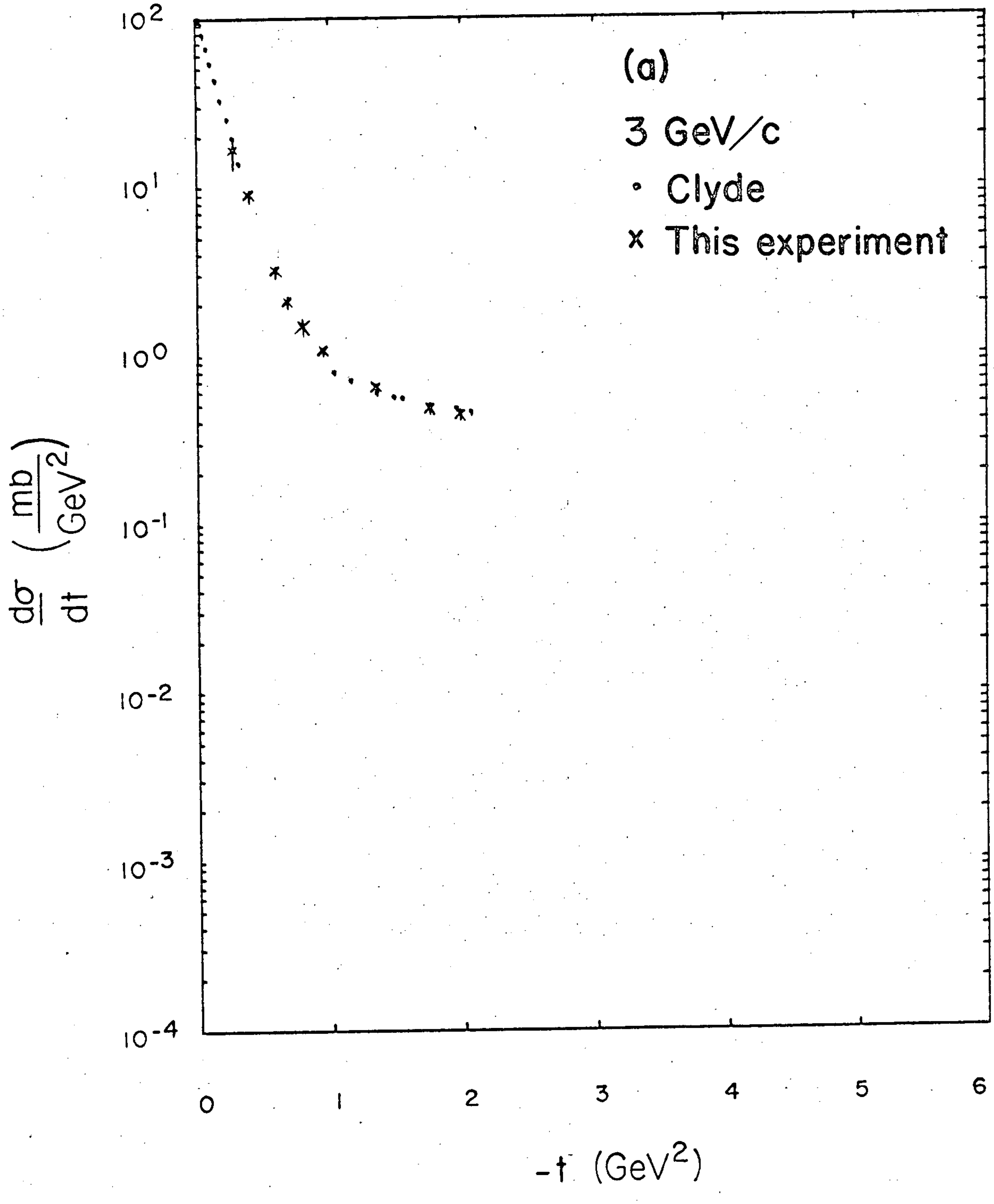

XBL 671-494

Fig. 15(a)

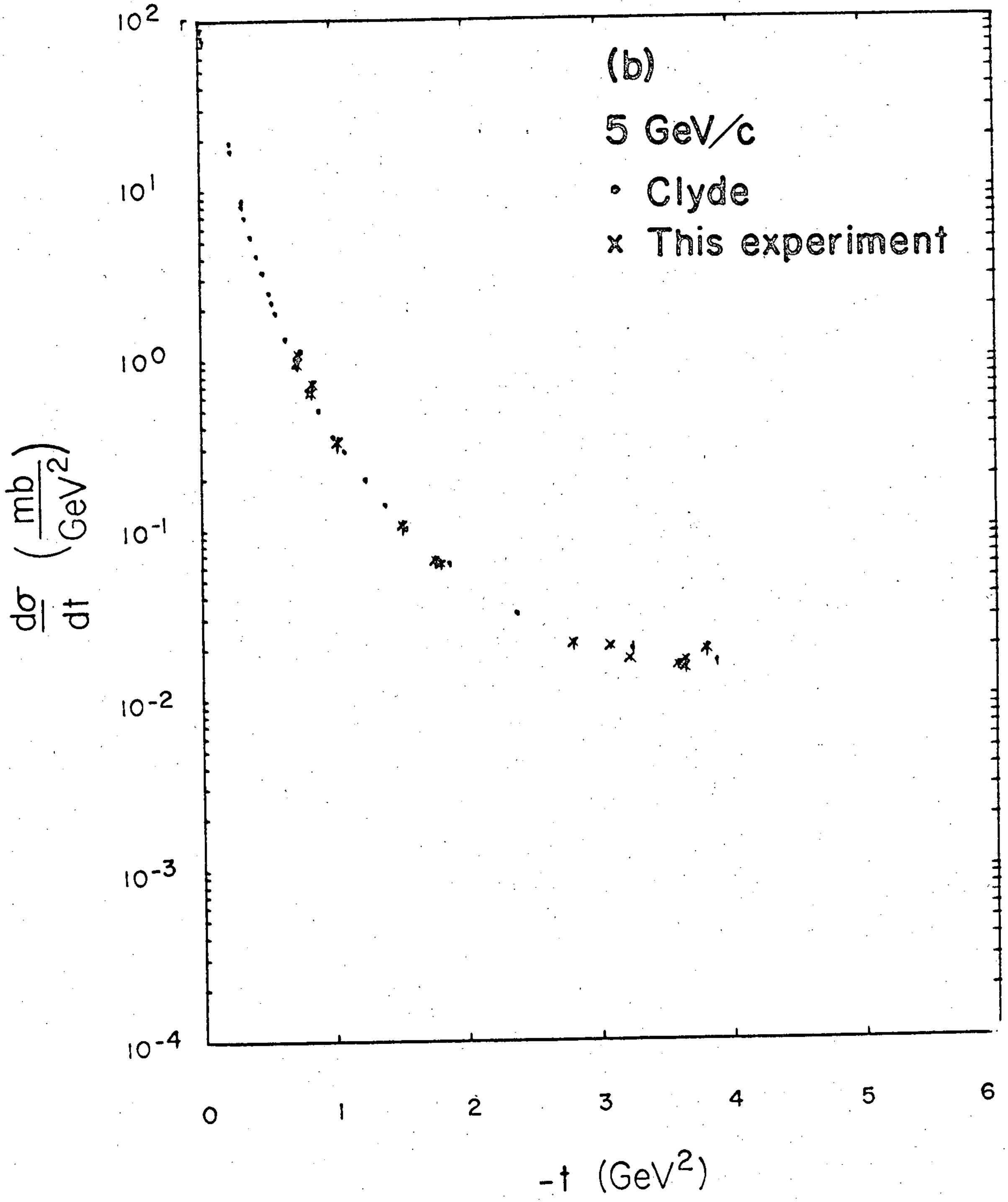

XBL 671-495

Fig. 15(b)

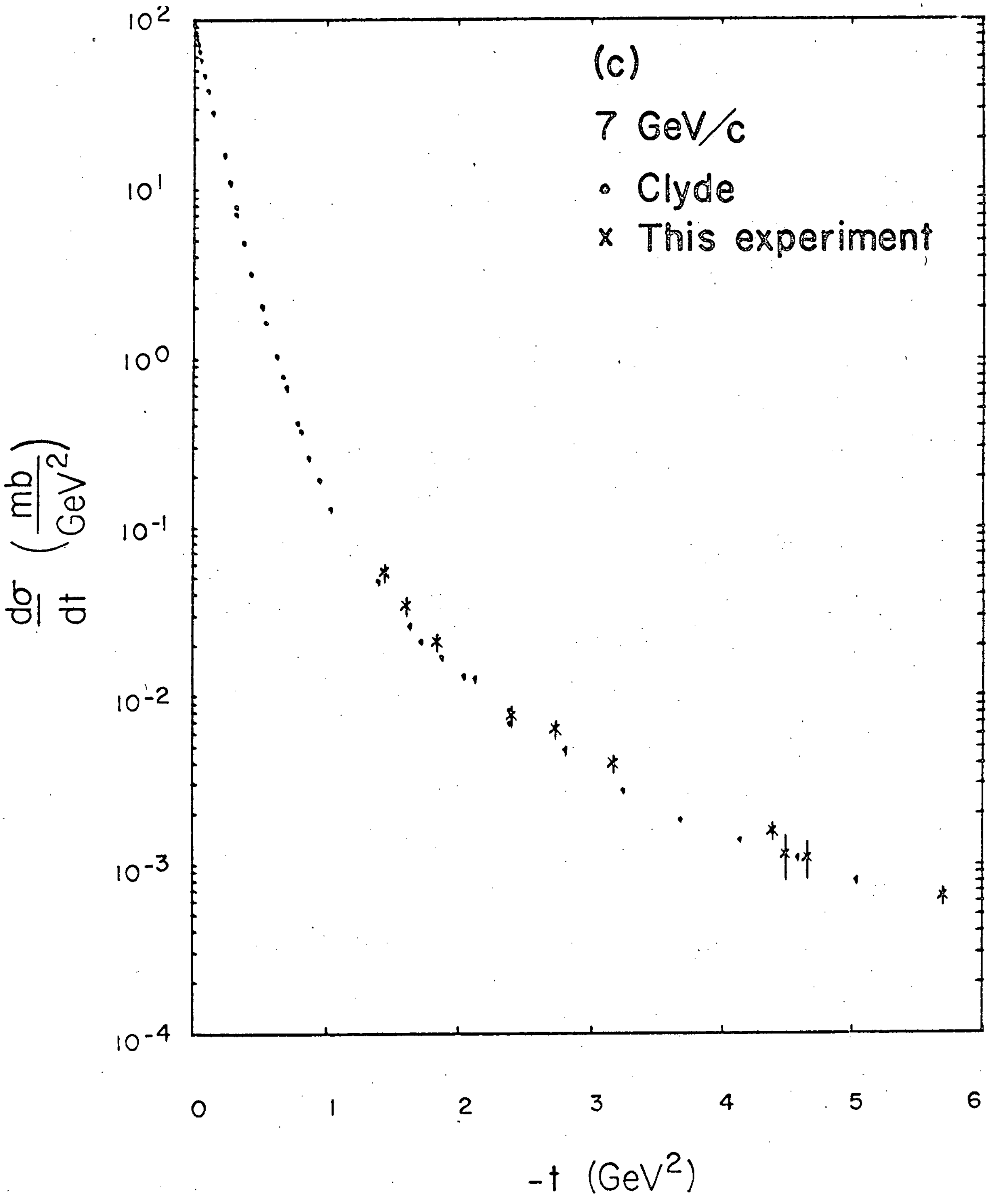

XBL 671-496

Fig. 15(c)

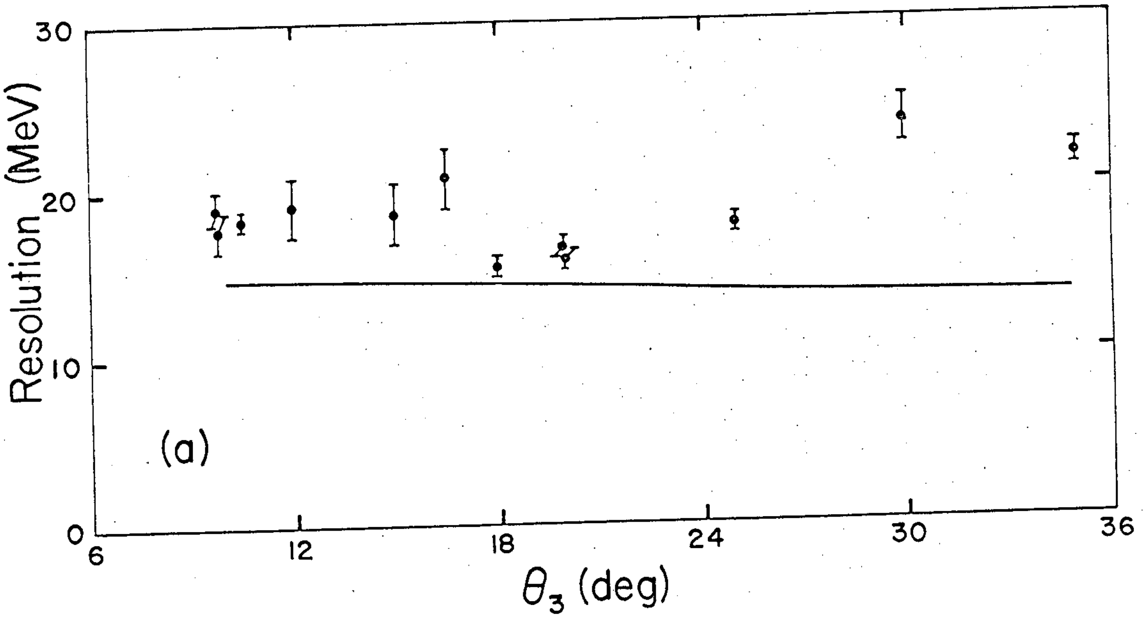

XBL 671-480

Fig. 16(a)

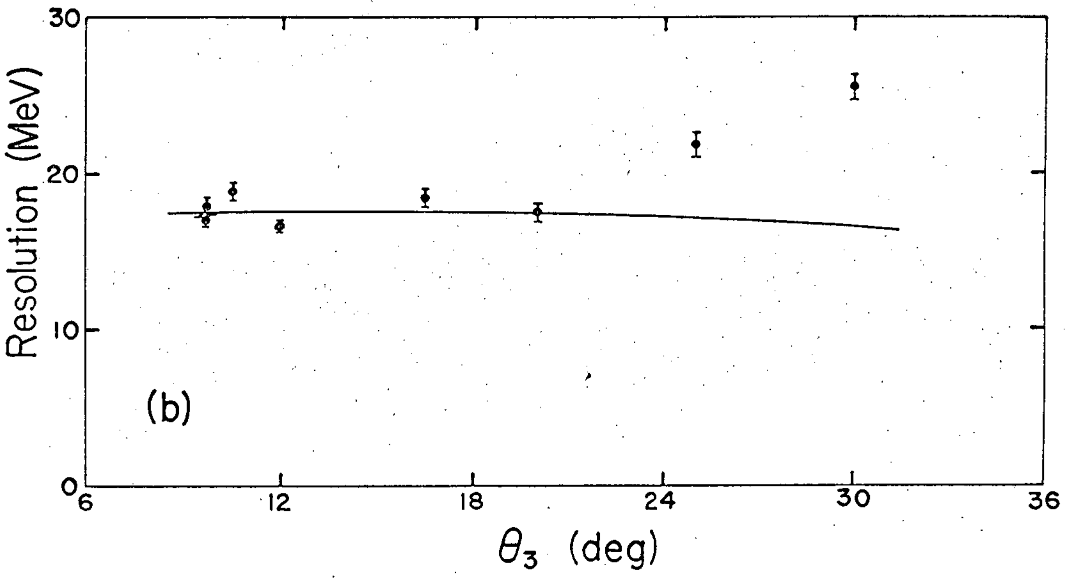

XBL 671-479

Fig. 16(b)

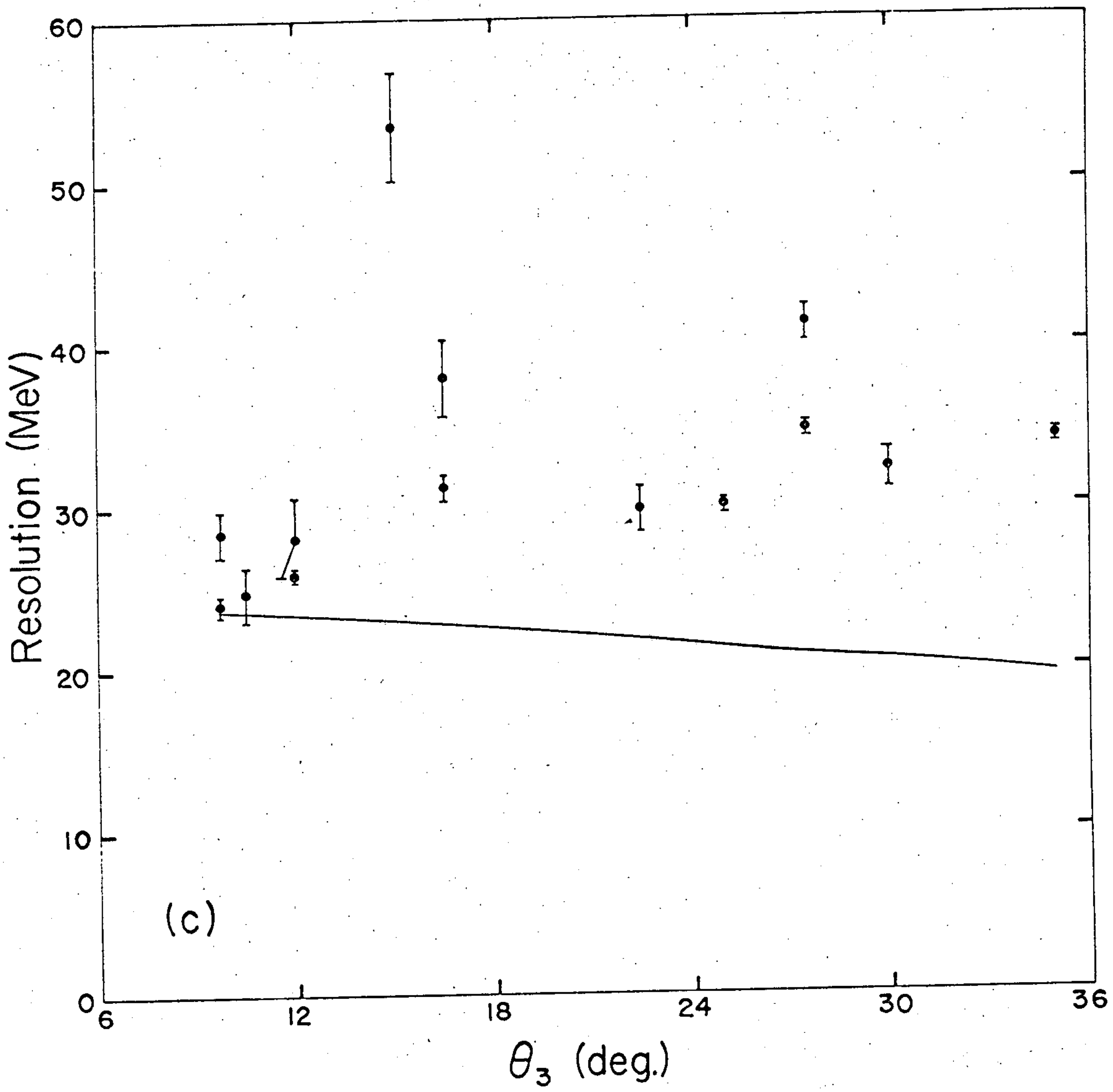

XBL 671-477

Fig. 16(c)

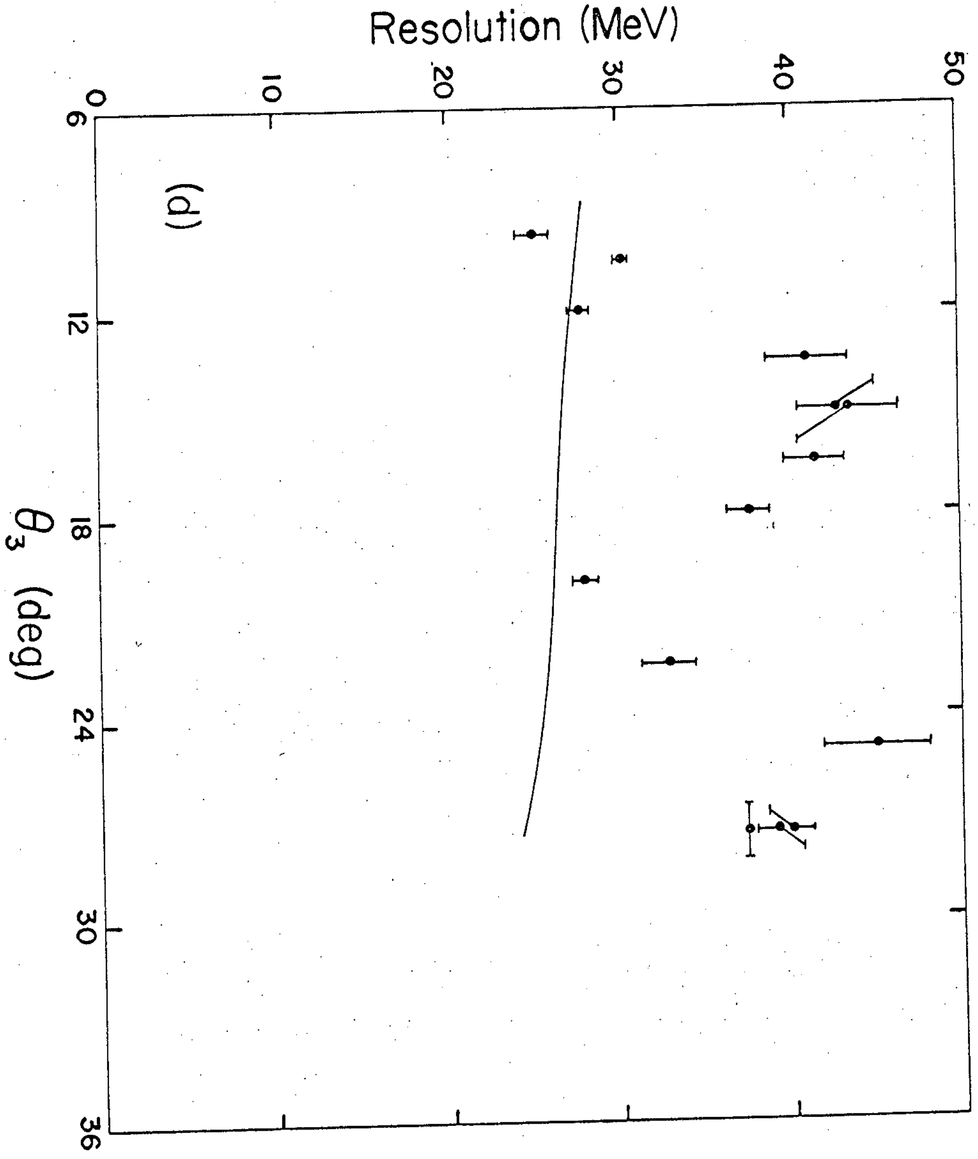

XBL 671-476

Fig. 16(d)

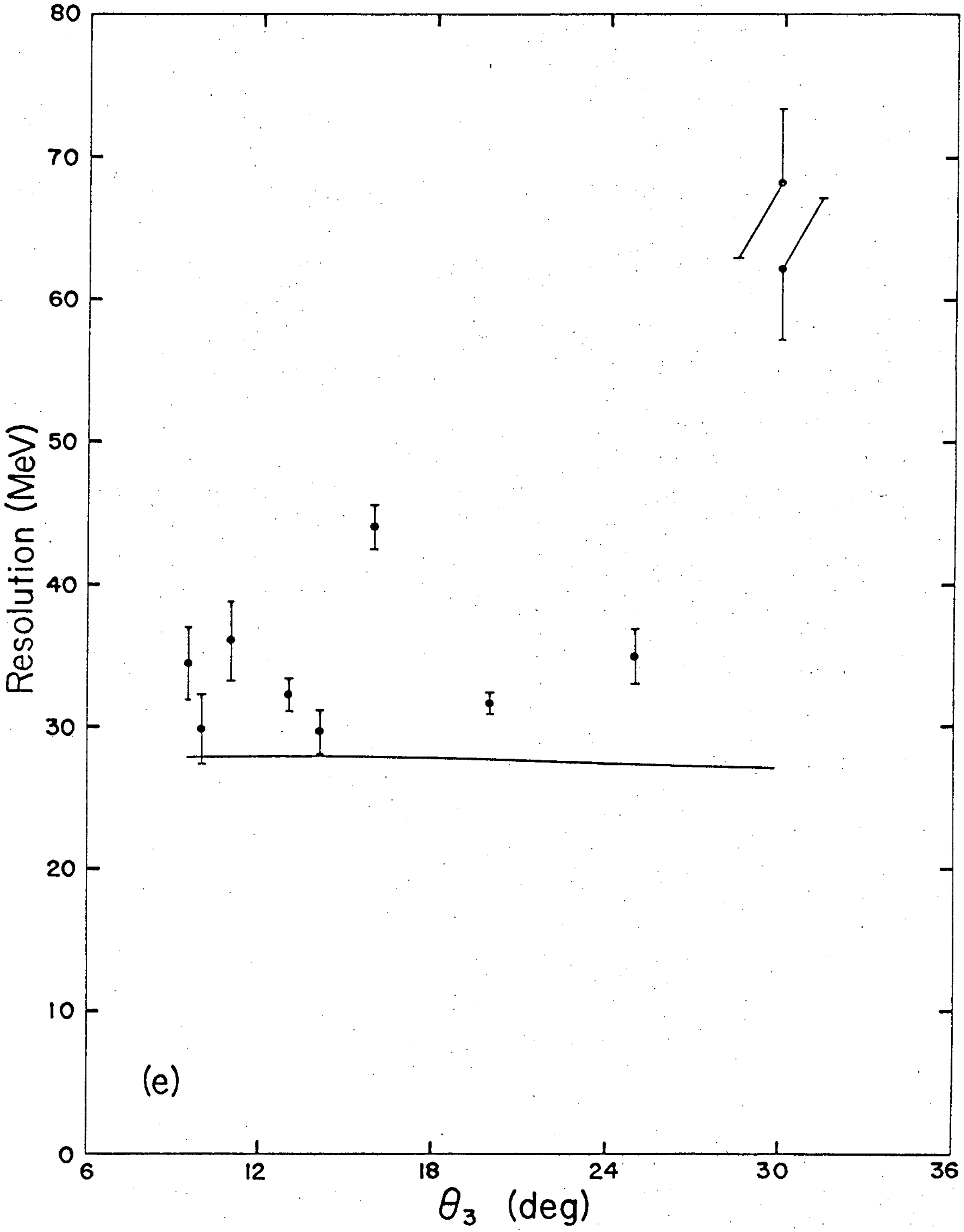

XBL 671-478

Fig. 16(e)

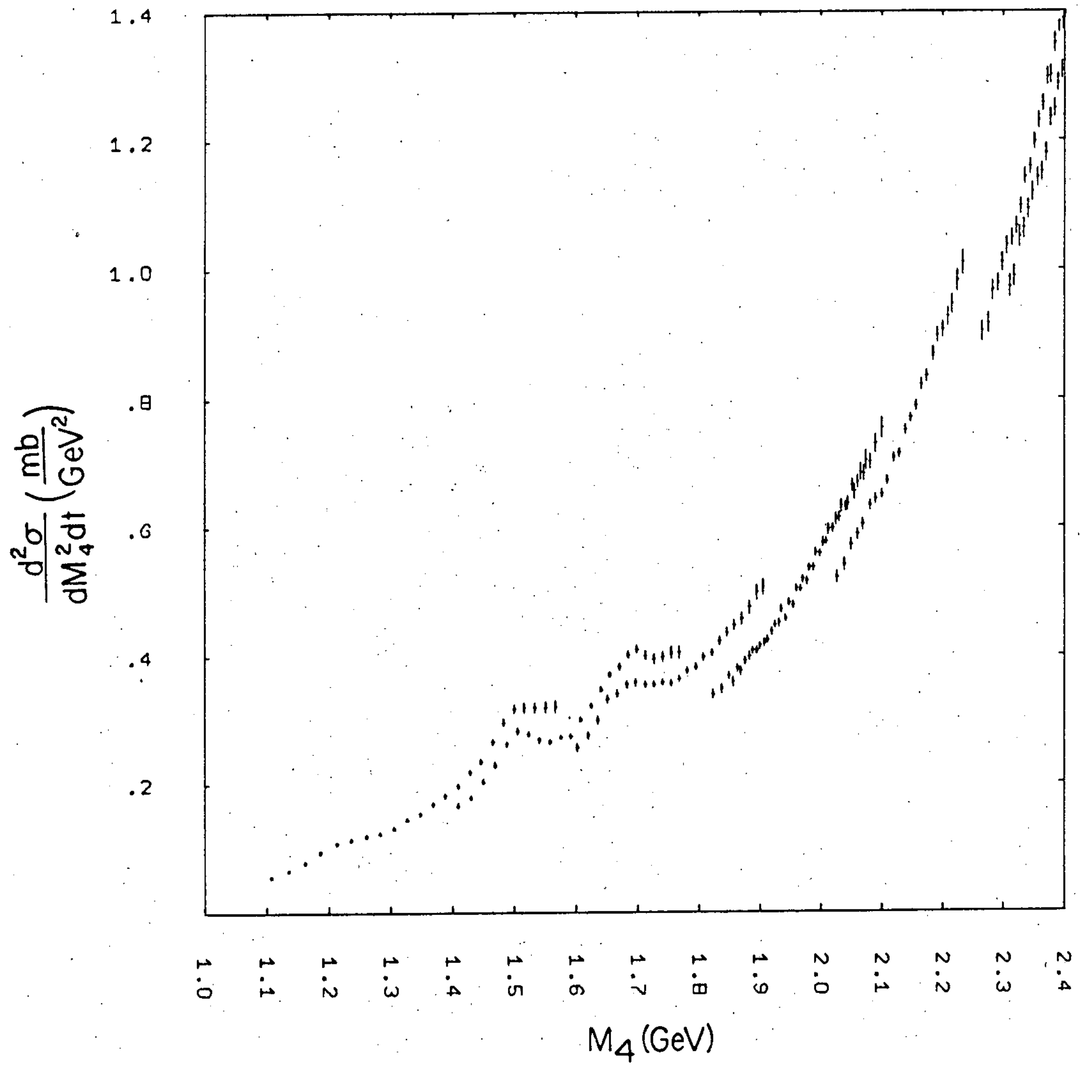

XBL 671-492

Fig. 17(a)

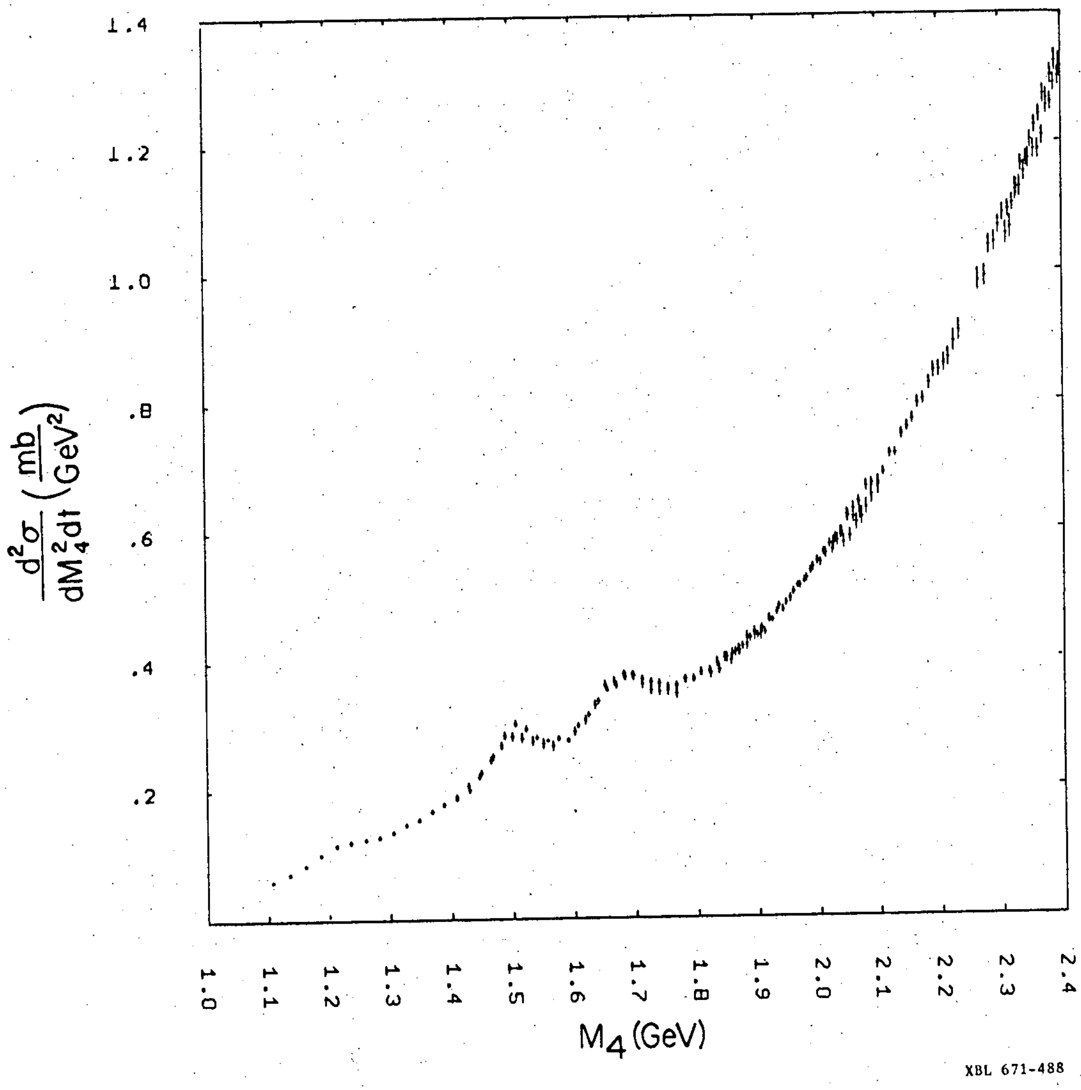

$\frac{d^2\sigma}{dM_4^2dt}\left(\frac{mb}{GeV^2}\right)$
1.4
1.2
1.0
.8
.6
.4
.2
1.0
1.1
1.2
1.3
1.4
1.5
1.6
1.7
1.8
1.9
2.0
2.1
2.2
2.3
2.4
M_4 (GeV)
XBL 671-488

Fig. 17(b).

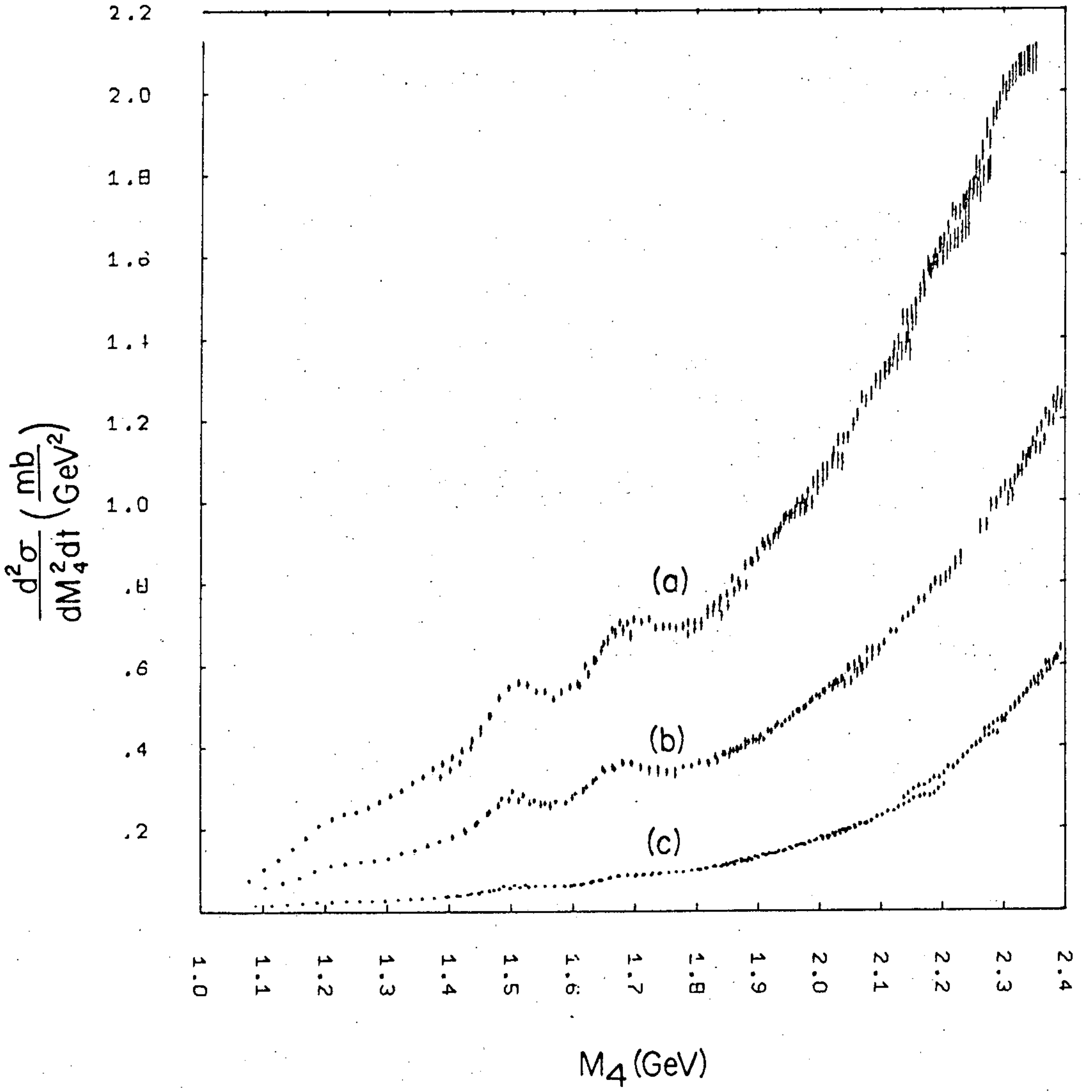

XBL 671-486

Fig. 18

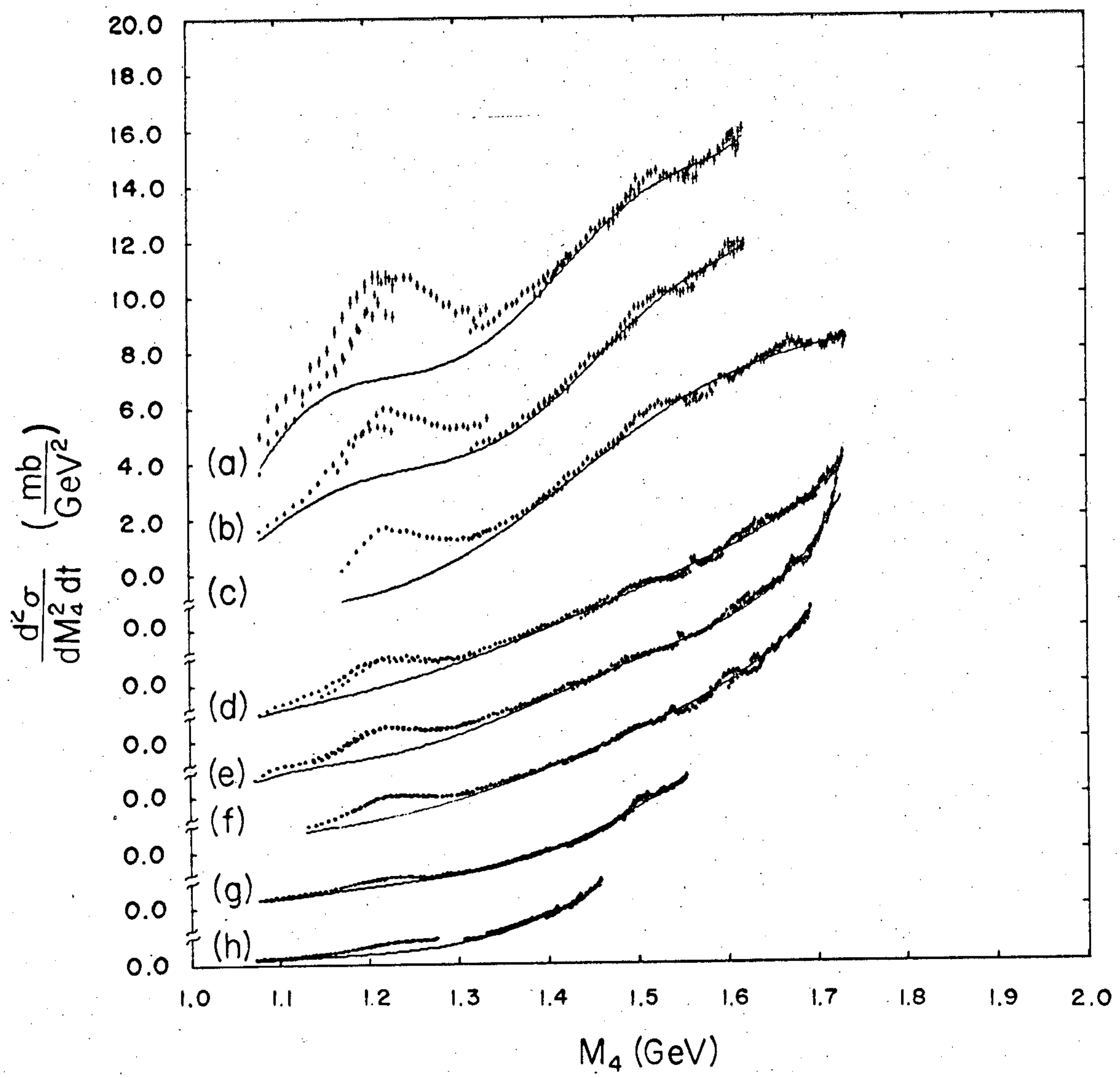

XBL 671-487

Fig. 19

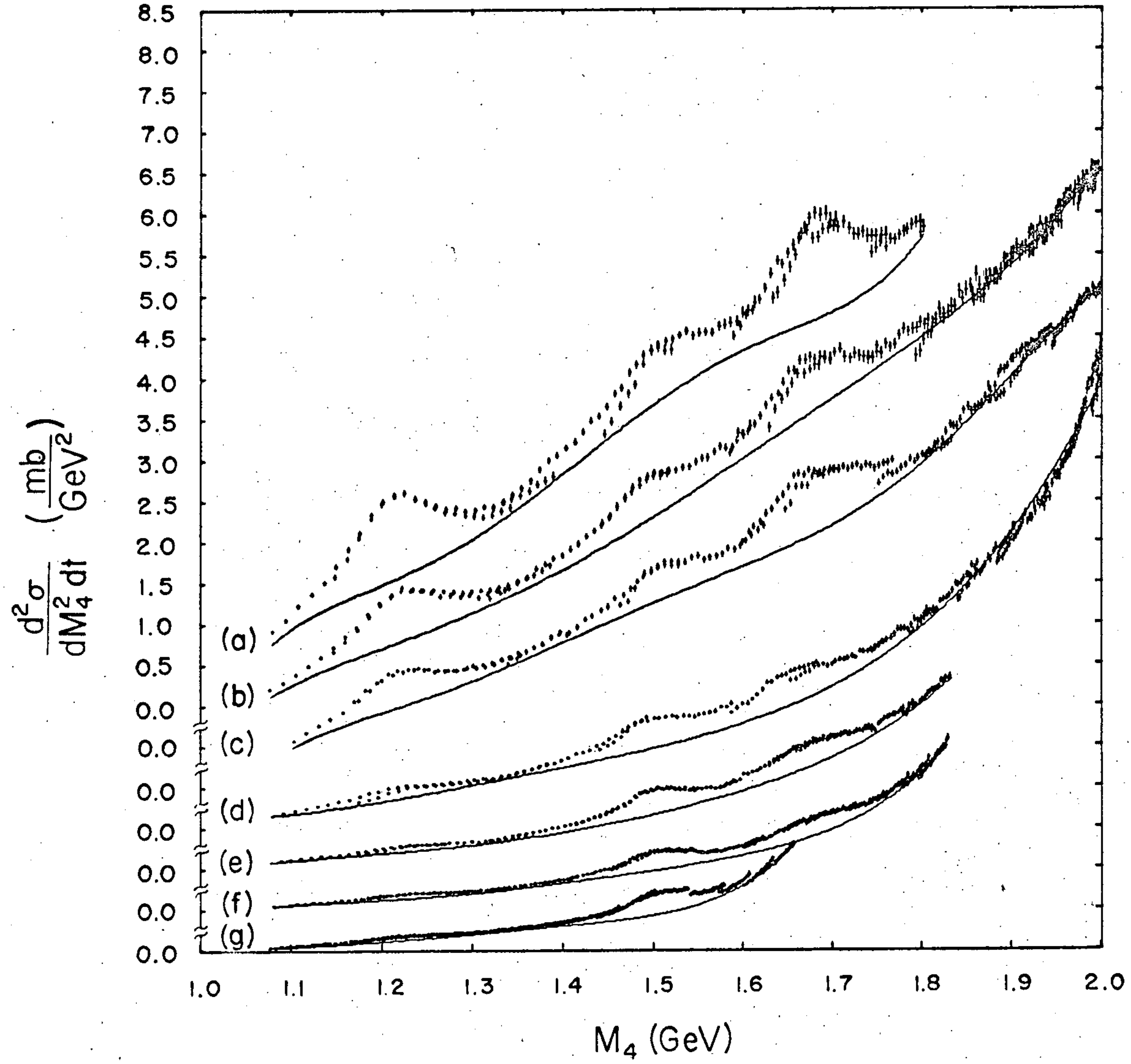

XBL 671-489

Fig. 20

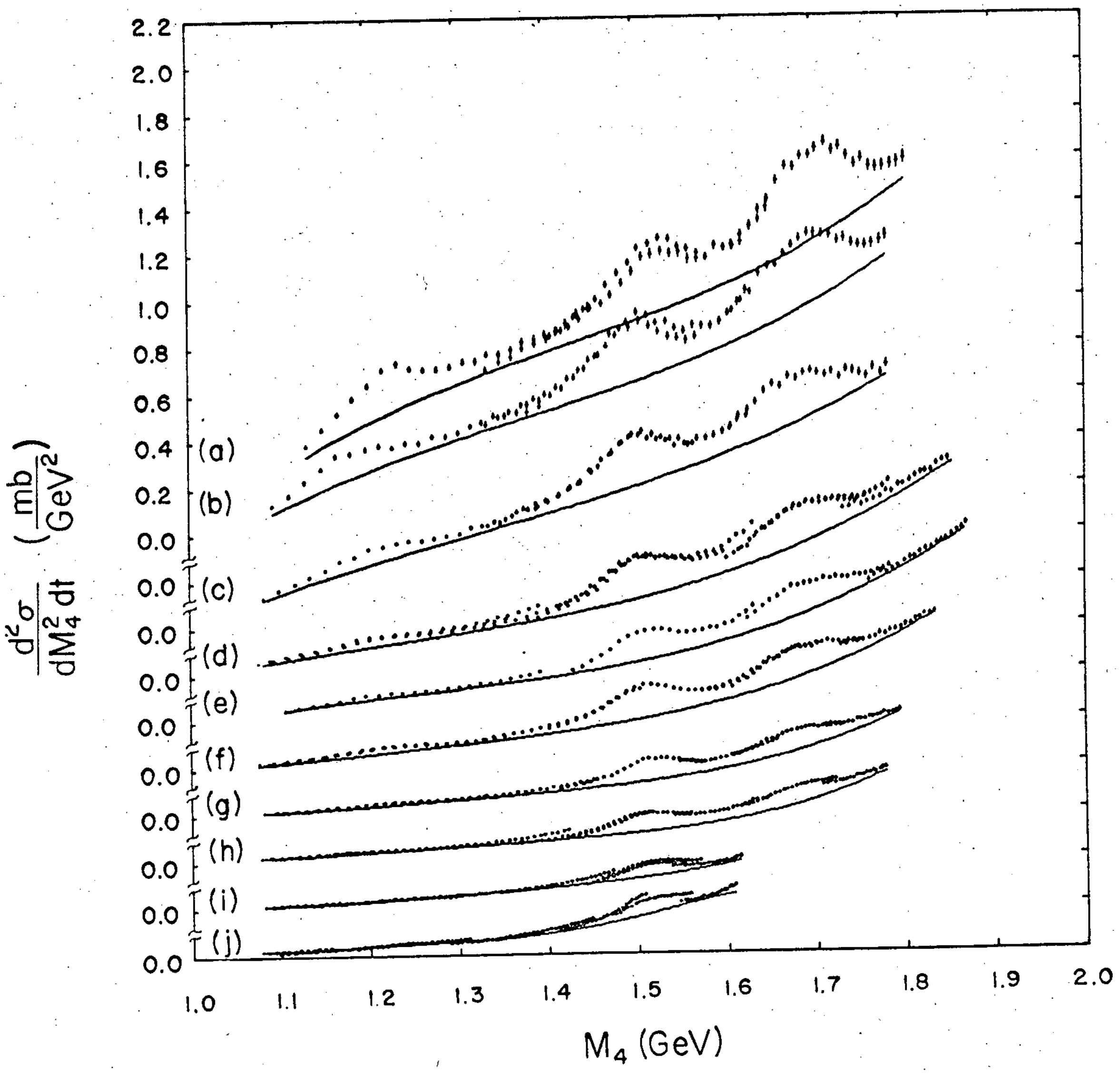

XBL 671-493

Fig. 21

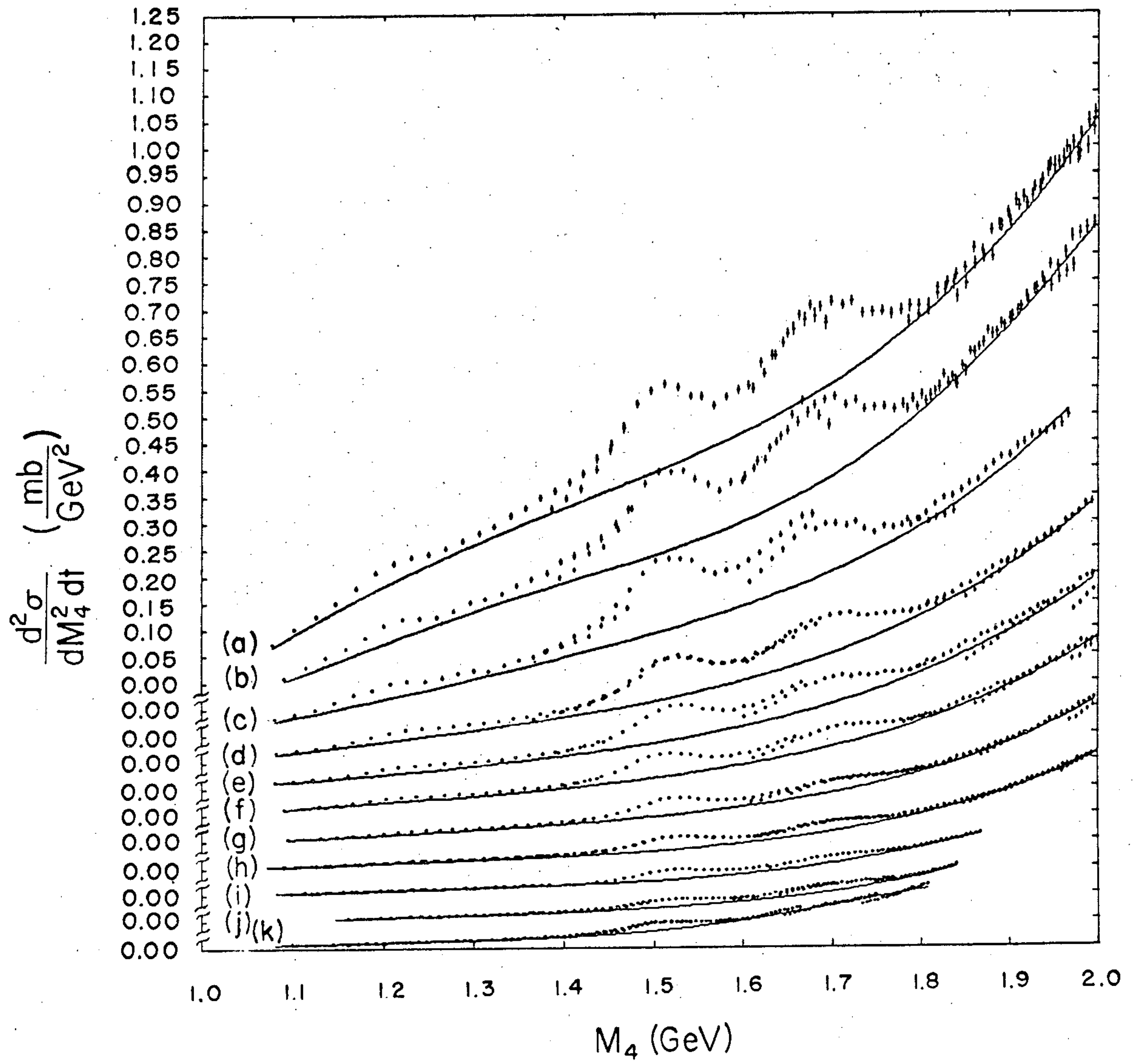

XBL 671-490

Fig. 22

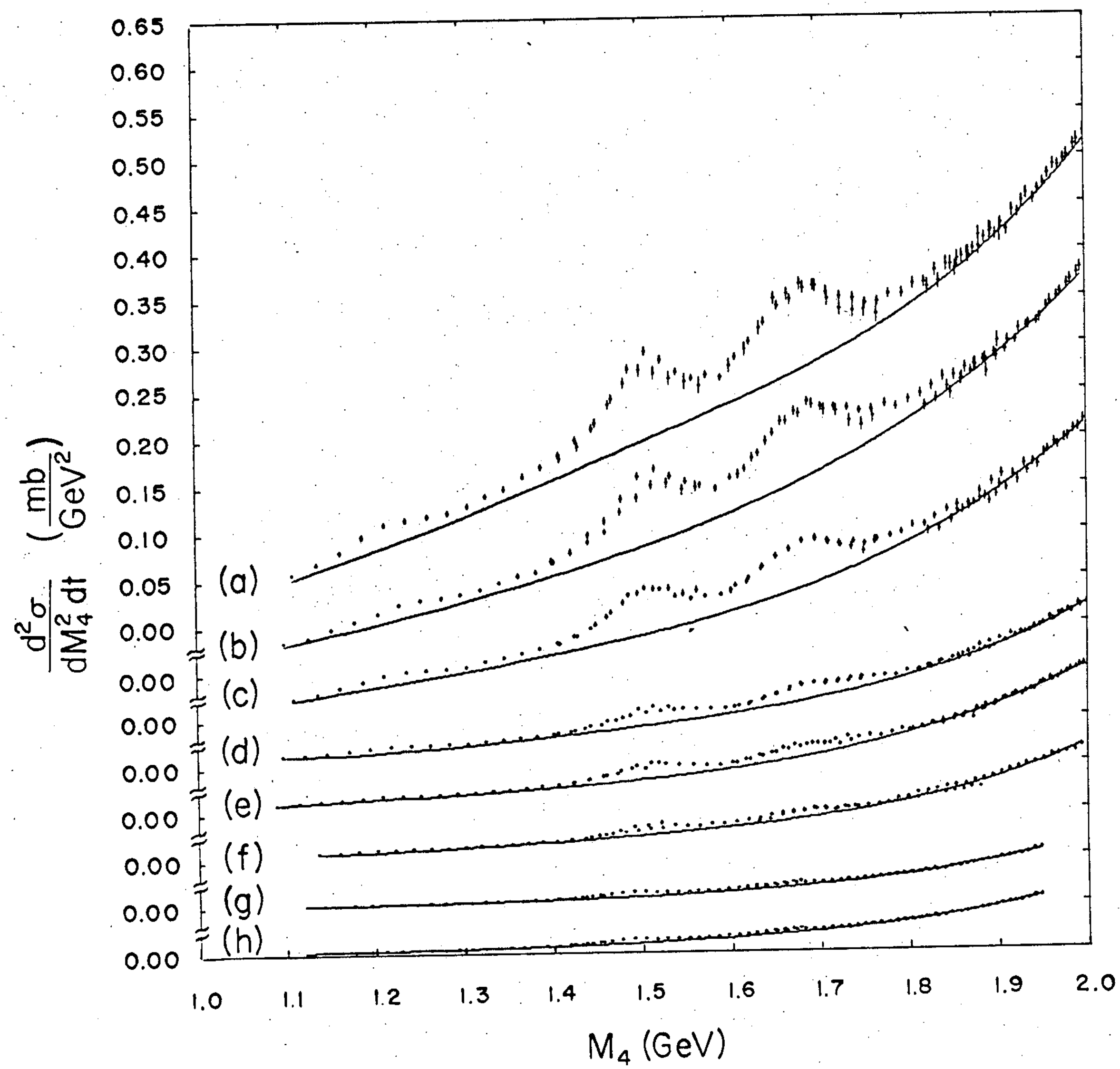

XBL 671-491

Fig. 23

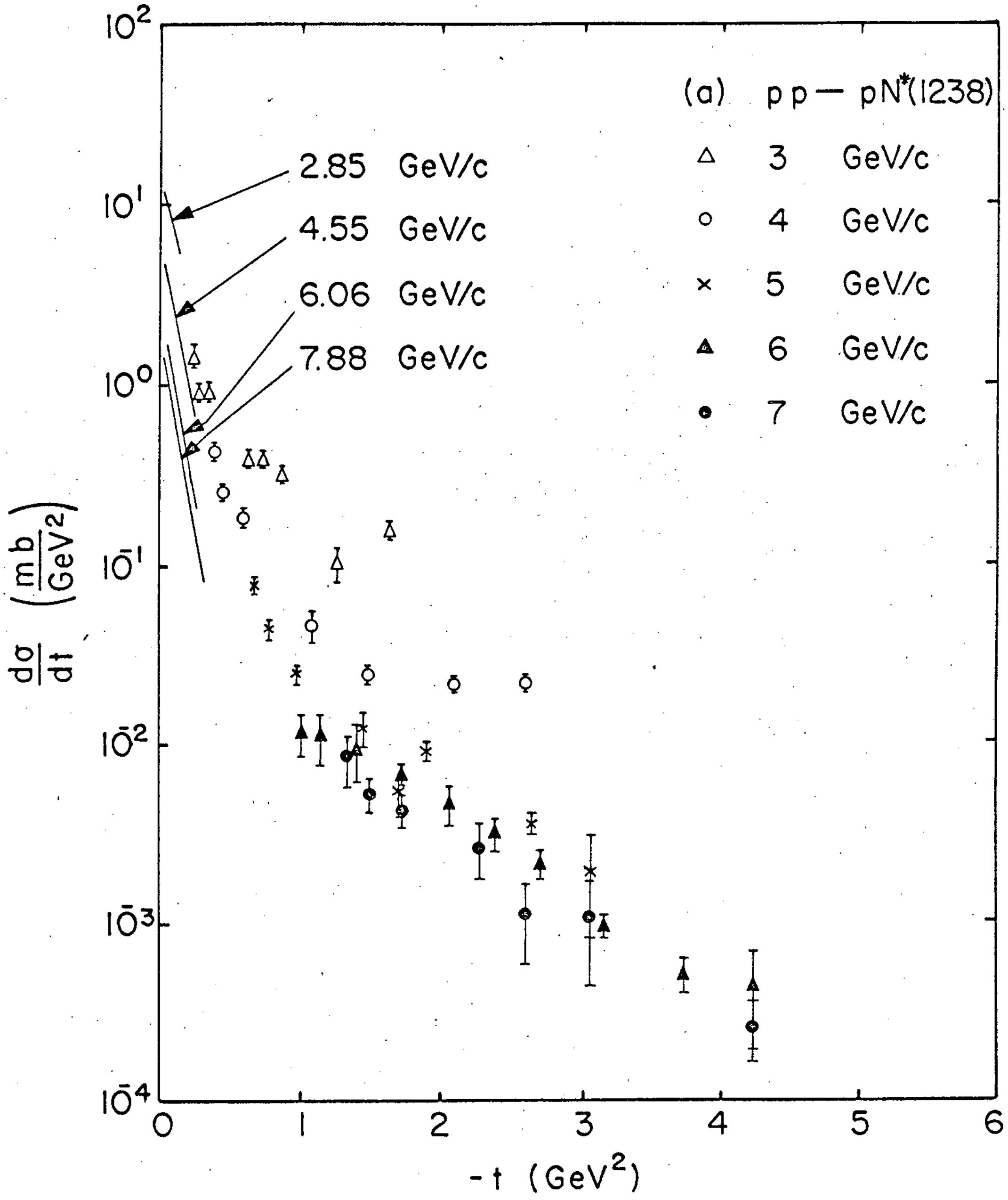

XBL 671-474

Fig. 24(a)

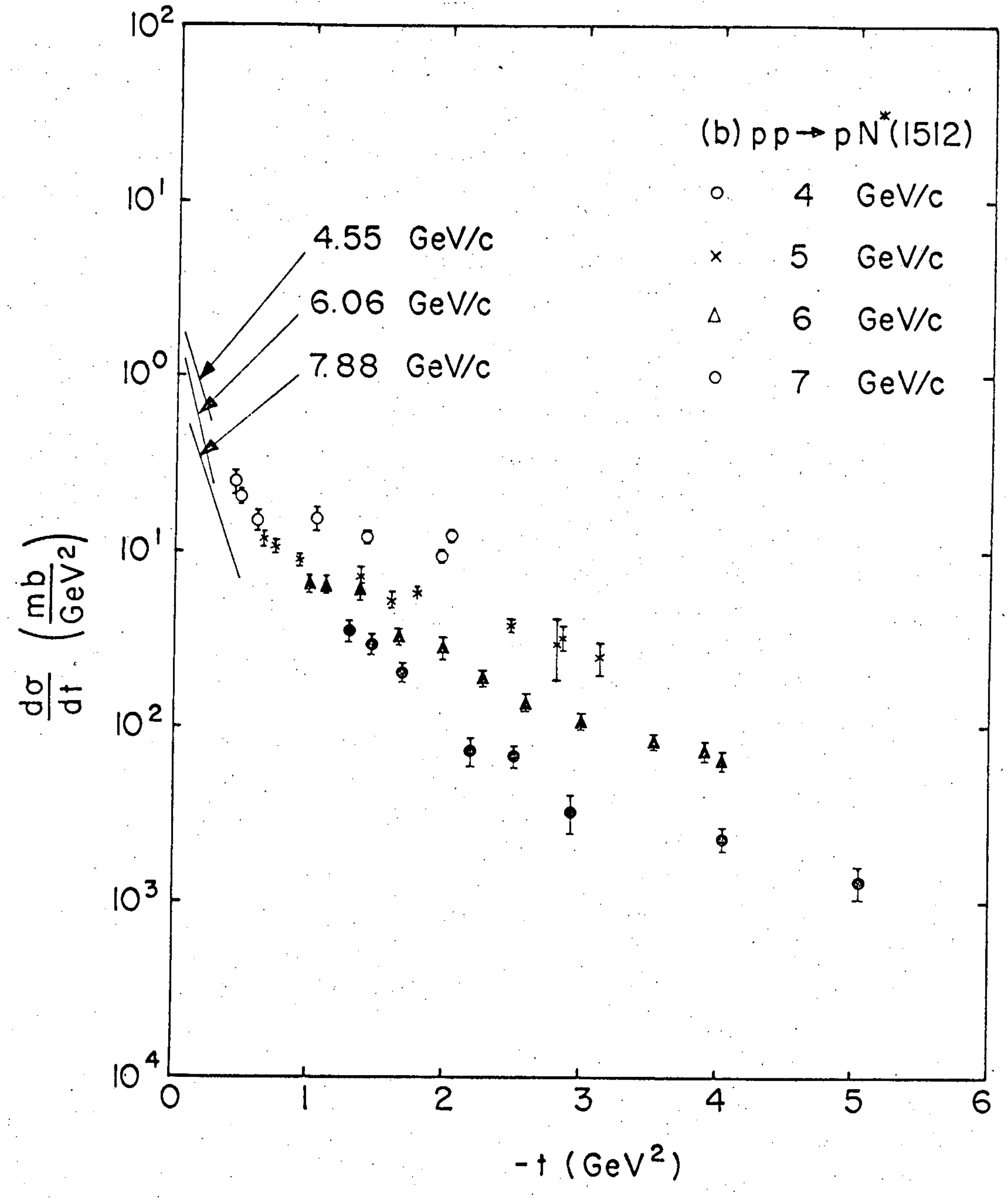

XBL 671-516

Fig. 24(b)

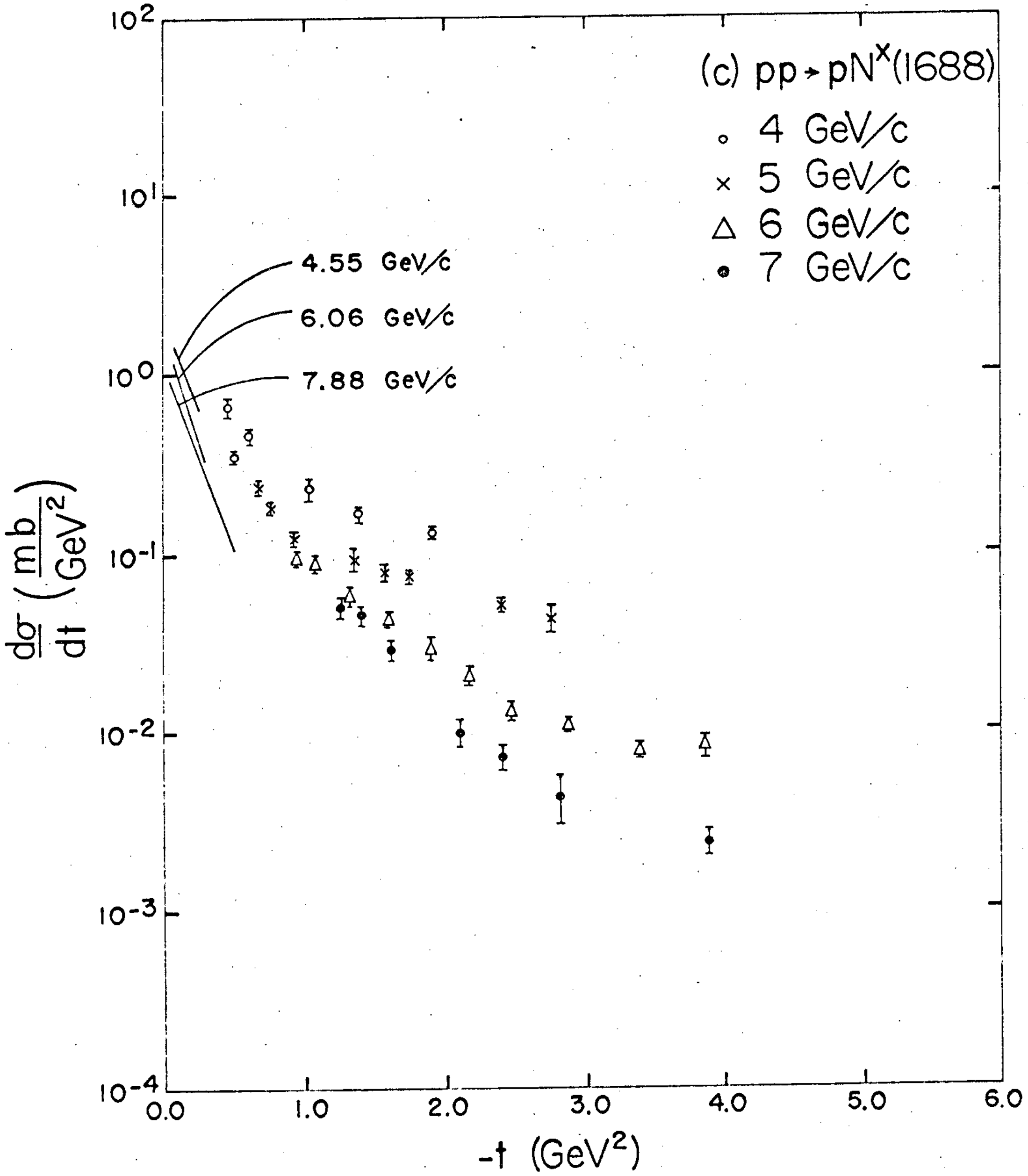

XBL 671-515

Fig. 24(c)

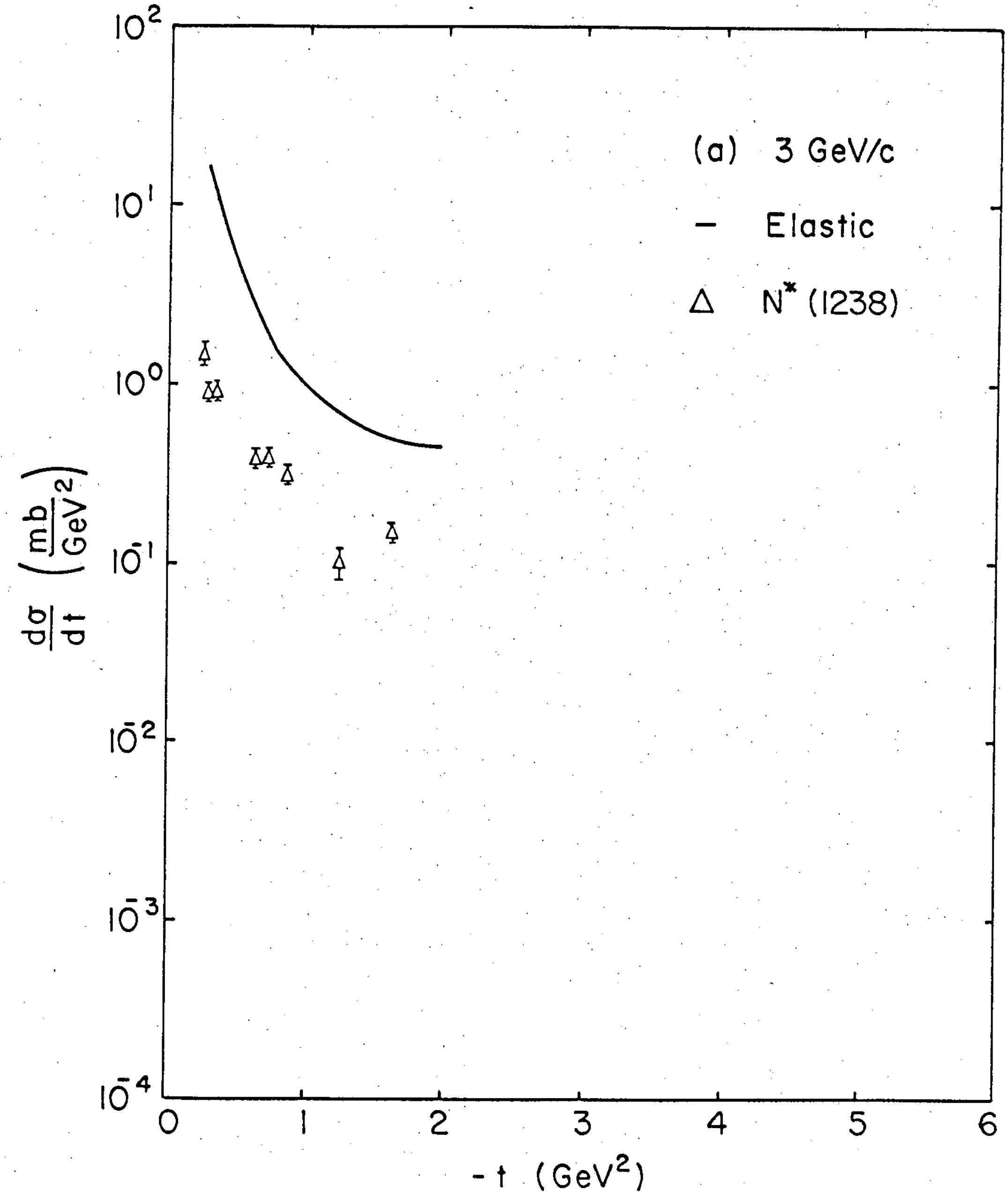

XBL 671-475

Fig. 25(a)

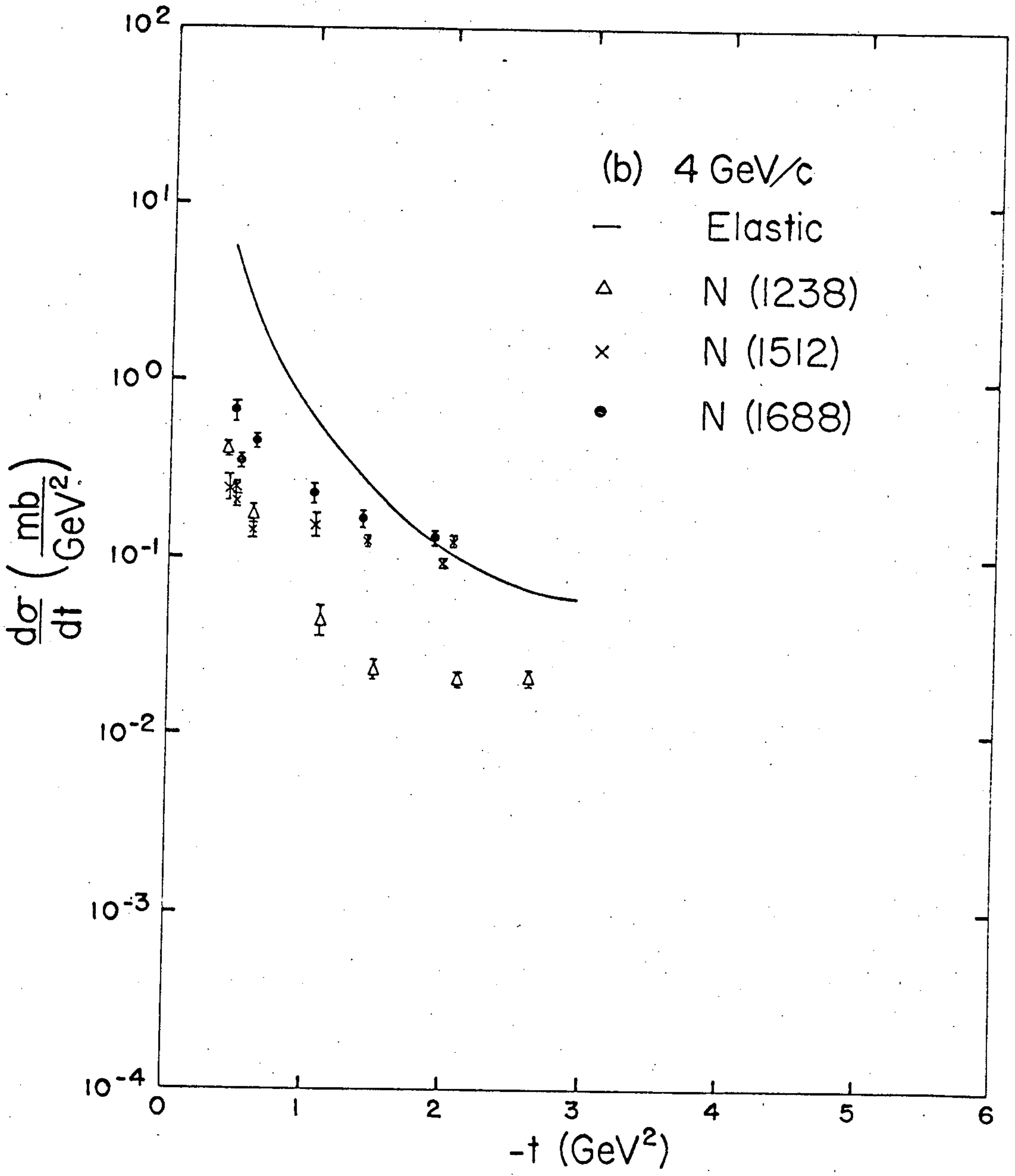

XBL 671-520

Fig.25(b)

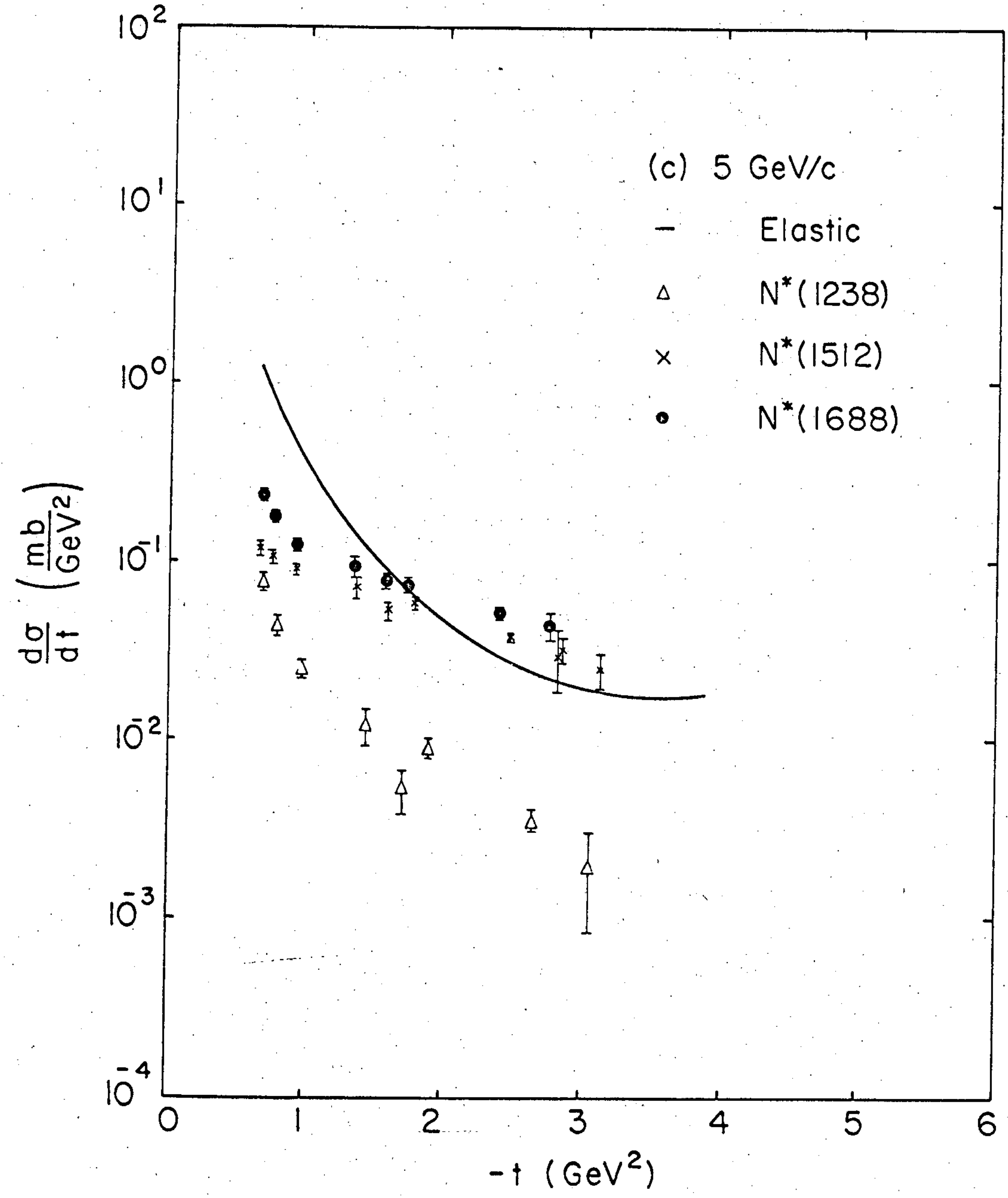

XBL 671-519

Fig. 25(c)

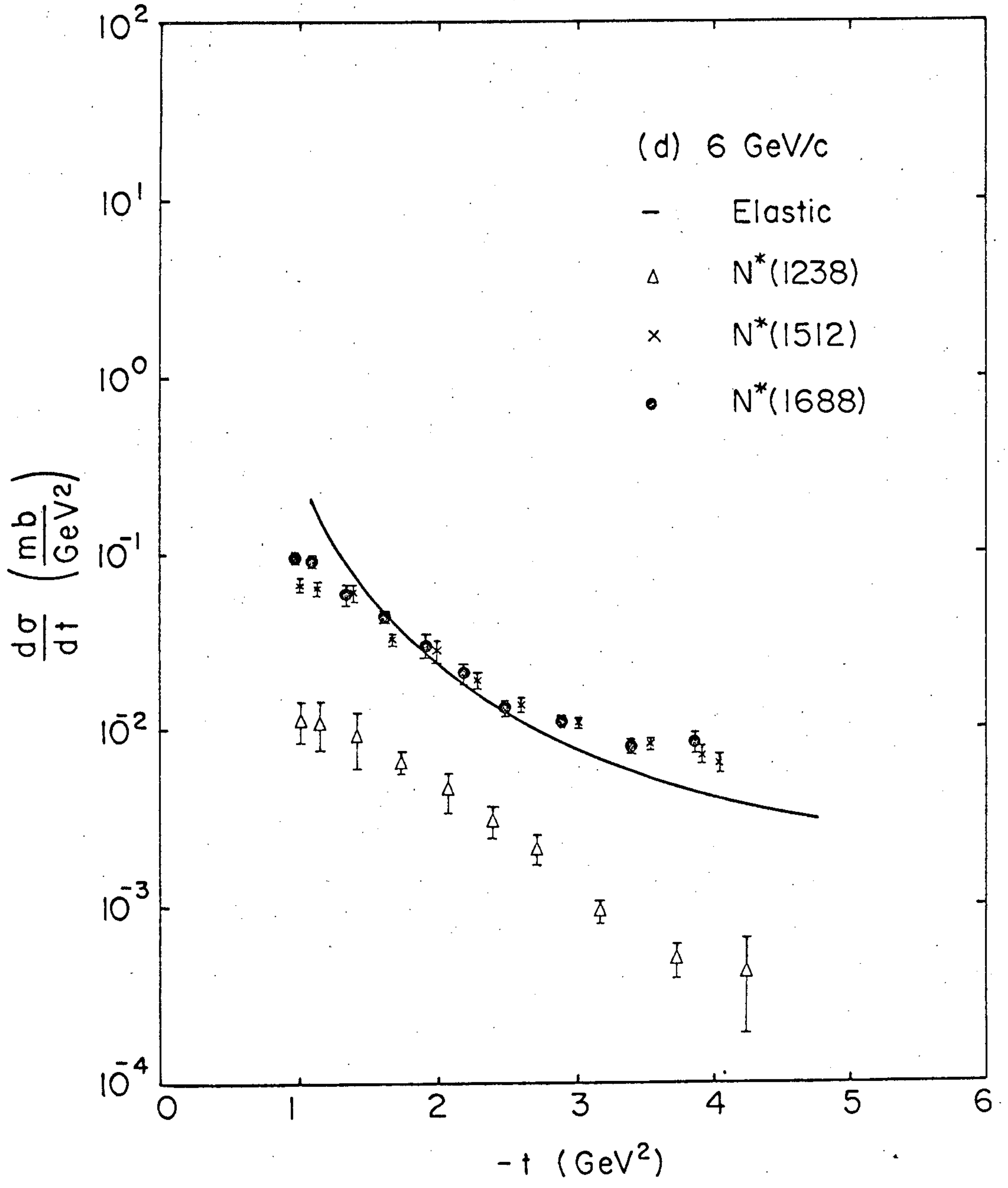

XBL 671-518

Fig. 25(d)

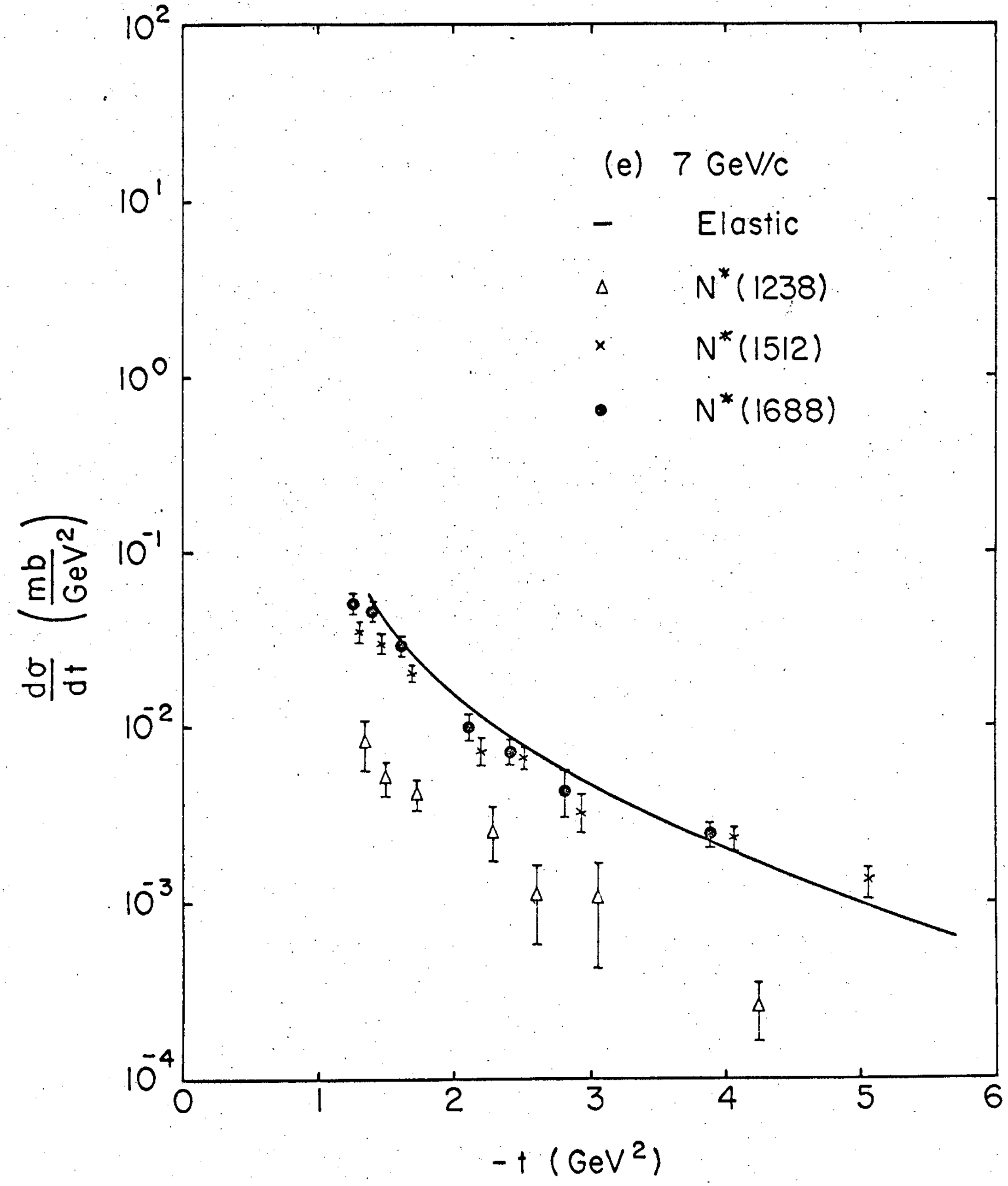

XBL 671-517

Fig. 25(e)

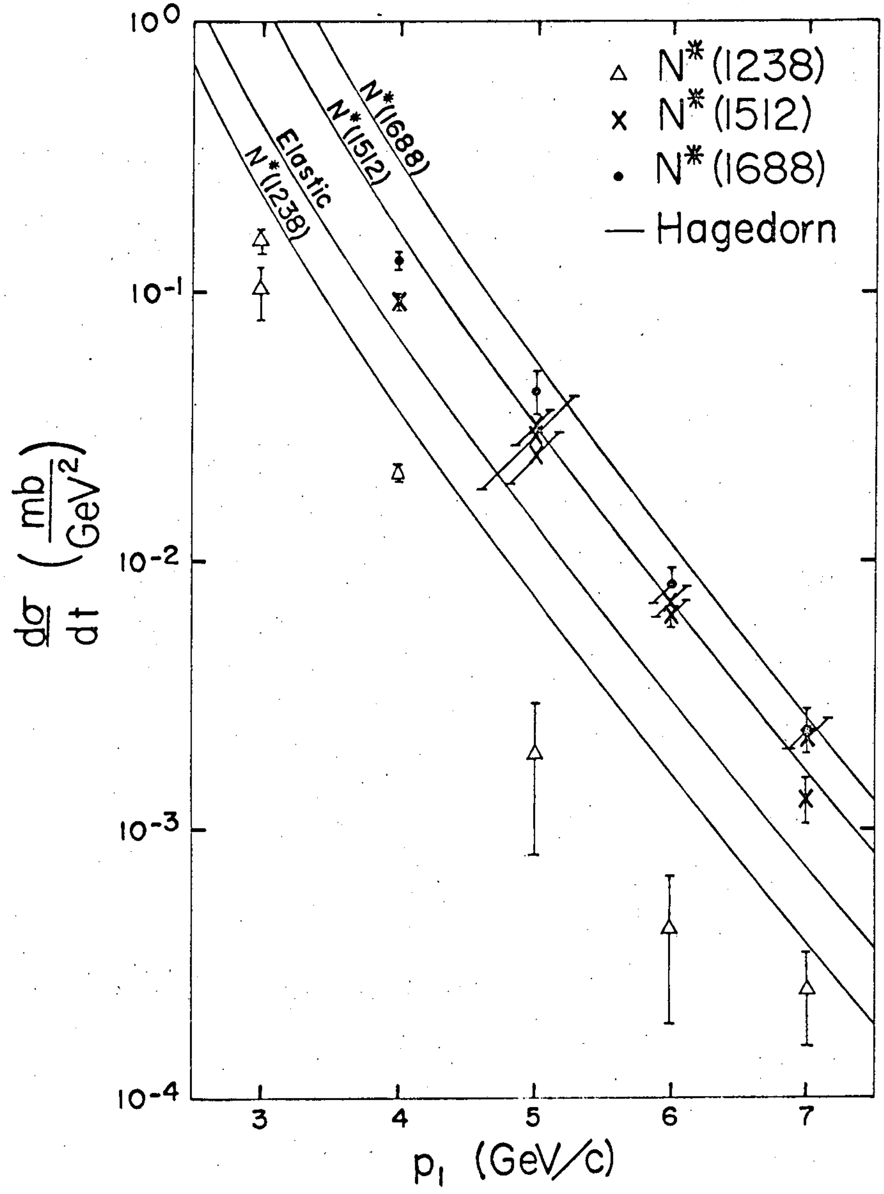

XBL 671-485

Fig. 26

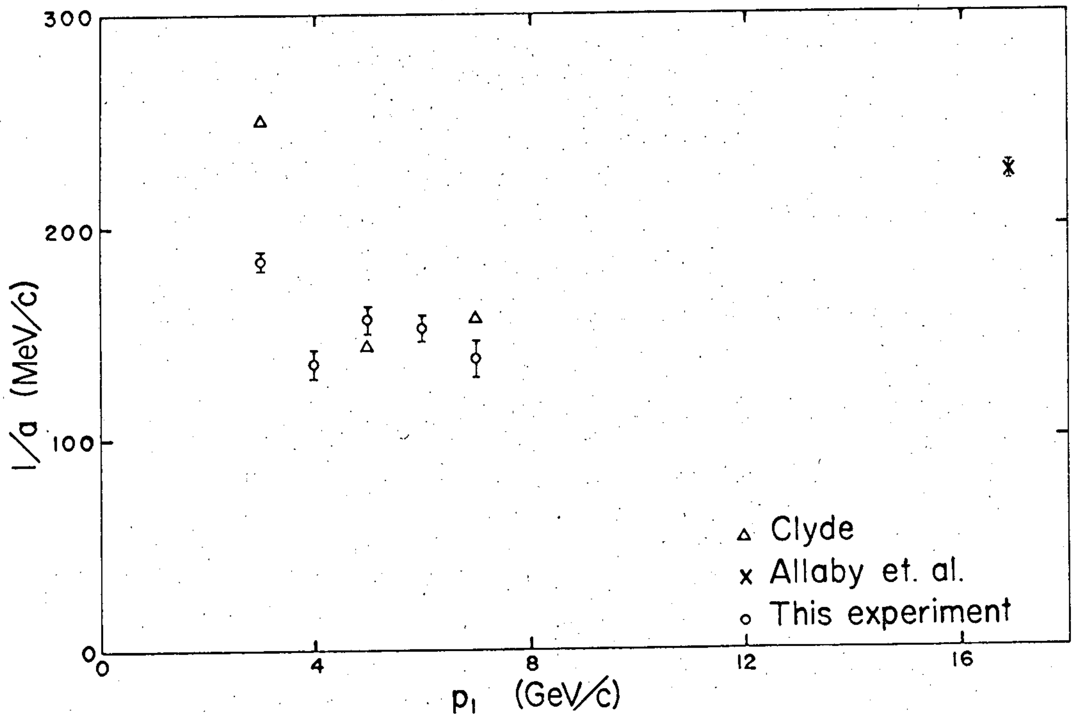

XBL 671-482

Fig. 27

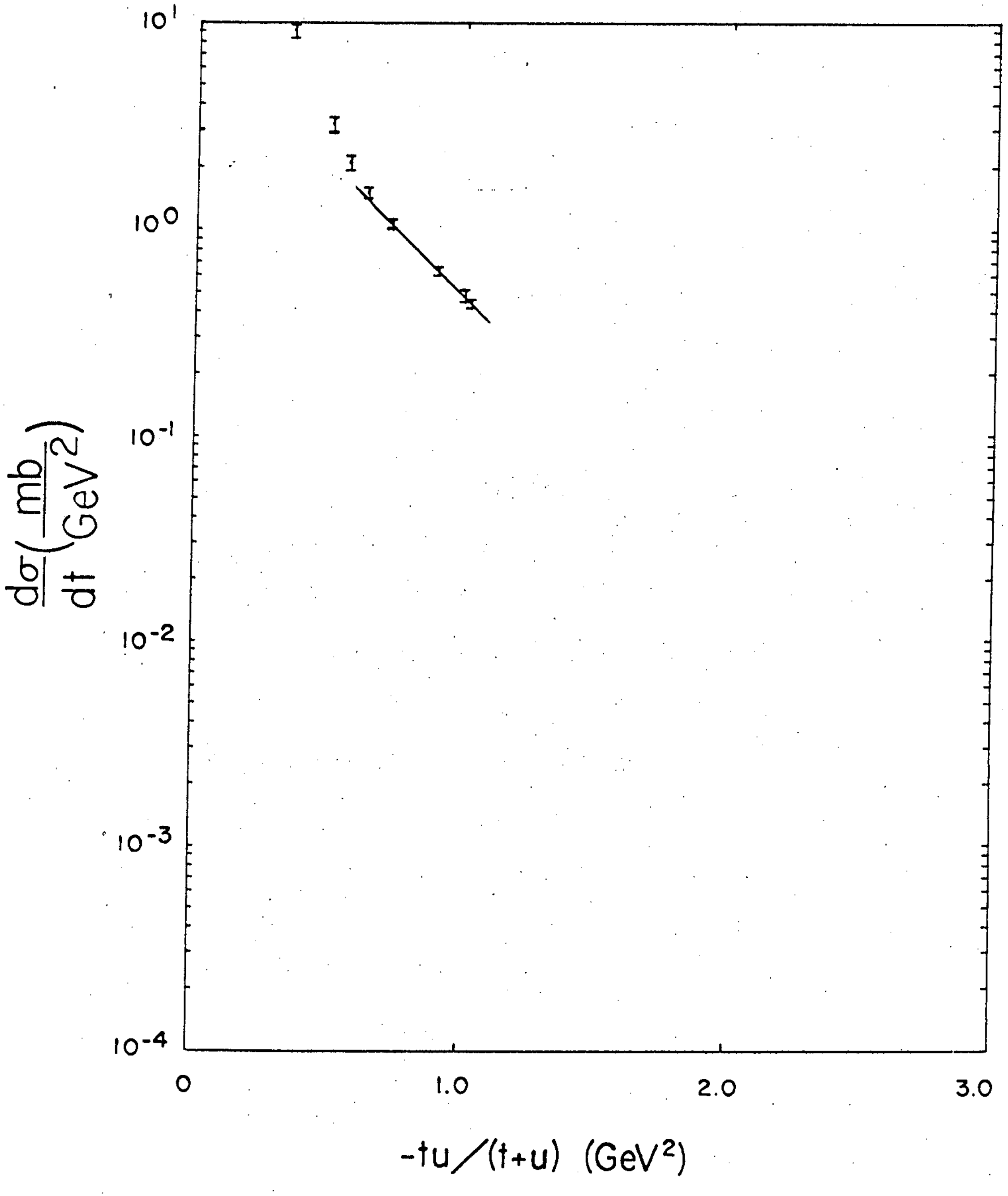

XBL 671-511

Fig. 28(a)

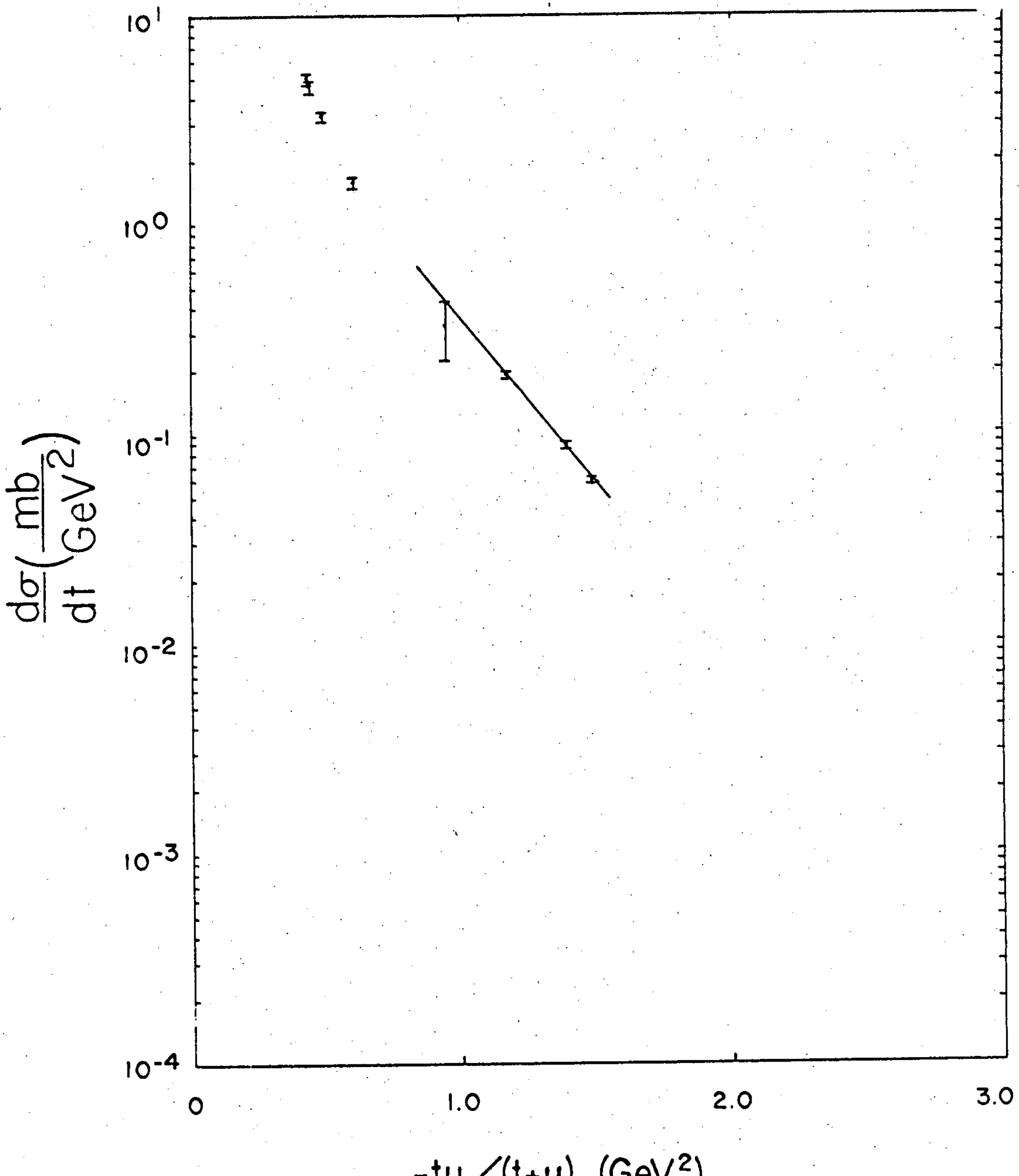

XBL 671-514

Fig. 28(b)

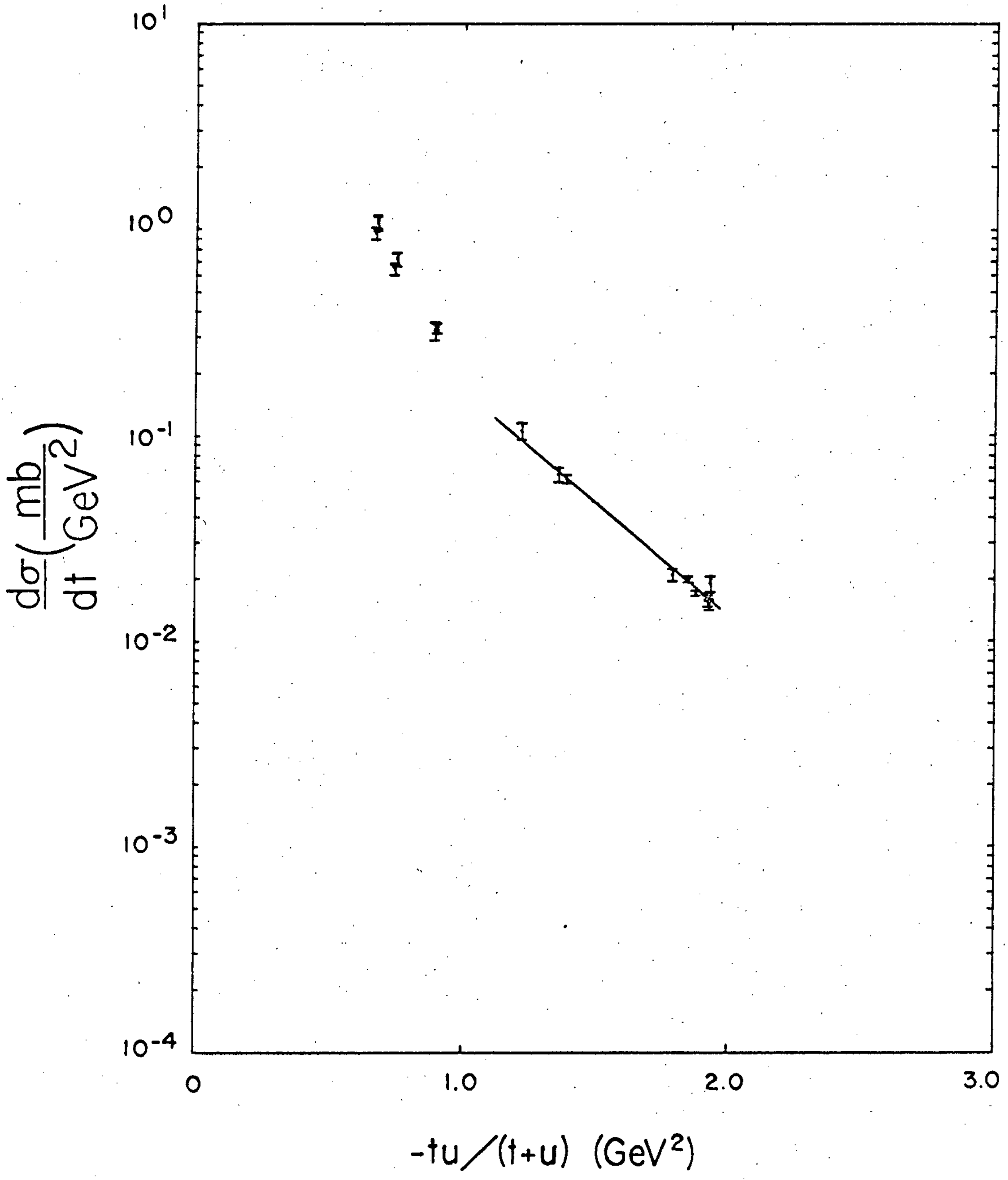

XBL 671-508

Fig. 28(c)

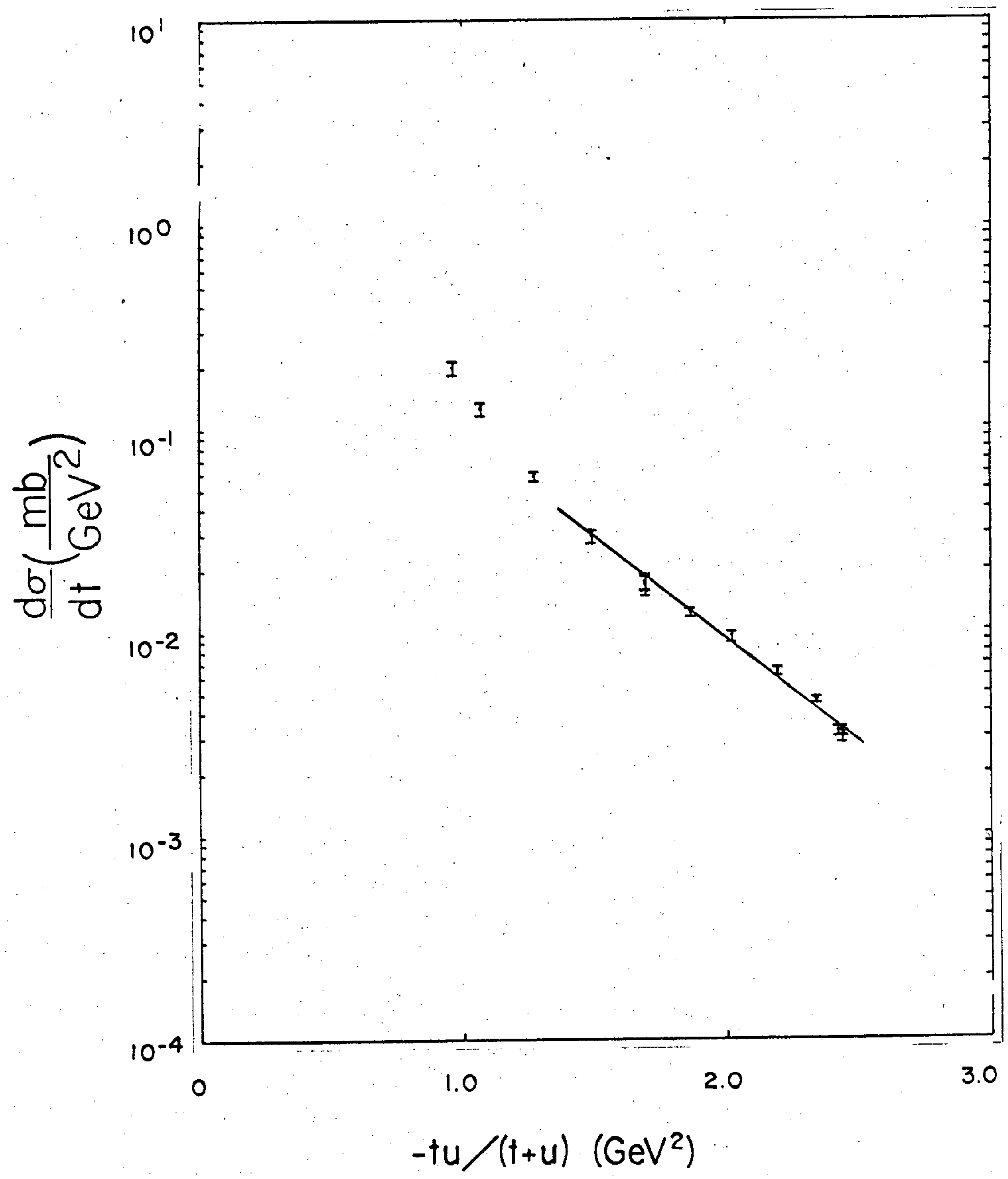

XBL 671-509

Fig. 28(d)

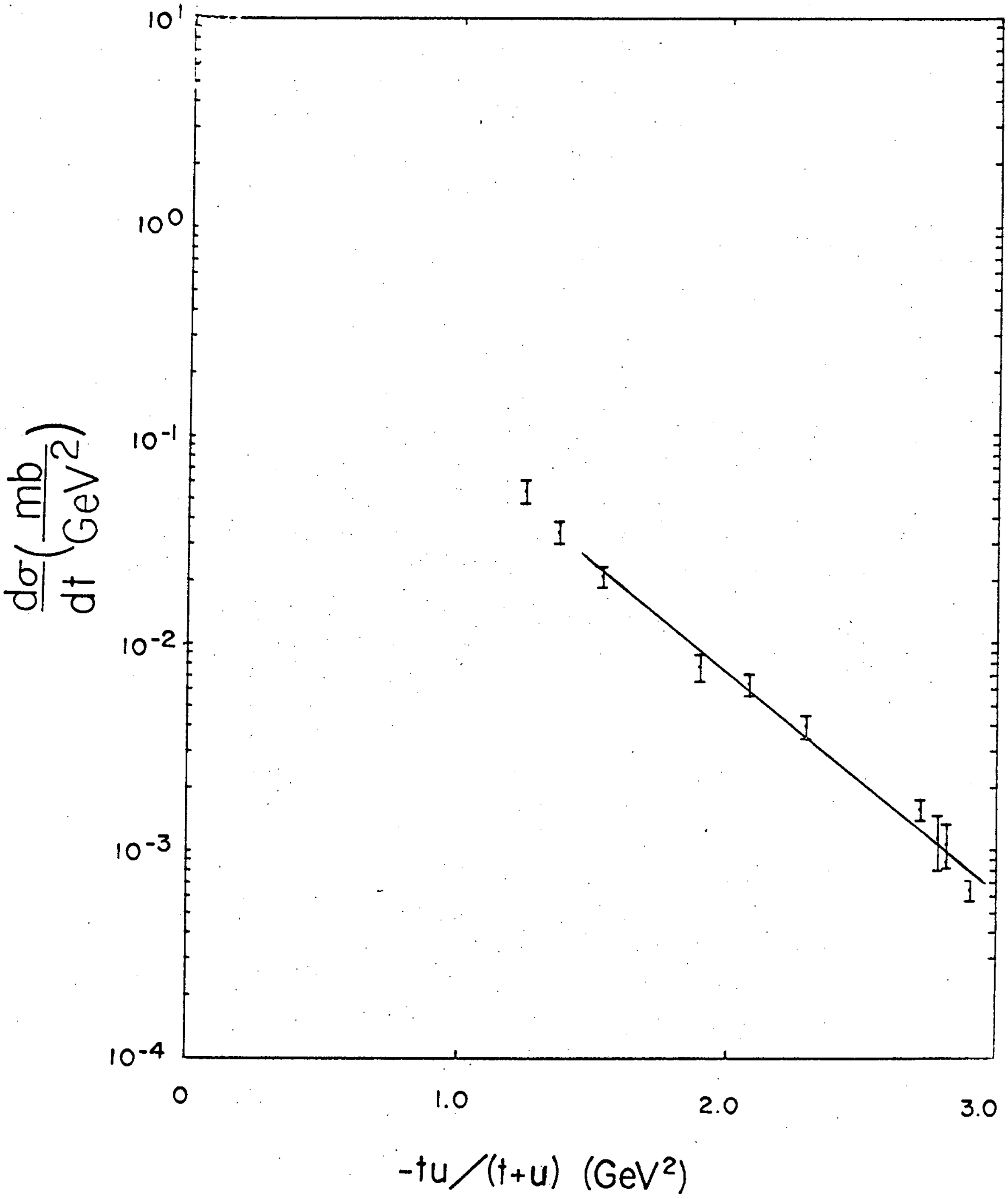

XBL 671-510

Fig. 28(e)

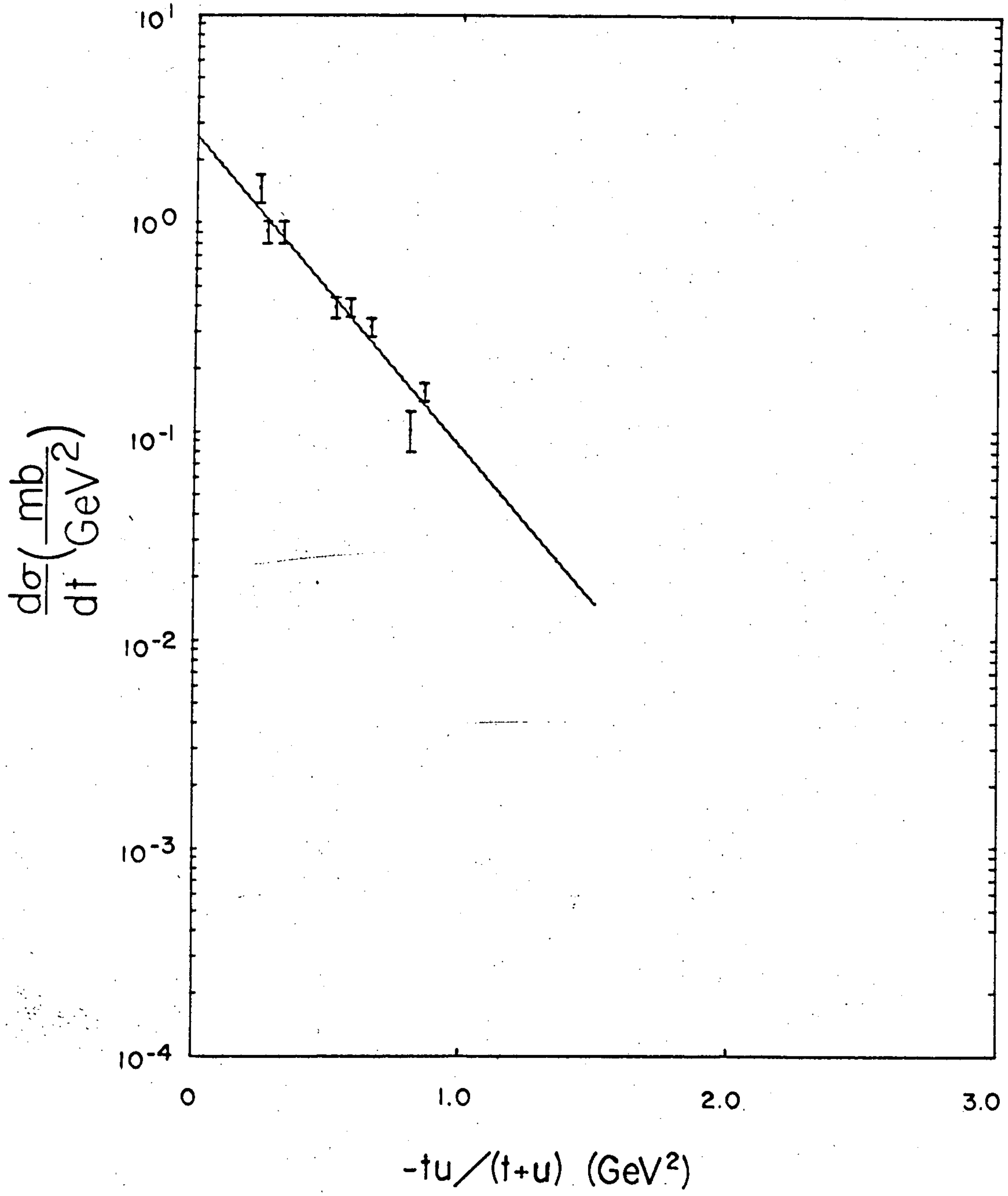

XBL 671-497

Fig. 29(a)

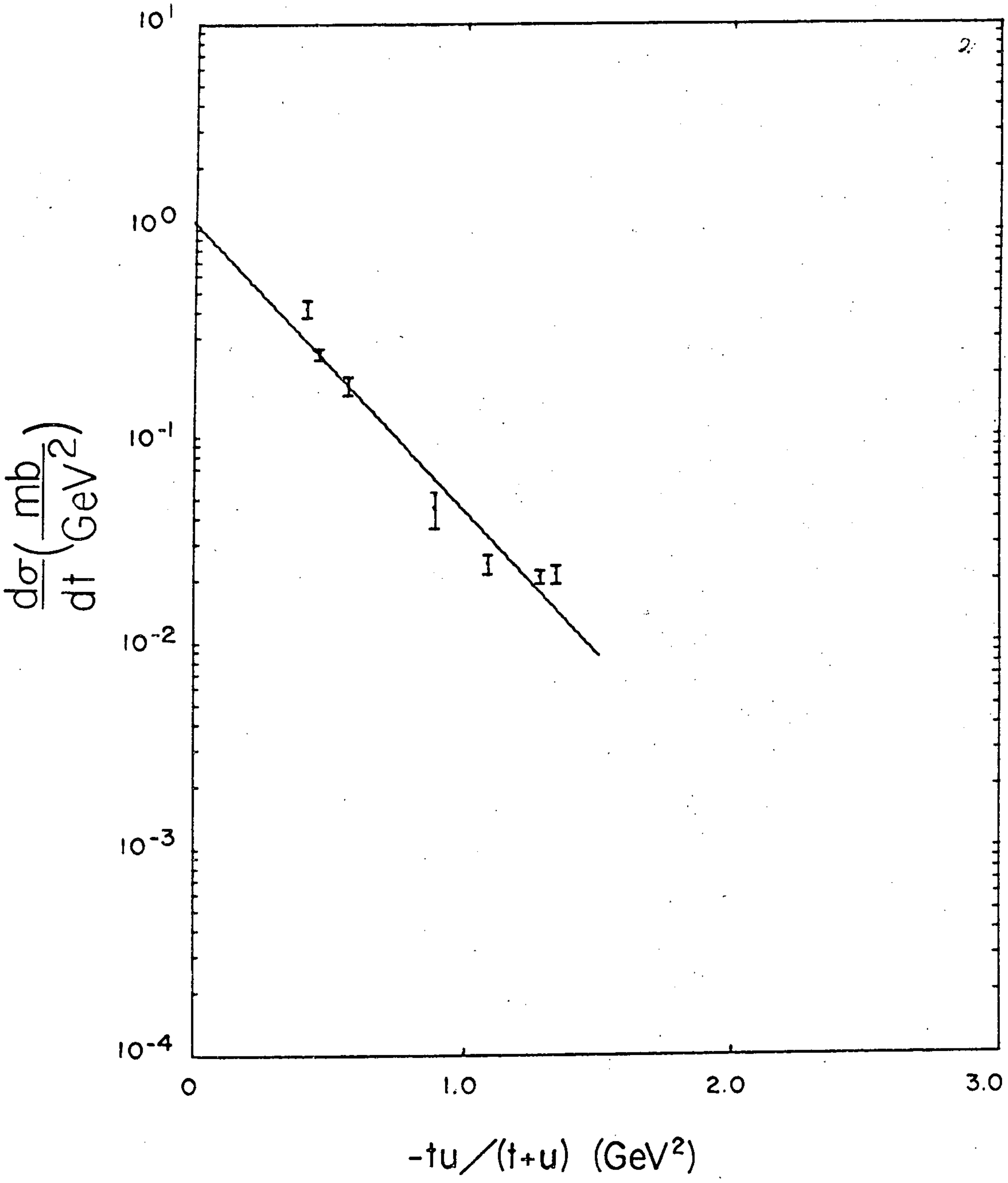

XBL 671-524

Fig. 29(b)

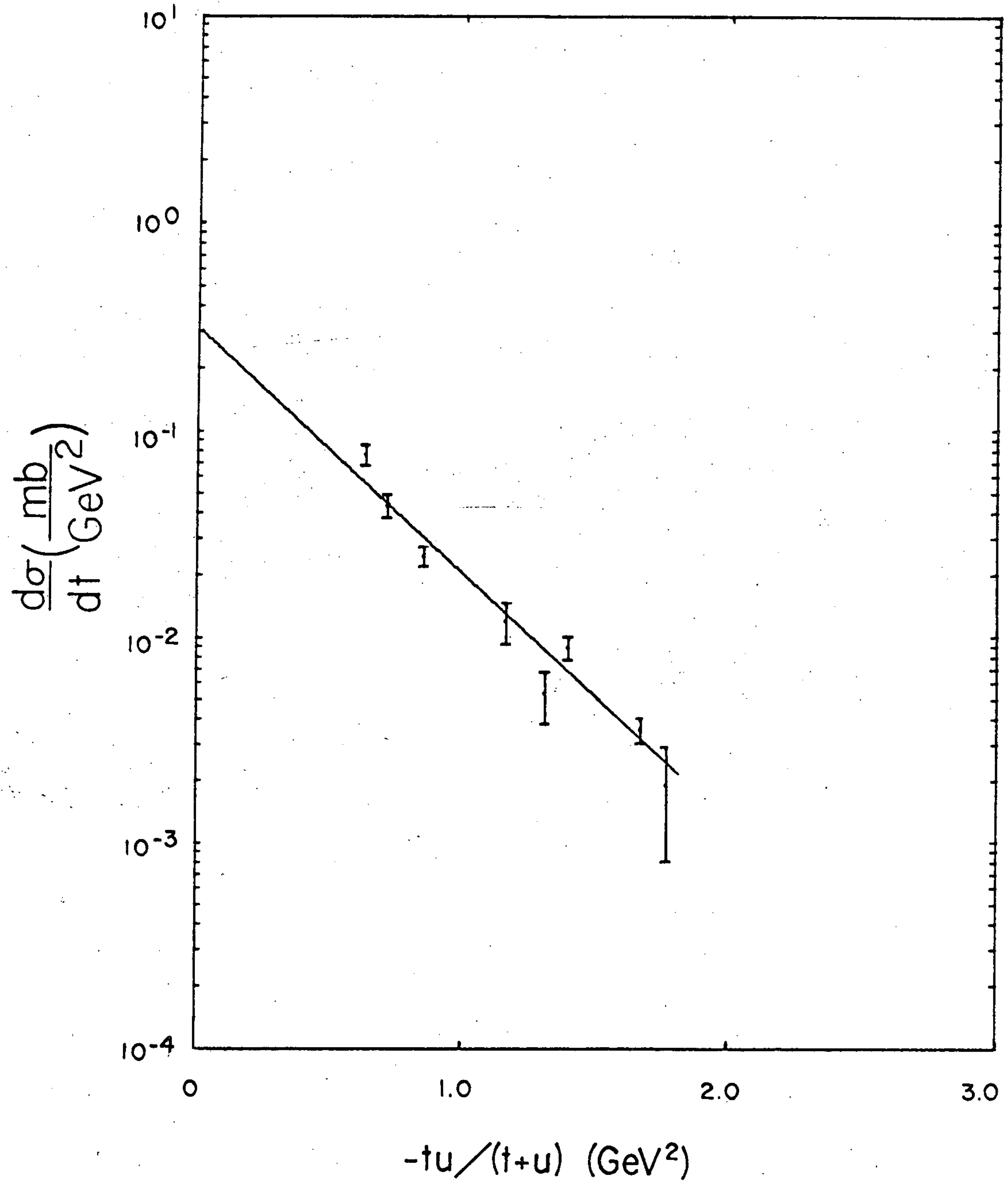

XBL 671-523

Fig. 29(c)

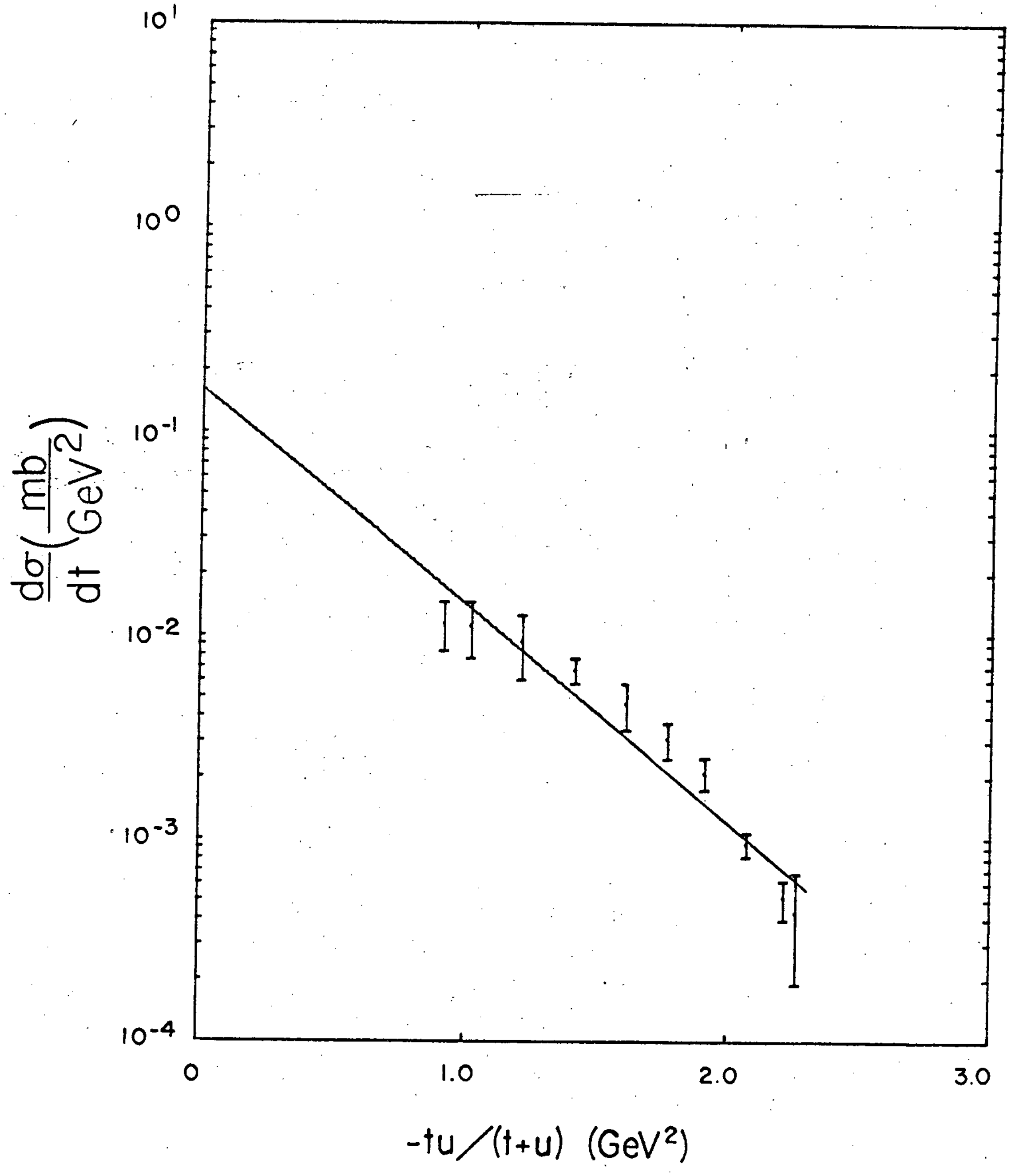

XBL 671-522

Fig. 29(d)

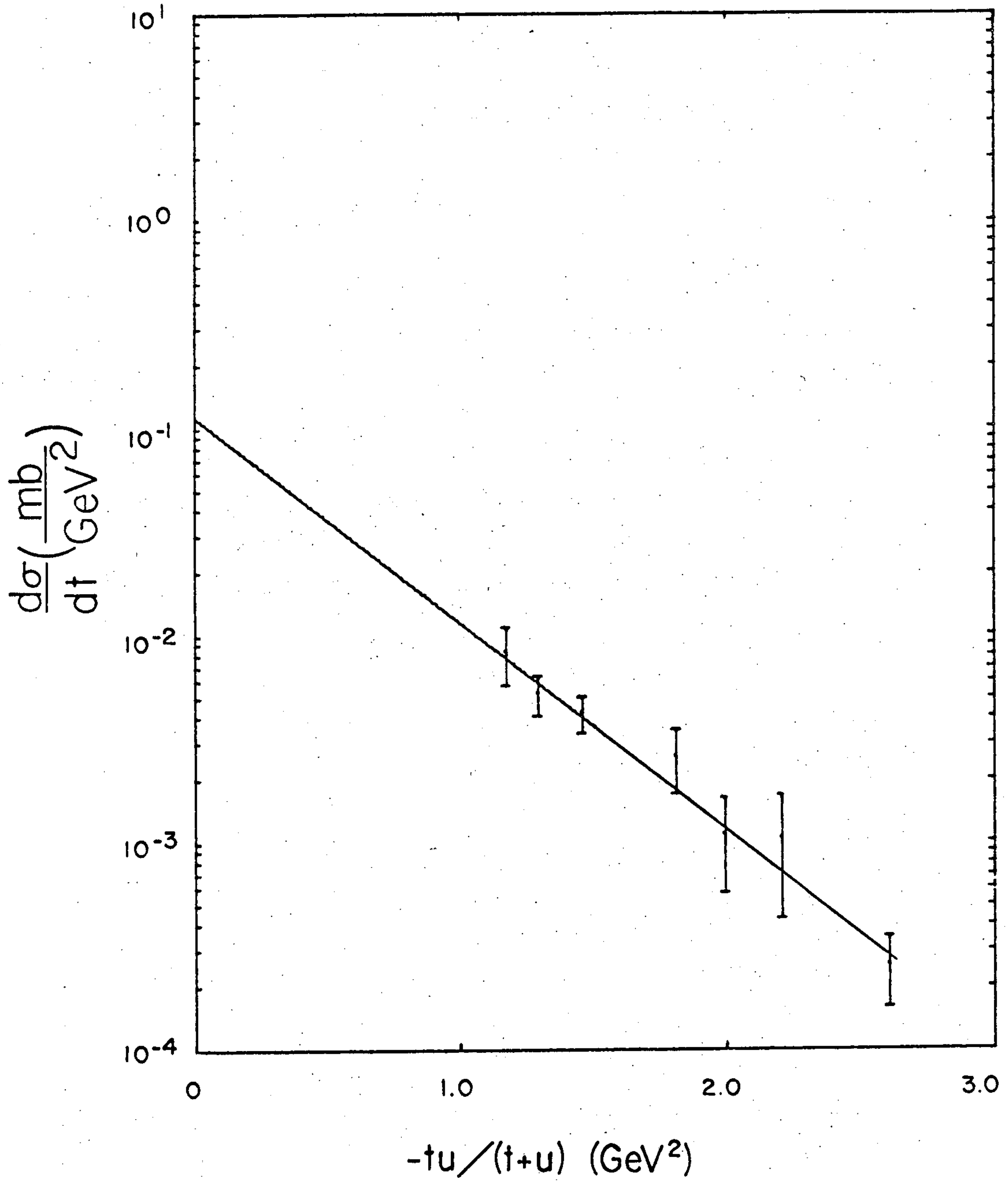

XBL 671-521

Fig. 29(e)

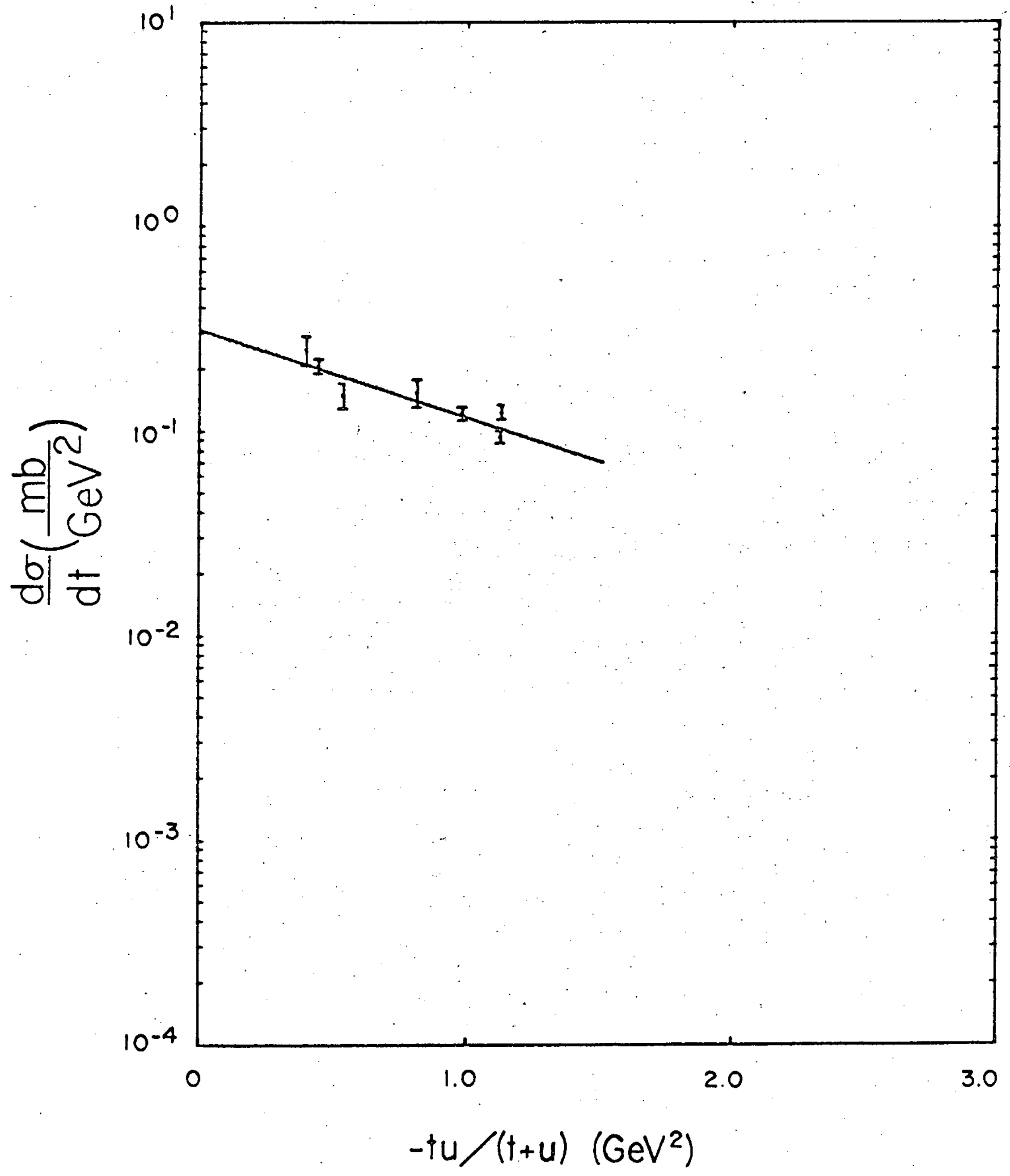

XBL 671-503

Fig. 30(a)

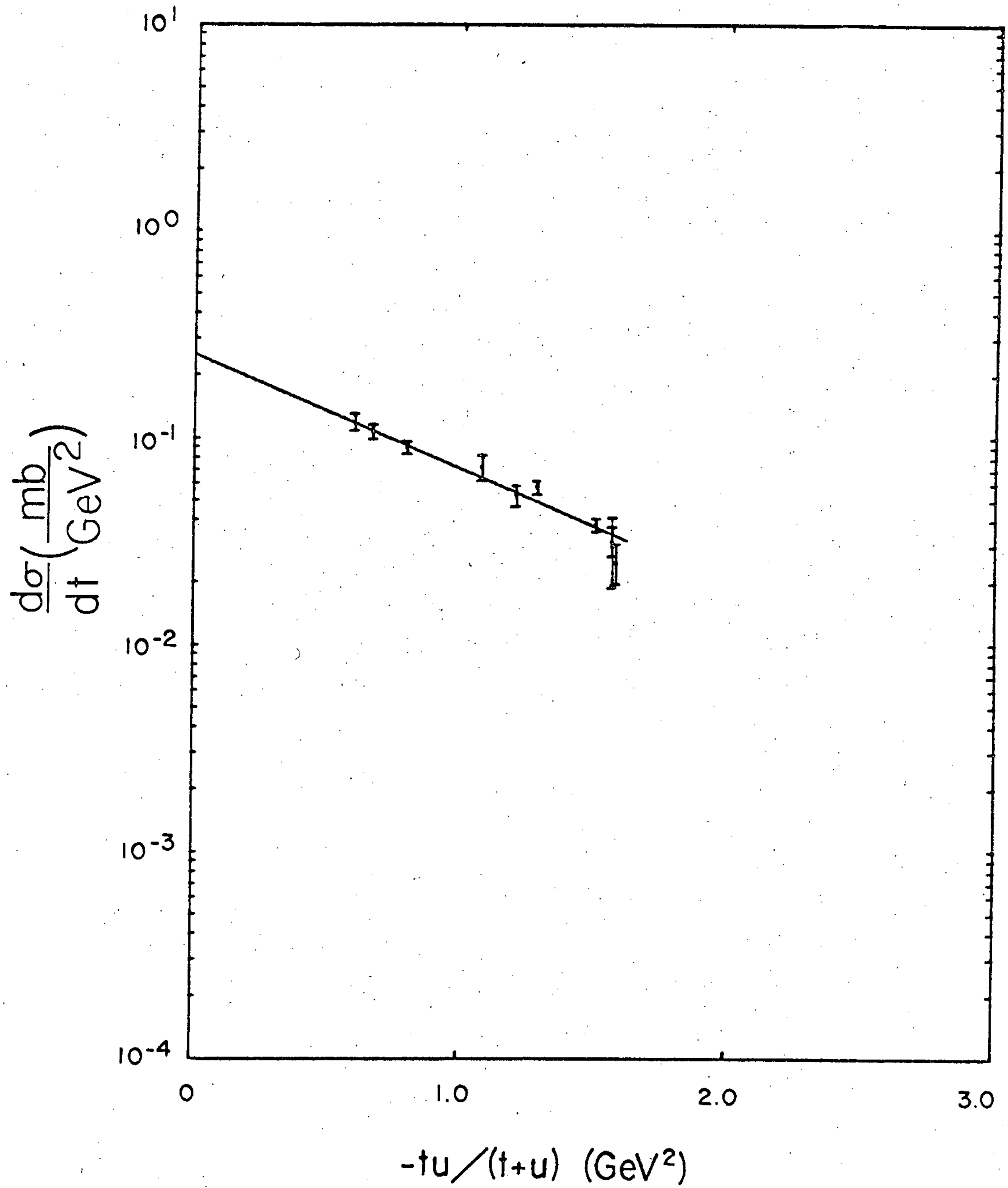

XBL 671-501

Fig. 30(b)

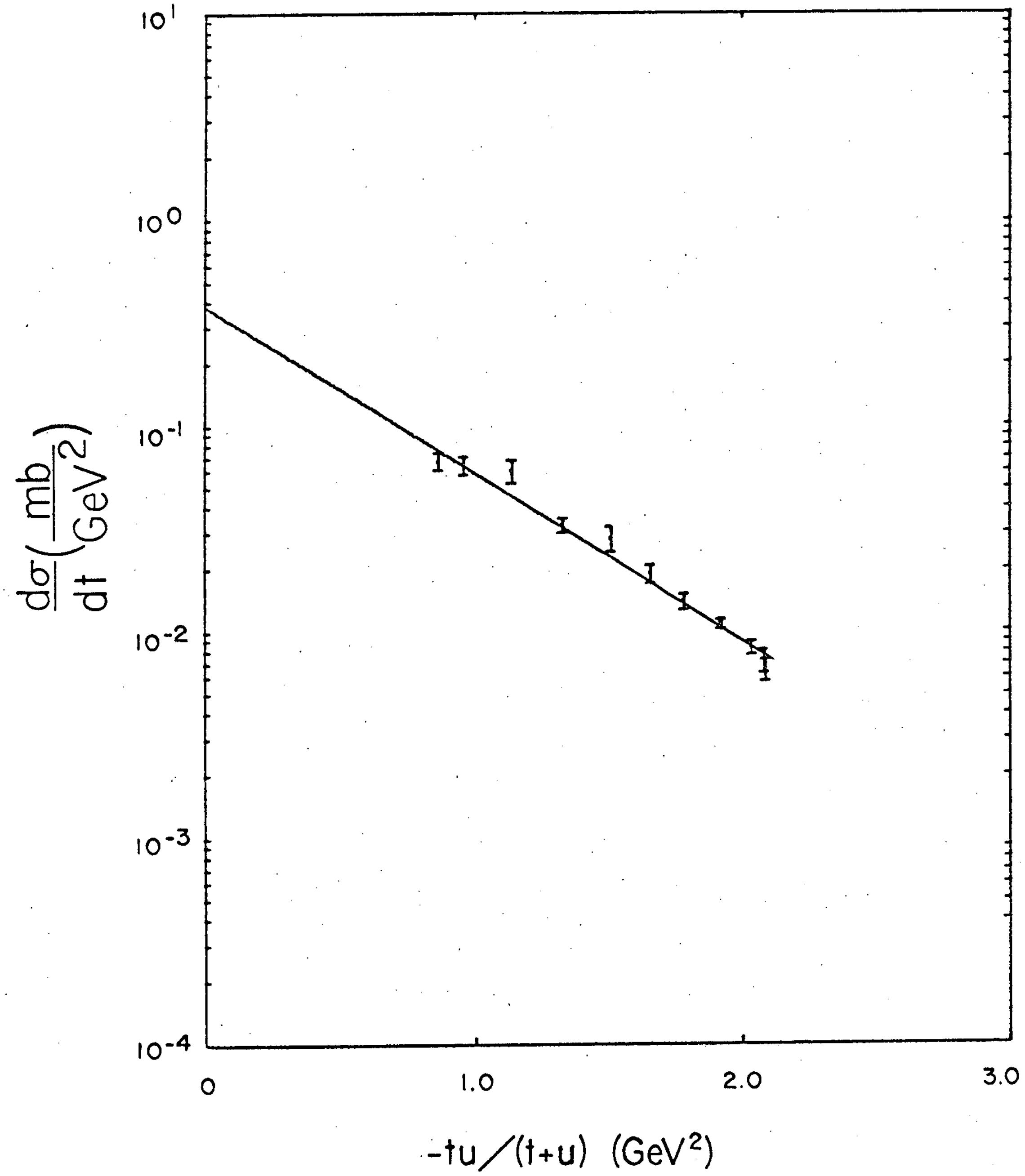

XBL 671-502

Fig. 30(c)

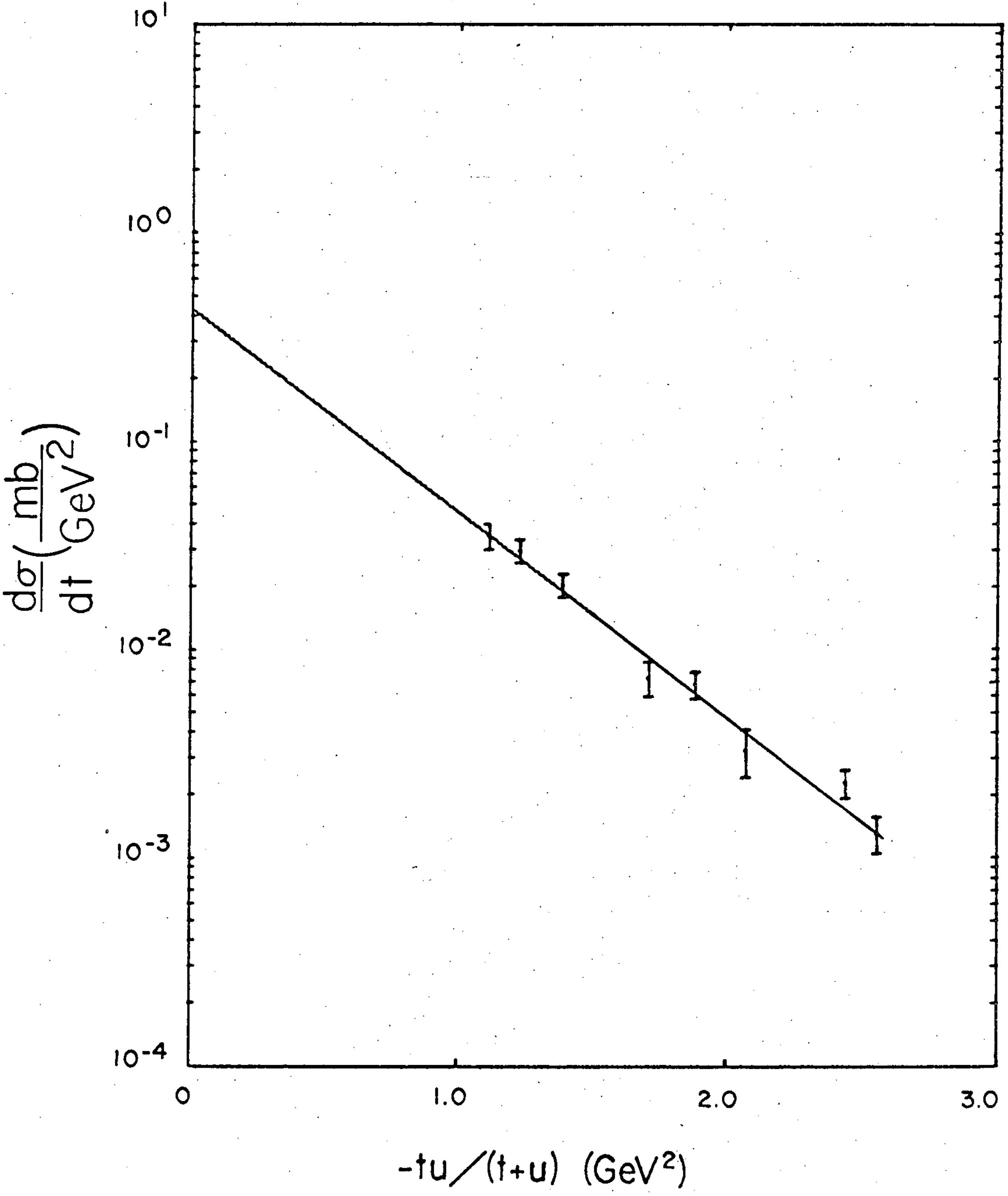

XBL 671-500

Fig. 30 (d)

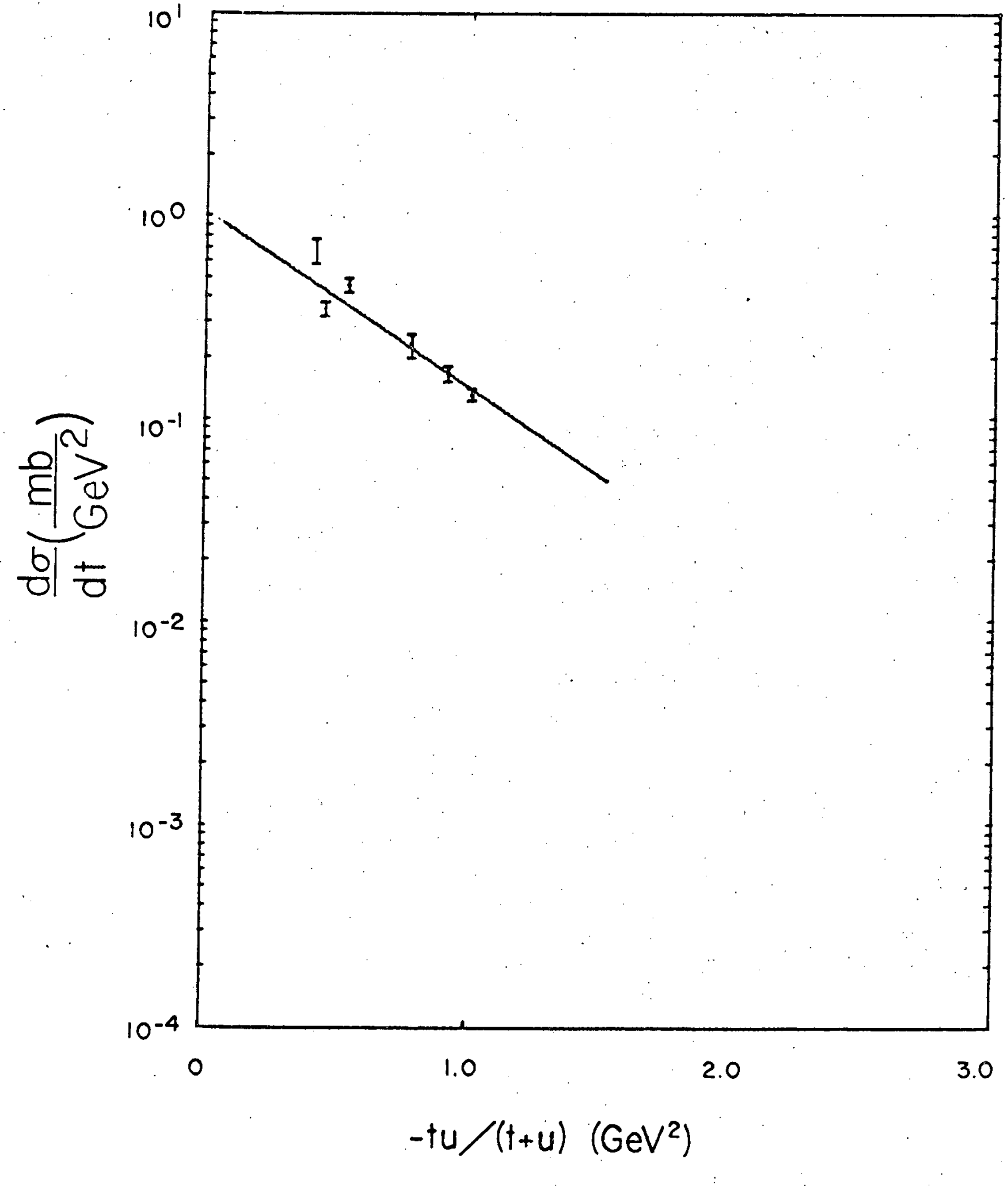

XBL 671-505

Fig. 31(a)

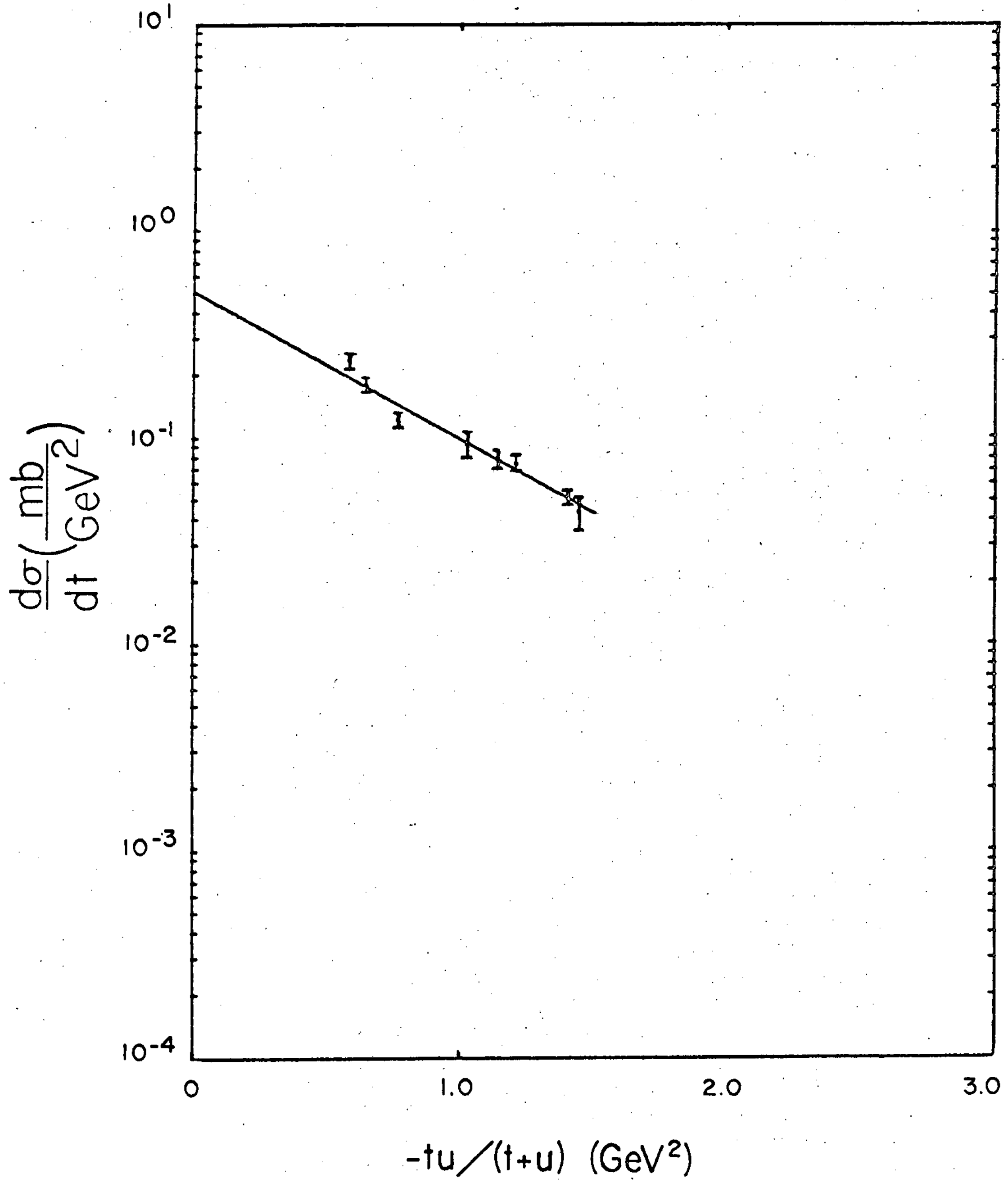

XBL 671-506

Fig. 31(b)

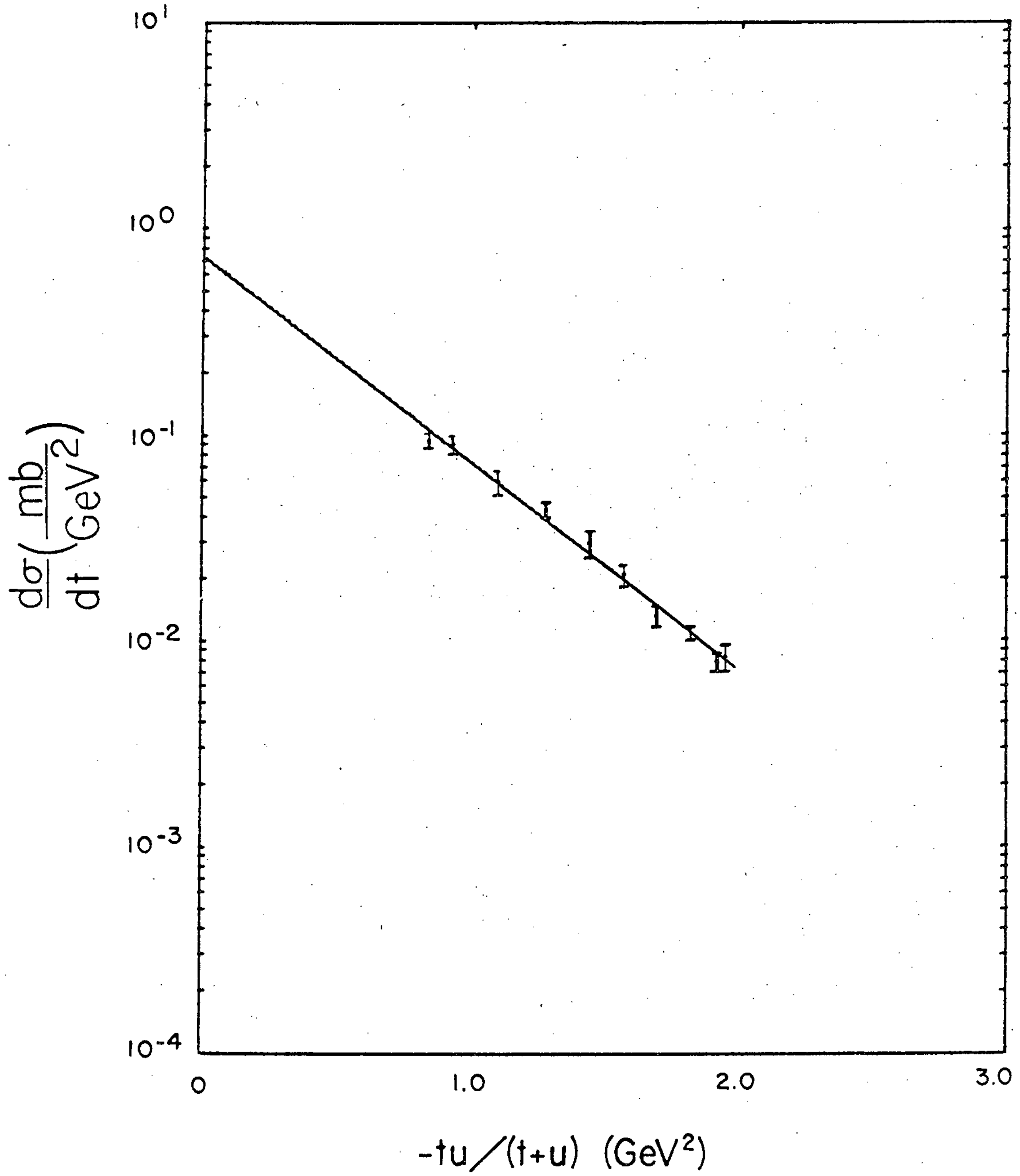

XBL 671-507

Fig. 31(c)

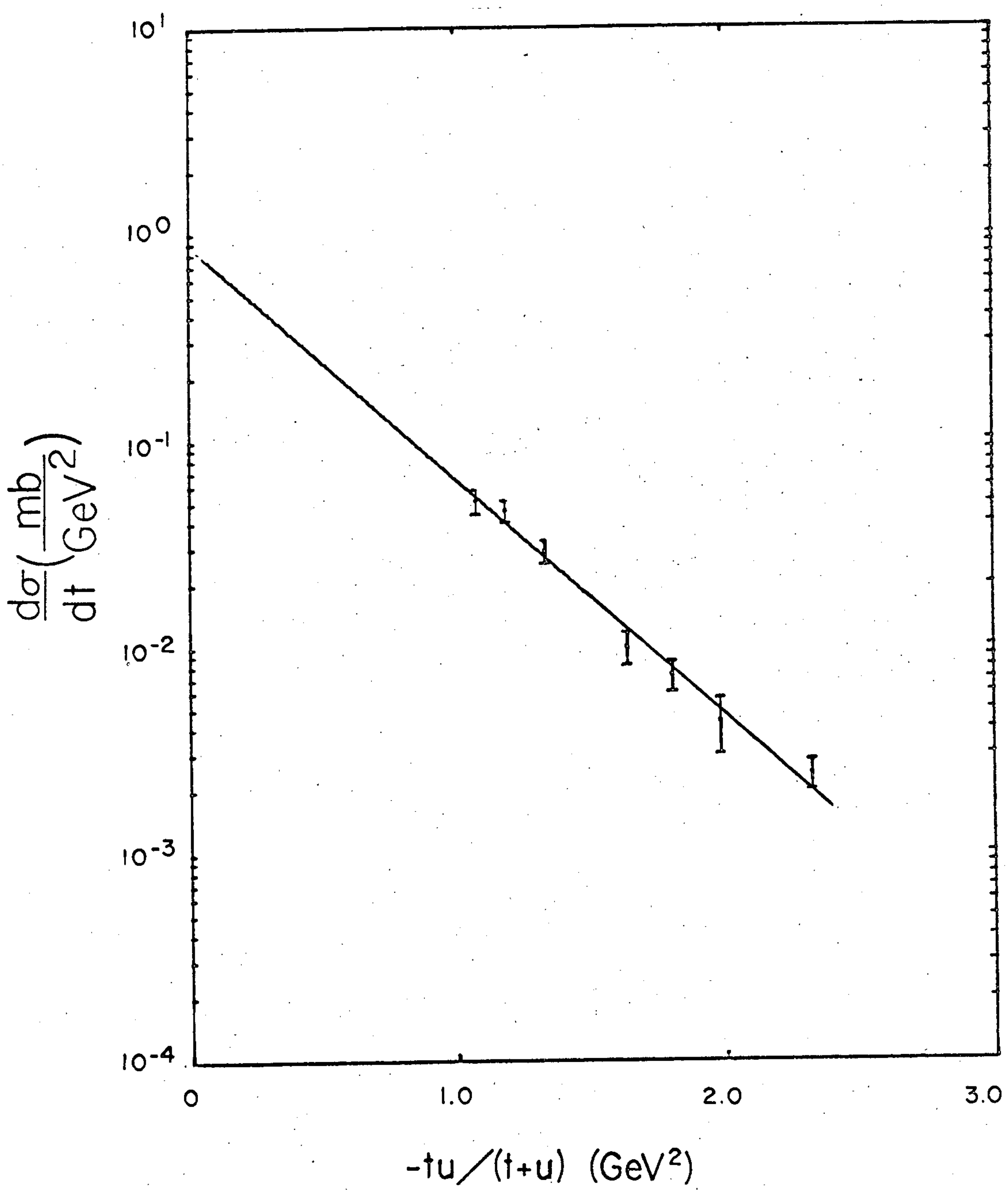

XBL 671-504

Fig. 31(d)

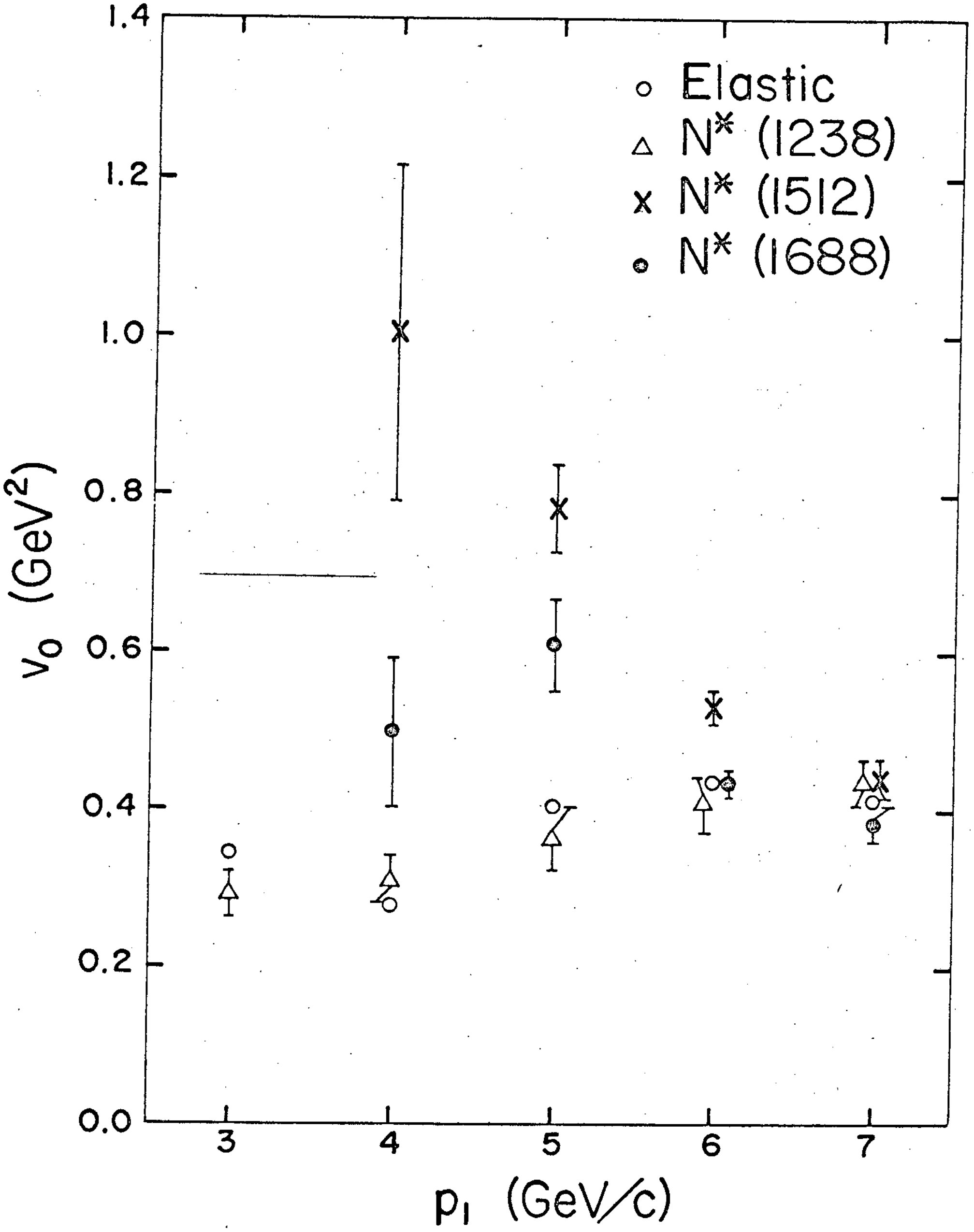

XBL 671-481

Fig. 32